

**EXPERIMENTAL AND NUMERICAL STUDIES ON THE NONLINEAR RESPONSES
OF WELDED WIDE FLANGE FUSES**

by

Winda Banjuradja

B.Sc., Bandung Institute of Technology, 2013

A THESIS SUBMITTED IN PARTIAL FULFILLMENT OF
THE REQUIREMENTS FOR THE DEGREE OF

MASTER OF APPLIED SCIENCE

in

THE FACULTY OF GRADUATE AND POSTDOCTORAL STUDIES

(Civil Engineering)

THE UNIVERSITY OF BRITISH COLUMBIA

(Vancouver)

January 2018

© Winda Banjuradja, 2018

Abstract

Metallic yielding damper is an example of commonly used as a sacrificial structural element to dissipate earthquake energy. In this thesis, a novel structural fuse, called Welded Wide Flange Fuse (WWFF), which utilizes commonly available welded wide flange sections to dissipate earthquake energy is proposed. WWFF is versatile, economic, and easy to fabricate. To dissipate earthquake energy, the WWFF is subjected to shear load in the longitudinal direction of the web. The inelastic behavior of the WWFF is expected to be concentrated in the web part of WWFF, where the earthquake energy is dissipated, while the flanges remain elastic. Experiment was conducted to study different parameters such as aspect ratios, slenderness ratios, and size ratios. These parametric studies provide detailed understanding in predicting the important engineering characteristics, such as yielding force, elastic stiffness, energy absorption, over-strength factor, and ductility of the WWFF. Nineteen specimens were tested under two type of loading protocols. Two analytical equations were derived to predict the yielding force and stiffness of the WWFF with different geometry parameters. Finite element models were developed using finite element software ABAQUS/CAE. The developed numerical models were verified using the experimental data. The verified numerical models were used to conduct detailed parametric studies on the WWFF with large array of aspect ratios and slenderness ratios. Beside the FE modelling approach, parametric studies on aspect ratio, slenderness ratio, and size ratio are conducted. Using this model, the effect of these parameters on key engineering characteristics is studied.

Lay Summary

The key purpose of this research is to investigate the nonlinear behavior of a newly proposed Welded Wide Flange Fuse as an economical and effective damper. This damper uses commonly available welded wide flange section. Therefore, it is very versatile and can be easily adjusted to fit various engineering demands.

Detailed numerical and experimental studies of the WWFF were conducted to identify the key design parameters of the WWFF. This research also proposed the general equation to be used by engineers in the industry. The results of the numerical and experimental studies shoes that the newly proposed WWFF has adequate capacity to dissipate stable energy and can be used as an effective structural damper for seismic application.

Preface

This thesis is submitted as a requirement of Master of Applied Science degree completion at University of British Columbia. This study of Welded Wide Flange Fuse was conducted under supervision of Prof. T. Y. Yang, from Department of Civil Engineering Department at UBC.

During this research, I received a lot of great help from industry, lab, and my peers. The experimental set up and specimens was kindly donated by George Third and Son, Custom Plate & Profiles, and Pacific Bolt. The testing apparatus was designed to be adjustable so that it can be reused in similar experiments. The experimental part of this research was conducted in collaborative with Dorian Tung, Yuan Jie Lie, and Jason Lin as the control team. The equations proposed in chapter 2 were originally derived by Lisa Tobber and T. Y. Yang.

Winda Banjuradja

2018

Table of Contents

Abstract	ii
Lay Summary	iii
Preface	iv
Table of Contents	v
List of Tables	ix
List of Figures	x
List of Abbreviations	xvi
Acknowledgments	xix
Dedication	xxi
Chapter 1: Introduction	1
1.1 Background	1
1.2 Objectives and research scope	4
1.3 Thesis outline	5
Chapter 2: Literature Review	7

2.1	Introduction.....	7
2.2	Types of dampers.....	7
2.3	Previous studies of metallic dampers.....	9
2.4	Limitation of previous studies	20
2.5	Welded Wide Flange Fuse (WWFF)	21
Chapter 3: Experimental Program		28
3.1	Introduction.....	28
3.2	Experiment Set Up.....	28
3.3	Loading mechanism.....	33
3.4	Specimen design	35
3.5	Test matrix	36
3.6	Instrumentations.....	40
3.7	Free run	44
3.8	Loading protocol.....	44
3.9	Testing procedure.....	46

Chapter 4: Experimental Result	48
4.1 Introduction.....	48
4.2 Free run result	48
4.3 Cyclic results.....	48
4.4 Monotonic result	64
4.5 Discussion	65
Chapter 5: Numerical Model	79
5.1 Introduction.....	79
5.2 Model description	79
5.3 Finite element model validation.....	87
Chapter 6: Parametric Study	90
6.1 Introduction.....	90
6.2 Finite element model matrix	90
6.3 Yielding force and initial stiffness.....	91
6.4 Over-strength ratio	93

6.5	Ultimate drift ratio	94
Chapter 7: Summary, Conclusion, and Recommendation		96
7.1	Summary and conclusion	96
7.2	Recommendation for future study	98
Bibliography		99
Appendices.....		104
A: Testing apparatus shop drawing.....		104
B: U2 displacement and rotation.....		113

List of Tables

Table 2.1 Comparison of dampers types.....	22
Table 3.1 Test matrix	37
Table 3.2 Testing matrix for size ratio study	38
Table 3.3 Testing matrix for aspect ratio study	39
Table 3.4 Testing matrix for slenderness ratio study	40
Table 3.5 Linear pot list	42
Table 3.6 Quasi-static drift loading	45
Table 4.1 Summary of experiment results	70
Table 4.2 Summary of yield force, initial stiffness, and prediction.....	74
Table 6.1 FEM analysis matrix	91
Table 6.2 Normalized yield force and normalized initial stiffness of equation, experiment, and finite element	93

List of Figures

Figure 1.1 Previous yielding steel plate devices (a) slit damper, (b) butterfly damper, (c) YSPD	3
Figure 1.2 Deformed shape of WWFF	3
Figure 2.1 Summary of dampers models and behavior (Source: Symans, M. D., A.M.ASCE, 2008)	9
Figure 2.2 Slit dampers test set up (Chan & Albermani 2008).....	10
Figure 2.3 (a) Slit dampers specimen; (b) hysteretic response (Chan & Albermani, 2007).....	11
Figure 2.4 Butterfly fuse geometric (Ma et al. 2011)	12
Figure 2.5 (a) Butterfly fuse specimen (b) hysteretic curve (Ma et al. 2011).....	12
Figure 2.6 Finite element modelling of butterfly fuse (Ma et al. 2011)	13
Figure 2.7 YSPD test set up (Chan & Albermani 2009).....	14
Figure 2.8 (a) YSPD specimen; (b) Load deformation response of cyclic loading (Chan & Albermani, 2009)	15
Figure 2.9 (a) Finite element modelling of YSPD; (b) Hysteretic response of YSPD from experiment and FE (Raquibul Hossain et al. 2011)	16

Figure 2.10 Comparison between test result and analytical equation (Raquibul Hossain et al. 2011)	17
Figure 2.11 PYSPD specimens (Chan & Albermani, 2007).....	18
Figure 2.12 Effect of perforation ratio to the yielding force.....	18
Figure 2.13 Buckling inhibited panel test (Brando et al. 2013).....	19
Figure 2.14 Deformed shape and stress diagram of the WWFF under combined shear and double curvature bending.....	23
Figure 2.15 σ_{YY} and τ_{XY} across the web	24
Figure 3.1 Experimental Setup	29
Figure 3.2 Loading beam	30
Figure 3.3 Pantograph system.....	31
Figure 3.4 Mounting	32
Figure 3.5 Out-of-plan support	32
Figure 3.6 Fin extension	33
Figure 3.7 Loading mechanism of the specimen	34
Figure 3.8 Pantograph force.....	35

Figure 3.9 Typical specimen geometry.....	37
Figure 3.10 WWFF specimens (a)A1.5S0.75 (b)A1.5S32 (c) A2S32.....	38
Figure 3.11 Actuator	41
Figure 3.12 Load cell	41
Figure 3.13 Linear pots layout	43
Figure 3.14 Geometric relationship of the linear pots configuration.....	43
Figure 3.15 Loading protocol for Quasi-static.....	46
Figure 4.1 Force-drift of A0.75S22	49
Figure 4.2 A0.75S22 at different drifts.....	50
Figure 4.3 Force-drift of A0.75S22-1.3	51
Figure 4.4 A0.75S22-1.3 at different drifts.....	51
Figure 4.5 Force-drift relationship of A0.75S22-2	52
Figure 4.6 A0.75S22-2 at different drifts.....	53
Figure 4.7 Force-drift relationship of A1.5S22	54
Figure 4.8 A1.5S22 at different drifts	54

Figure 4.9 Force-drift relationship of A2S22	55
Figure 4.10 A2S22 at different drifts	56
Figure 4.11 Force-drift relationship of A0.75S32	57
Figure 4.12 A0.75S32 at different drifts	57
Figure 4.13 Force-drift relationship A1.5S32	58
Figure 4.14 A1.5S32 at different drifts	59
Figure 4.15 Force-drift relationship of A2S32	60
Figure 4.16 A232 at different drift.....	60
Figure 4.17 Force-drift relationship of A0.75S43	61
Figure 4.18 A0.75S43 at different drifts	62
Figure 4.19 Force-drift relationship of A0.75S43	63
Figure 4.20 A1.5S43 at different drifts	63
Figure 4.21 Force-drift relationship of monotonic loading	64
Figure 4.22 Failure mode of the different specimen	66
Figure 4.23 Force-drift relationship of size ratio study (A0.75S22, A0.75S22-1.3, A0.75S22-2)67	

Figure 4.24 Cyclic force-drift relationship of aspect ratio and slenderness ratio study (all specimen except A0.75S22-1.3 and A0.75S22-2)	68
Figure 4.25 Sample backbone curve	69
Figure 4.26 (a) Hysteresis curve; (b) Backbone curve; (c) Factored cumulative energy of A075SR22, A075SR22-1.3, A075SR22-2.....	71
Figure 4.27 (a) Yield shear force and (b) initial stiffness for different aspect ratio	72
Figure 4.28 (a) Normalized yield shear force and (b) normalized stiffness for different aspect ratio	73
Figure 4.29 (a) Yielding drift ratio and (b) ultimate drift ratio.....	75
Figure 4.30 Backbone of normalized force plot of aspect ratio 0.75 and 1.5	76
Figure 4.31 Normalized energy plot of aspect ratio 0.75 and 1.5.....	77
Figure 4.32 Over-strength factor.....	78
Figure 5.1 Specimen model in ABAQUS/CAE.....	80
Figure 5.2 S4R shell element (ABAQUS manual)	82
Figure 5.3 Mode shape of buckling analysis of $A=0.75$, $A=1.5$, and $A=2$	84
Figure 5.4 A1.5S32 Backbone for different imperfection amplitude (0%, 0.25%, 0.3%, and 0.95% of D')	85

Figure 5.5 A1.5S32 backbone for different mesh size (1%, 2%, 10%,20%, and 40% of <i>tw</i>)	86
Figure 5.6 Comparison between experimental and FE model for cyclic loading.....	88
Figure 5.7 Buckling shape of experiment and corresponding U3 deformation of FEM	89
Figure 6.1 Normalized yield shear force and stiffness for different aspect ratio.....	92
Figure 6.2 Over-strength ratio for different slenderness ratio	94
Figure 6.3 Ultimate drift ratio of parametric study.....	95

List of Abbreviations

Δ_{total}	Total displacement
C_y	Normalized yield force
D'	Clear web depth
DOF	Degree of freedom
D_w	Web depth
E_N	Normalized energy
V_P	Pure shear yield force
V_u	Ultimate shear force
$V_{y,eq}$	Predicted yield shear force
k_s	Plate buckling coefficient
t_w	Web thickness
σ_T	True stress
$\sigma_{yy,avg}$	average axial stress

τ_y	Shear stress at yielding
ϵ_T	True strain
E	Young's modulus
FE	Finite element
σ_y	Yield stress
LP	Linear pot
N	Axial force
P	Actuator force
PYSPD	Perforated yield shear panel device
WWFF	Welded Wide Flange Fuse
YSPD	Yield shear panel device
A	Aspect ratio
G	Shear modulus
I	Moment of inertia
K	Elastic stiffness

M	Moment
S	Slenderness ratio
V	Shear force
a	Web length
f	Flexibility
y	Layer distance
γ	Drift
σ	Stress
τ	Shear stress
ϵ	Strain
γ_y	Yield drift ratio
γ_u	Ultimate drift ratio

Acknowledgments

Firstly, I want to thank my supervisor, Prof. T. Y. Yang of the Civil Engineering Department at the University of British Columbia. His guidance and support has led me to conduct great research and become a better intellectual.

I want to acknowledge the financial support from the Indonesia Presidential Scholarship, awarded by the Indonesian Endowment Fund for Education. Without this support, I would not have been able to pursue my degree at the University of British Columbia.

I also want to express my gratitude to George Third and Son, Pacific Bolt, and Apex Custom Plates & Profile for fabricating and donating the testing apparatus and specimens for my research.

To all my colleagues and my fellow researchers, especially Lisa Tobber and Fabrício Bagatini Cachuço, you have given me tremendous support throughout my endeavors. I would like to offer thanks to my engineering classmates, Marcel Hong, Eytan Fiszman, Marco Galaviz, Steve Jeon, and Alex Mueller, for our times together throughout the program. To my very dedicated interns, Laurence Yin, Soham Vaze, and Allen, thank you for your great help in the lab. For the help from our structure lab technicians, Dave Roberts and Harald Schrempp, I will be forever indebted.

I also want to thank my family, my mom and dad, and my brother. They will always be my anchor and number one support. This thesis is dedicated to my mother, who inspires and shapes me to be the best version of myself.

I would like to express my great appreciation to Danika Wheeler and Mary Burns who kindly gave their time and effort to proofread my paper and thesis. I also would like to extend my gratitude to my friends back in Indonesia, Ruri Fitriyanti, Janette Suherli, Angel Goenawan, Florentia Edrea, who always believed in me and supported me.

Finally, I want to thank my friends here in Vancouver, Sophie Lewis, Carmen Chung, Sandy Chan, Melissa So, Danika Wheeler, Mary Burns, Reanne Bowlby, Farhana A. K., and Jutta Kolhi, for reminding me to have fun despite the pressure as a graduate student.

Dedication

I dedicated this research to my mother, Lusianawaty Tana,

and to Indonesian and other people in the world that are affected by earthquake.

Chapter 1: Introduction

1.1 Background

Many highly populated cities around the world are located in earthquake prone zones. The buildings in these areas need to have good seismic performance during earthquakes to protect their inhabitants. However, based on the current seismic design principal, most of the damaged structures are far too expensive to be repaired and need to be demolished after strong earthquake shaking. This results to significant financial losses. Therefore, resilient earthquake resistant buildings are essential in regions of high seismicity.

One of the solutions to improve the seismic performance of buildings is to use energy dissipating devices or dampers to dissipate the sudden surge of earthquake energy. The concept is similar to the action of an electrical fuse such that when there is an energy spike in an electrical circuit, the fuse will blow to protect the electronic devices. During an earthquake, the damper is designed to absorb or redirect earthquake energy – to be ‘damaged’ or ‘sacrificed’ – in order to protect the building’s other structural components such as gravity systems. Later on, this device will be rapidly replaced so that the building can return to its full function efficiently.

It is important that reliable dampers for buildings be widely available in earthquake prone zones. The characteristics and behaviors of dampers need to be well understood to engineers to design the fuse suitable for any given location. Dampers also need to be versatile to meet diverse structural demands. Finally, they should be easily fabricated as well as economical.

The development of energy dissipation devices and their implementation gained a lot of attention in the mid-1990s. These energy dissipation devices can be divided into three categories: passive, active, and semi-active systems. Active and semi-active systems require a power source to operate. Passive devices are designed to operate without a power source – in the event of an earthquake, either the dynamic response of the system can be reduced (e.g. base isolation or tuned-mass damper) or energy is dissipated through inelastic behavior (e.g. friction, viscoelastic, yielding of metals).

The concept of sacrificing a particular structural component to dissipate energy had been studied by researchers and used by engineers around the world. Various types of these innovative devices were developed over the past decades. A metallic damper is one type of the structural fuse that had been developed. It dissipates earthquake energy through yielding or inelastic behavior.

In 2011, Ma et al. [10] have conducted experimental tests on steel plates cut with slit or butterfly patterns to form dampers (Figure 1.1a and Figure 1.1b). Each steel strip is designed to yield in flexure and form plastic hinges at the ends when the damper is sheared horizontally which provides stable energy dissipation capacity. However, as the steel plate is cut into small strips, the elastic stiffness for the slit and butterfly dampers is relatively low which might not be desirable for some structural applications. In 2009, Chan and Albermani [5] developed the Yielding Shear Panel Device (YSPD), where a steel plate was cut and welded inside the hollow steel sections (HSS) (Figure 1.1c). In the YSPD the HSS is used as the boundary element for the welded plate and location for the bolted connection to the structure. YSPD is designed to

dissipate the earthquake energy through shear yielding of the welded plate and flexural deform of the HSS at the same time. YSPD has stable energy dissipation, however, design of the YSPD is difficult as the coupling between the HSS and yielding plate is highly nonlinear under deformation. More importantly, YSPD fabrication is very difficult because it requires the web plate to be cut into the exact dimension of the HSS opening and welded inside the HSS.

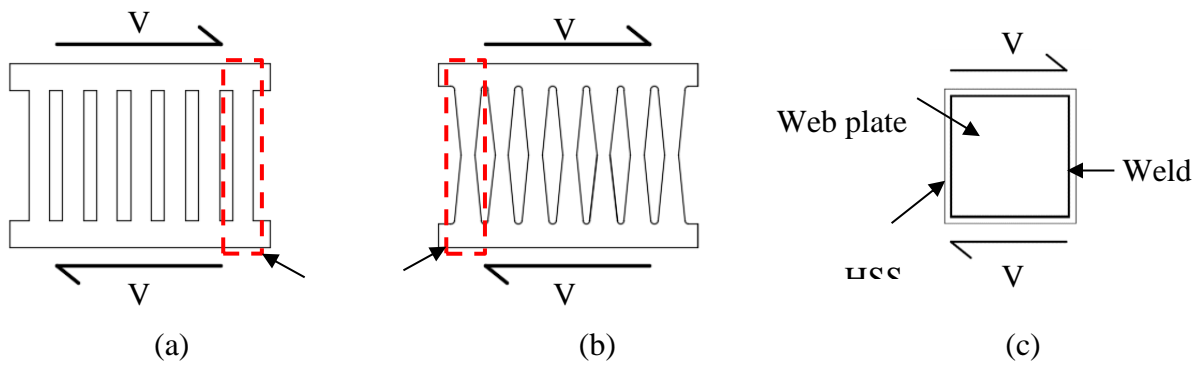


Figure 1.1 Previous yielding steel plate devices (a) slit damper, (b) butterfly damper, (c) YSPD

In this study, a novel steel plate damper called a Welded Wide Flange Fuse (WWFF) is proposed. Figure 1.2 shows the concept of the WWFF.

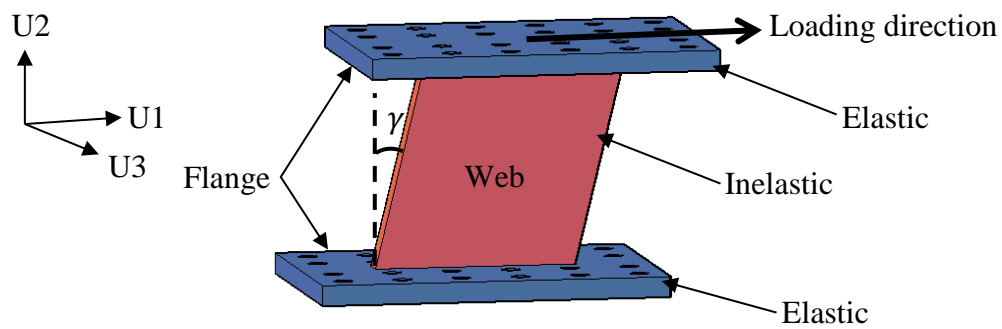


Figure 1.2 Deformed shape of WWFF

WWFF uses welded wide flange sections to dissipate earthquake energy through shear yielding of the web in the longitudinal direction, while the flanges are designed to remain elastic. The use of the welded wide flange sections provides many significant advantages. First, the size of the flanges and web can be varied to meet different structural application, making the design and fabrication of WWFF versatile, efficient and economical. Second, the yielding mechanism expected is a combination of flexure and shear of the web. Therefore, it will have higher stiffness. The thick flanges reduce the deformation of the flanges due to prying action. Third, the WWFF is designed to be bolted to the structure through the flanges, which can be capacity designed to remain elastic. The elasticity of flanges makes the energy dissipation mechanism very stable and allows the WWFF to be easily replaceable after a strong earthquake. Hence, equipping a structure with WWFF is more resilient towards future earthquake.

1.2 Objectives and research scope

The objective of this research is to study the behavior of a new metallic yielding damper using commonly available welded wide flange section. This welded wide flange is subjected to shear loading in a longitudinal direction, with attention paid to yielding and ultimate force, yielding displacement, and ductility. These values are important for engineers in the design of fuses and to capacity design the other structural components.

To accomplish this objective, this study has two phases: the experimental phase and the numerical phase. The results from the experiment was used to validate the finite element and analytical equation of the numerical phase. Many aspects of WWFF behavior, such as the size effect, slenderness ratio, failure modes, and aspect ratio, were investigated.

The experimental phase of the research was conducted at University of British Columbia. Nineteen specimens were tested with two different loading protocols (monotonic and cyclic). The yielding force, stiffness, ductility, failure mechanism, and the energy absorption of the fuse were experimentally studied. The testing apparatus was fabricated and donated by George Third and Sons, Custom Plate & Profiles, and Pacific Bolts.

In this study, simple equations to predict the yielding and the stiffness of the WWFF are proposed. These analytical equations are used to design the specimen and to predict some of the parameter's effect on the fuse's behavior. These equations serve as tools for engineers to design the fuse in a building. The finite element model was developed in ABAQUS/CAE and validated by the experimental result. The finite element model was later used to conduct the parametric study.

1.3 Thesis outline

Chapter 2 of this thesis presents a literature review of the various types of metallic dampers currently available. A summary of both experimental and numerical results of these studies is presented, followed by a comparison between the previous studies with WWFF. The derivation of the proposed equation for yielding and stiffness closes the chapter.

The experimental program design and set-up are discussed in Chapter 3. The loading mechanism of the test set up is then explained, followed by a discussion about the instrumentation layout. Two loading protocols (monotonic and cyclic) were used in this research. The cyclic loading protocol applied to provide the hysteresis behavior of WWFF, whereas the monotonic result was

compared to the hysteresis' backbone. A detailed explanation about how the testing matrix was developed is also provided.

The results of the experiment are discussed in Chapter 4. The observation of each specimen for different loading protocol is presented. This includes the force deformation relationship, energy absorption, failure mechanism, documentation, and observations of the overall behavior of the specimen as well as the testing apparatus.

Chapter 5 focuses on the finite element modelling done using ABAQUS/CAE. Numerical modelling techniques such as mesh convergence study, material calibration, and boundary condition are covered. Several finite element models are validated with the test results.

The numerical parametric study of WWFF is discussed in Chapter 6. The results from these models are compared with the proposed equations (developed in Chapter 2) to predict the yielding and stiffness of WWFF. In addition, this chapter discussed the effects of slenderness ratio and aspect ratio on over-strength factor and ultimate drift ratio of WWFF.

Finally, the summary and conclusions from previous chapters, as well as the future research recommendation are presented in Chapter 7.

Chapter 2: Literature Review

2.1 Introduction

The concept of fuse application is common in earthquake engineering practice. A good fuse must have these following characteristics: (1) shows stable hysteretic behavior; (2) have good long term reliability; (3) provide adequate stiffness and strength to resist service load; (4) have good resistance to environmental factors. Different types of fuses are categorized based on their energy dissipation mechanism, rate dependency, or their material. The most common dampers type based on the energy dissipation mechanism are discussed below.

2.2 Types of dampers

2.2.1 Viscous fluid dampers

Viscous fluid dampers usually consist of a hollow cylinder with fluid (typically silicone based) inside. The mechanism of this device is similar to a piston in vehicle. The piston head pushes and forces the fluid to flow through orifices on or around the piston head. This motion creates a pressure differential across the piston head and therefore generates large forces that resists the relative motion of the dampers. Viscous fluid dampers will be activated at low displacement and will require a small restoring force.

Although the performance of viscous fluid dampers has been proven through military application, these devices have a potential for fluid leakage that raises reliability concerns.

2.2.2 Viscoelastic solid dampers

Viscoelastic solid dampers are viscoelastic material pads attached to steel plates. These devices dissipate energy as heat from the shearing of the viscoelastic material. They also show both elastic and viscous behavior, meaning that they are displacement and velocity dependent. These devices also work at low displacement. Another desirable behavior is the restoring force they provide. The disadvantage is the reliability concern from the possibility of de-bonding or tearing of the attached viscoelastic pads.

2.2.3 Friction dampers

Friction dampers are another type of damper that dissipates energy through friction. The force generated from the damper is explained using the Coulomb model of friction, where force equals the coefficient of the dynamic friction times the normal force at the sliding surface.

These devices dissipate a large amount of energy per cycle due to their rectangular hysteretic curve (See Figure 2.1). Nevertheless, the sliding interface needs regular maintenance. Also, friction dampers produce large permanent displacement if there is no restoring force.

2.2.4 Metallic dampers

Metallic dampers dissipate energy when undergoing inelastic deformation. The use of steel and aluminum enable this effect, as well as providing both consistency due to its homogeneous nature and long-term reliability. These technologies, which include ADAS, BRB, and SPSW, are well developed and have been implemented widely.

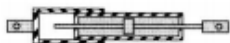

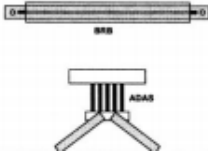
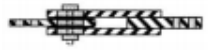
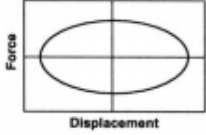
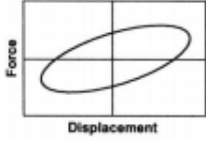
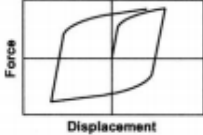
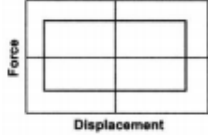
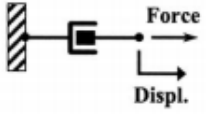
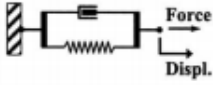
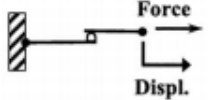
	Viscous fluid dampers	Viscoelastic solid dampers	Metallic dampers	Friction dampers
General construction				
Hysteretic behavior				
Idealized physical model			No idealized model	

Figure 2.1 Summary of dampers models and behavior (Source: Symans, M. D., A.M.ASCE, 2008)

2.3 Previous studies of metallic dampers

One of the most common earthquake energy dissipation mechanisms is inelastic deformation. Metal is a homogenous material that is reliable and shows good inelastic behavior. This thesis focuses on the development of a new metallic damper called a Welded Wide Flange Fuse (WWFF). The yielding mechanism of WWFF is longitudinal shearing of its web. This section discusses previous research on similar devices as to what is proposed in this thesis.

2.3.1 Slit dampers

In 2008, Chan & Albermani developed an experimental study of slit dampers for an energy dissipation device. Slit dampers are fabricated from I-beam section with numbers of laser cut slits on its web. The remaining strips act as beams with fixed ends. The dampers dissipate energy by flexural yielding of these beam strips.

A total of nine specimens were tested at the City University of Hong Kong. The test set-up is presented in Figure 2.2. This test set up generated shear load to the specimen while maintaining the verticality of the loading beam. One of the specimen (SL4) hysteretic curves was presented on Figure 2.3. The experiment results showed that slit dampers had stable hysteretic behavior and was able to dissipate large amount of energy.

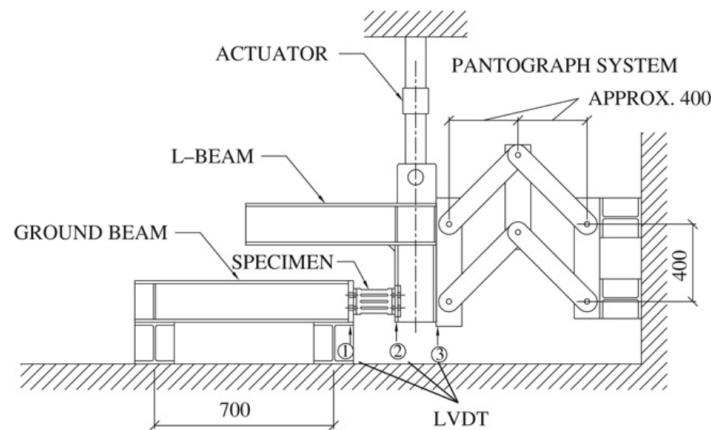
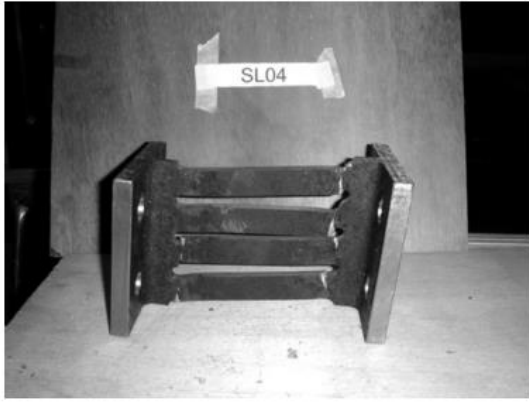
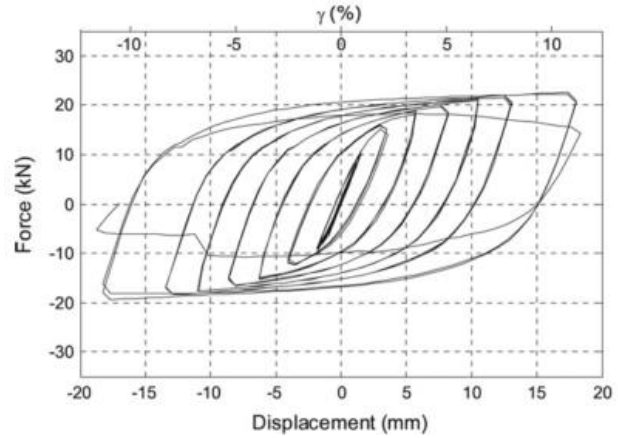


Figure 2.2 Slit dampers test set up (Chan & Albermani 2008)



(a)



(b)

Figure 2.3 (a) Slit dampers specimen; (b) hysteretic response (Chan & Albermani, 2007)

In this study, equations to predict the yielding force and the stiffness were developed. As mentioned before, the yielding mechanism of this device is flexural controlled, therefore, the yield strength of the device could be predicted with a pure flexural plastic mechanism calculation. These equations predicted the yield force accurately but are valid for flexural controlled yielding mechanism only. However, in case of plate that yields in combination of shear and flexural, these proposed equations might not be able to give a reasonable result.

2.3.2 Butterfly fuse

Ma et al. studied about butterfly fuse in 2011. Butterfly fuse is a plate damper with “diamond” shaped openings as shown in Figure 2.4. This geometrical shape is expected to have greater distributed yielding throughout the links due to the shape similarity with the fixed-ends beam.

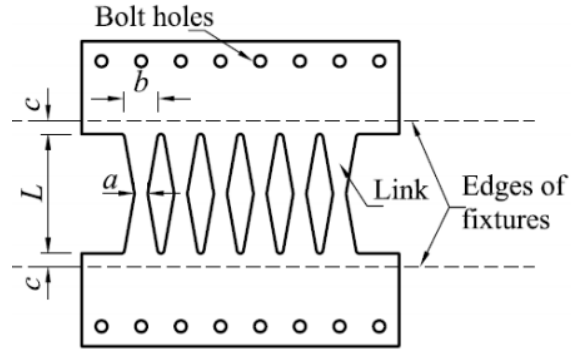
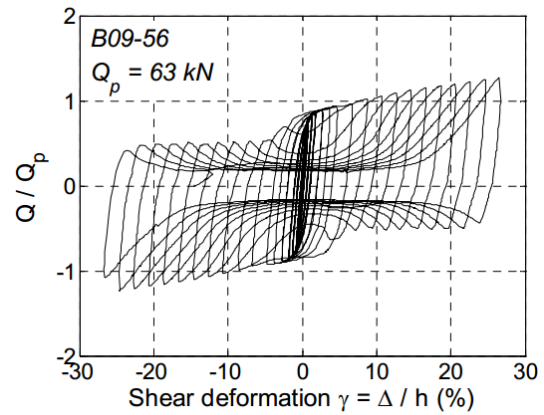


Figure 2.4 Butterfly fuse geometric (Ma et al. 2011)

Butterfly fuse performance was researched by Ma et al (2011) in Report No.173. In this research, different geometry variations were tested (Figure 2.5a). The ratio of link width to thickness (b/t) tested in this report was 2-10 whereas the slenderness ratio (L/t) was 14-56. From the experiment, it was observed that the fuses failed at a shear deformation of 35% (Figure 2.5b).



(a)



(b)

Figure 2.5 (a) Butterfly fuse specimen (b) hysteretic curve (Ma et al. 2011)

A numerical model was developed using ABAQUS finite element software. A three-dimensional, four-node-shell element was used to model the specimen. An elastic, perfectly plastic material model was assumed in this model. In this numerical model, the testing apparatus was also included in the model using a rigid element. It was found that the model showed sufficient accuracy to represent the fuse behavior.

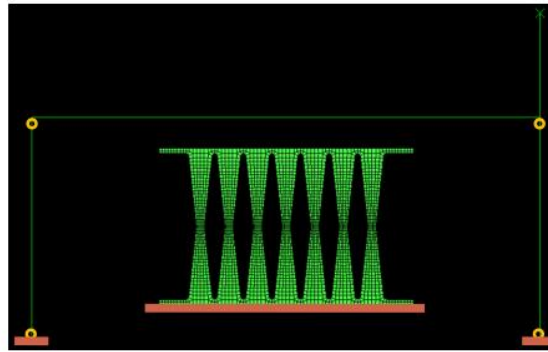


Figure 2.6 Finite element modelling of butterfly fuse (Ma et al. 2011)

2.3.3 Yielding Shear Panel Device (YSPD)

In 2009, Chat et al. studied Yielding Shear Panel Device as a structural fuse. The development of YSPD was started from the interest of utilizing the plastic shearing mechanism of thin plate as a damper (Nakashima et al, 1994). The application of low yield steel was studied to avoid shear buckling happens before yielding occurs. Later on, Chan et al. in 2009 studied the shear yielding behavior of a steel plate welded inside hollow section using regular steel material. The steel plate acts as a diaphragm and yields in shear. Whereas, the hollow section provides supports as it welded to the plate edges. The objective of the study was to investigate the performance of YSPD as a component (without the frame structure) to dissipate energy.

The experiment was conducted at the structural laboratory of the City University of Hong Kong (shown in Figure 2.7). The testing apparatus used for the test was the same with the test set up for the slit dampers test (Chan & Albermani 2009).

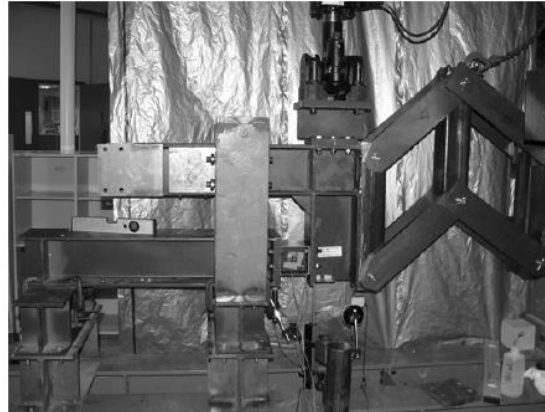
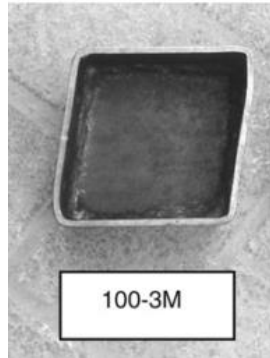


Figure 2.7 YSPD test set up (Chan & Albermani 2009)

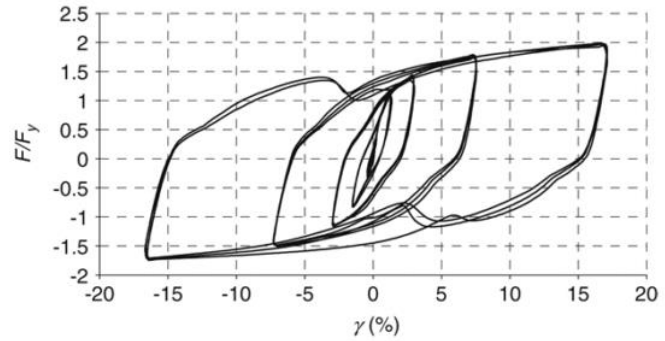
In this study, 19 specimens with two different square hollow section (SHS) sizes (100X100X4 and 120X120X5) and three different diaphragm plate thicknesses (2, 3, and 4 mm). Figure 2.8a shows the deformed YSPD specimen and its hysteretic curve in Figure 2.8b. The connection between the plate diaphragm to the SHS was fillet weld with leg size approximately 3 mm. The connection of the SHS to the testing apparatus was bolt connection using 4 bolts at top and bottom side of the SHS. Thicker flanges were used at three specimens to reduce the contribution of top and bottom plates deformation.

Square hollow sections were used as the plate boundary to develop 45-degree tension field. The plate slenderness was varied between 24 -59. Two loading protocols (monotonic and cyclic)

were used in this test, i.e. monotonic and cyclic. The cyclic loading protocol followed the ECCS recommendation for simulating ground motion.



(a)



(b)

Figure 2.8 (a) YSPD specimen; (b) Load deformation response of cyclic loading (Chan & Albermani, 2009)

This study concluded that devices with high slenderness ratio could provide good energy dissipation, strength, and ductility. Although inelastic buckling occurred on these specimens, it did not instigate instability on the device. On the other hand, low slenderness device gave unsatisfactory energy dissipation although it did not buckle. This was due to possible bolt slippage and localized deformation of the SHS. In addition, the specimens with stiffened flanges showed better stability behavior, however, due to increase of eccentricity between the specimen center line and the actuator, the energy dissipation was less effective.

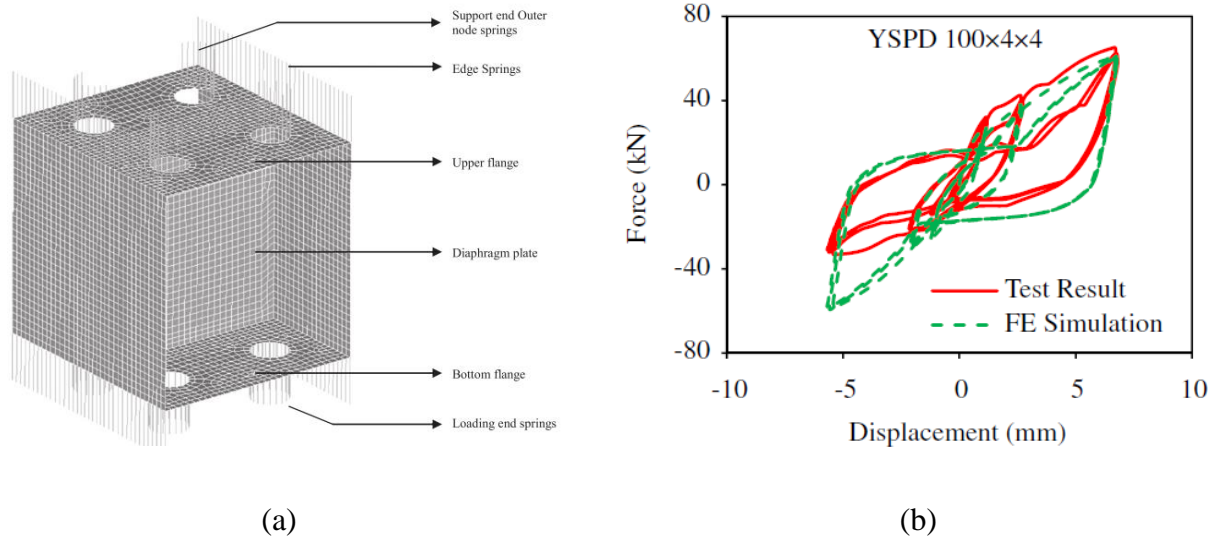


Figure 2.9 (a) Finite element modelling of YSPD; (b) Hysteretic response of YSPD from experiment and FE
(Raquibul Hossain et al. 2011)

In the supplemental numerical study of YSPD (Raquibul Hossain et al. 2011), finite element model on ANSYS and analytical equations to predict yielding force and the elastic stiffness were developed. Figure 2.9a shows the finite element modelling in ANSYS, and Figure 2.9b shows the validation of the numerical modelling by the test result.

The material model was bilinear with kinematic hardening. Both geometric and initial stress imperfections were modelled. Combination of hinges and springs was used to simulate the deformation and movement of the bolts and edges of YSPD. A reduction factor, ϕ , was introduced here to account for the degradation of SHS stiffness due to rotation. Therefore, the finite element model became cumbersome and might not be applicable for different type of YSPD.

The yield force and stiffness of the proposed equations are shown in Figure 2.10. It shows that the analytical equations could predict the behavior of YSPD. The yield force was derived based on pure shear mechanism. However, the stiffness equation derivation was highly affected by the flexibility contributed by the square hollow section (SHS). Therefore, the stiffness equation became very complicated.

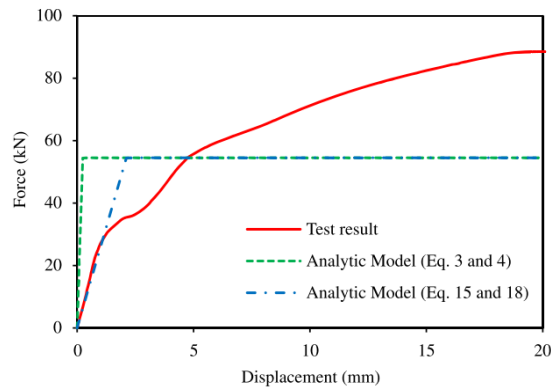


Figure 2.10 Comparison between test result and analytical equation (Raquibul Hossain et al. 2011)

2.3.4 Perforated Yielding Shear Panel Device (PYSPD)

The next development of YSPD is PYSPD by Chan et. al (2013) which introduces perforations at the plate (Figure 2.11). Perforations decrease the in-plane stiffness which reduces the deformation demand of supporting elements. Three type of perforation patterns were studied by both finite element modelling and experimental testing.

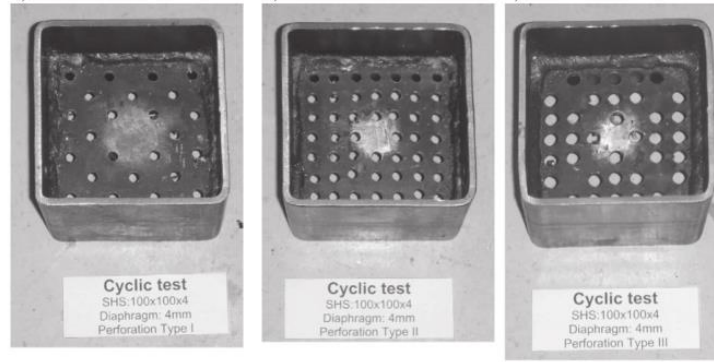


Figure 2.11 PYSPD specimens (Chan & Albermani, 2007)

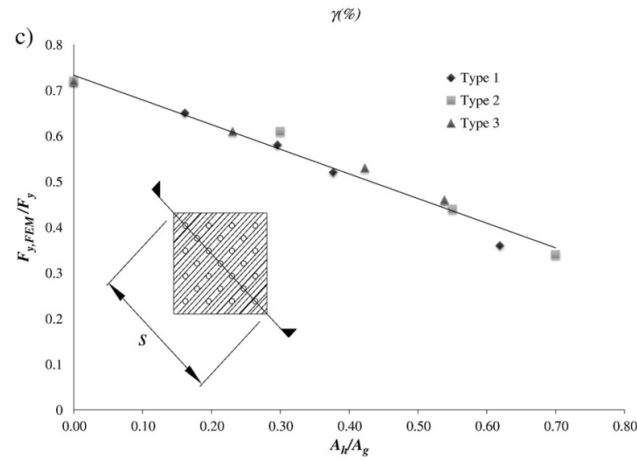


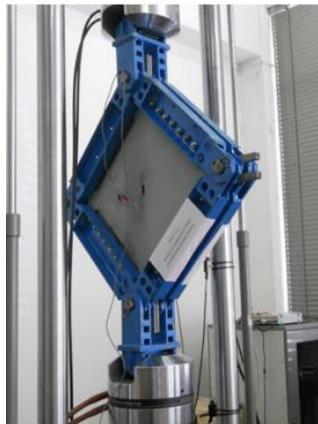
Figure 2.12 Effect of perforation ratio to the yielding force

In PYSPD research couple of holes' patterns were modelled and tested. Based on the experiment it could be observed that the yielding force decreases as the number of holes are increases (Figure 2.12). This was due to the reduction of cross sectional area.

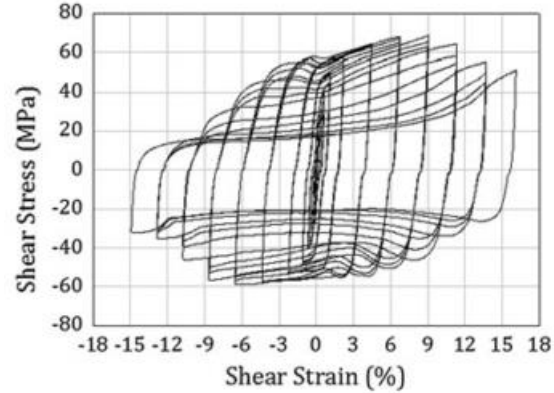
2.3.5 Buckling inhibited shear panels

The application of low-strength metal as a fuse had been explored as an alternative to using regular steel material. Brando et al, (2013) used pure aluminum (EN-AW-1050A) as the yielding material. They conducted experimental study of two specimens, i.e., partially buckling inhibited and fully buckling inhibited panels. Buckling inhibition plate was used to prevent the first four dominant modes of buckling and ultimately improve the performance.

The specimen and the hysteretic result of fully inhibited buckling panel is shown on Figure 2.13. The experimental result showed a stable hysteretic curve. The specimen collapsed at shear strain of 11.37%. Also, it was found that the ultimate shear stress of device was higher than the nominal material shear strength ($\frac{f_y}{\sqrt{3}} = 46.18 \text{ MPa}$).



(a)



(b)

Figure 2.13 Buckling inhibited panel test (Brando et al. 2013)

2.4 Limitation of previous studies

Energy dissipation device using a plate as the yielding device had been studied as some of these researches were presented on the previous sections. The results showed that a metallic yielding device was a reliable damper. However, these studies also showed some limitation of each device.

Dampers that dissipate energy by flexural mechanism (slit and butterfly dampers) show low initial stiffness. This flexibility can compromise the stiffness of the structural system against service load., e.g., wind load. Therefore, the shear yielding device (YSPD) was developed to achieve higher stiffness. YSPD showed that the SHS was too flexible compared to the in-plane stiffness of the diaphragm. Thus, the initial stiffness was affected significantly by flanges deformation. In addition, very limited parametric study had been conducted to provide better understanding of the effect of slenderness ratio and aspect ratio. The equations proposed by the previous study also was not accurate and highly dependable to the boundary condition.

The focus of this thesis is to provide deeper understanding of shear plate fuse made from welded wide flange section. The flanges thickness was designed to avoid prying action and provide better boundary condition. Two analytical equations that provide more accurate prediction of yielding force and stiffness were proposed. Also, investigation on the effect of parameters, such as slenderness ratio, aspect ratio, and size ratio on the behavior were conducted both experimentally and numerically.

2.5 Welded Wide Flange Fuse (WWFF)

Welded wide flange section is commonly available and used worldwide as structural components. Its size versatility makes it very desirable. In addition, this section is economical and easy to be fabricated. Therefore, the application of welded wide flange section as a fuse is desirable. The advantage of using welded wide flange fuse is the size of the flange and the web can be varied as needed. This versatility can answer the various needs of the structural fuse mechanical properties for different structural systems.

Welded wide flange fuse proposed is connected at the flanges to the structural system using bolts. The thickness of the flanges is designed to be able to resist the prying action. So that the flange will not contribute significantly to the flexibility of the fuse. Then, it will be sheared in the longitudinal direction. The bolts connection is designed to be able to resist moment.

In this research, shear fuse is developed by incorporating welded wide flange section. There are several parameters that are observed in this research, such as size ratio, aspect ratio, and slenderness ratio. The results of the experiment are used to validate the numerical model developed in ABAQUS/CAE.

The steel A36 is used as the material of fuse. A36 is a commonly available grade for steel plate. Steel A36 is also very reliable with yield strength of 36 ksi and ultimate strength 58-80 ksi.

The overall differences between WWFF and previous similar steel fuses are summarized in Table 2.1. The application of welded wide flange section is novel and also versatile. Two fix-ends make WWFF installation simpler with less number of bolts needed.

Table 2.1 Comparison of dampers types

Dampers	Slit dampers	Butterfly fuse	YSPD	PYSPD	Buckling inhibited shear panel	Welded Wide Flange Fuse
Element	I-beam	Plate	Thin plate welded inside HSS	Thin plate welded inside HSS	Thin plate	Welded WF
Perforation	Slit holes	Diamond shape	None	Circular hole	None	None
BC	2 fix ends	2 pin ends	2 fix, 2 pin ends	2 fix, 2 pin ends	4 pin ends	2 fix ends
Mechanism	Flexure	Flexure	Shear	Shear	Shear	Shear and flexure

2.5.1 Derivation of design equations

It is important for engineers to have equations to predict the yielding force and stiffness of the fuse for design purposes. The analytical equations to predict the yielding force and the elastic stiffness for the WWFF are derived in this section.

2.5.2 Yielding force

The WWFF dissipates the earthquake energy by a combination of flexure and shear yielding of the web. Figure 2.14 shows the deformed shape and the stress diagram of the WWFF under combined shear and double curvature bending.

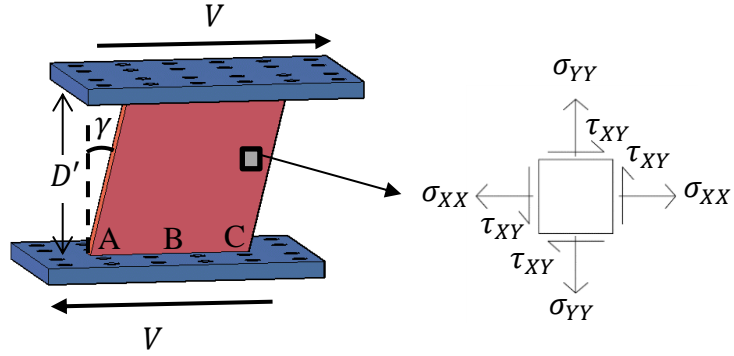


Figure 2.14 Deformed shape and stress diagram of the WWFF under combined shear and double curvature bending

The Von Mises yielding criterion is used to determine the interaction of stresses at the section level. The Von Mises relationships for 2-D problem is expressed as follows:

$$\sigma_y = \sqrt{\sigma_{XX}^2 + \sigma_{YY}^2 - \sigma_{XX}\sigma_{YY} + 3\tau_{XY}^2} \quad (1)$$

Where σ_{XX} and σ_{YY} = normal stress, τ_{XY} = shear stress, and σ_y is the uniaxial yield stress of the material.

Eq. (1) shows that if the yielding is due to axial stress; no shear stress can be applied. Also, when there are no axial stresses applied, the yielding shear stress, τ_y , can be calculated as $0.577\sigma_y$. This condition is called pure shear yielding. In this condition, it is assumed that the yielding condition is due to shear stress only. Based on material mechanics, the pure shear yielding force can be calculated as:

$$V_P = \frac{\sigma_y}{\sqrt{3}} * t_w * a \quad (2)$$

This pure shear yielding mechanism might not be accurate since the distribution of the shear stress is zero at the edge of the section. Furthermore, due to the fixed connection between the flanges and the web, there will be shear-moment interaction.

In this thesis, an equation is proposed to predict the yielding of the fuse. Unlike the pure shear yielding stated before, this equation incorporates both shear and flexure interaction. Figure 2.15 shows the shear stress, τ_{XY} , and axial stress, σ_{YY} , of the WWFF along the length of the web due shear and double curvature bending. As shown in this figure, the shear stress and axial stress varies along the length of the web. To make the calculation simple, an average shear stress, $\tau_{XY,average}$, and average axial stress, $\sigma_{YY,average}$, are used to simulate the combined stress across the web of the WWFF.

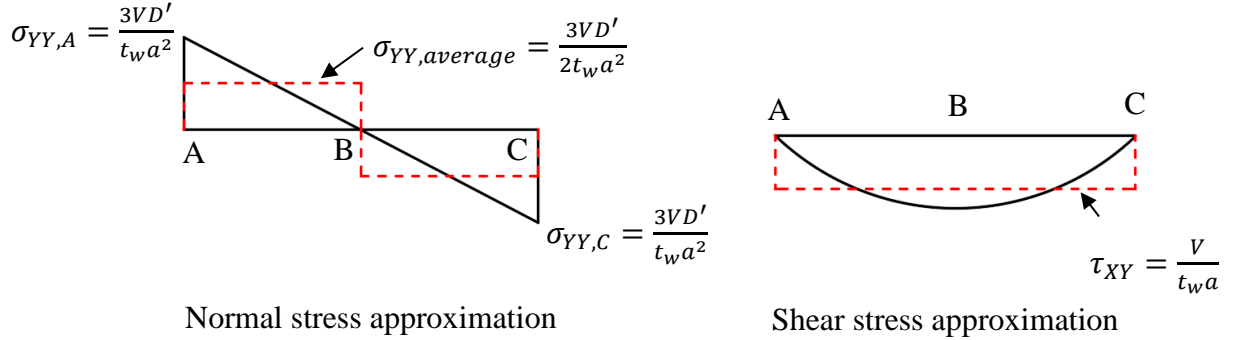


Figure 2.15 σ_{YY} and τ_{XY} across the web

The Von-Mises yielding criteria for two-dimensional problem with $\sigma_{XX} = 0$:

$$\sigma_y = \sqrt{\sigma_{YY}^2 + 3\tau_{XY}^2} \quad (3)$$

The axial stresses distribution profile is assumed to have linear gradient.

$$\sigma = \frac{My}{I} \quad (4)$$

Where the moment of inertia of the web plate is taken as:

$$I = \frac{1}{12} t_w a^3 \quad (5)$$

The average axial stress due to bending is taken at half distance between the neutral axis and the edge of the web.

$$\sigma_{yy,average} = \frac{3M}{t_w a^2} \quad (6)$$

From the equilibrium, the relationship between the moment and shear is:

$$M = 0.5V * D' \quad (7)$$

Substituting M into (6) yields:

$$\sigma_{yy,average} = \frac{3VD'}{2t_w a^2} \quad (8)$$

Substituting the Von Mises yielding criterion with $\sigma_{YY,average} = \frac{3VD'}{2t_w a^2}$ and $\tau_{XY} = \frac{V}{t_w a}$:

$$\left(\frac{3V_y D'}{2t_w a^2} \right)^2 + 3 \left(\frac{V_y}{a t_w} \right)^2 = \sigma_y^2 \quad (9)$$

The equation is then re-arranged by moving the yield shear force to the left side:

$$V_y = \sqrt{\frac{\sigma_y^2}{\left(\frac{3D'}{2t_w a^2}\right)^2 + 3\left(\frac{1}{at_w}\right)^2}} \quad (10)$$

To simplify the equation, the yielding shear force is normalized by the pure shear force (V_p) and substituted by aspect ratio ($A = \frac{a}{D'}$). The normalized shear force is expressed as follows:

$$C_y = \frac{V_y}{V_p} = \frac{2A}{\sqrt{4A^2 + 3}} \quad (11)$$

2.5.3 Initial stiffness

The elastic or initial stiffness is an important property of a fuse. The fuse stiffness affects the stiffness of the building. Furthermore, fuse is expected to provide adequate stiffness against service load such as wind load.

The initial stiffness can be estimated from the combination of shear and flexure displacement.

$$\Delta_{total} = \Delta_f + \Delta_s \quad (12)$$

$$\Delta_{total} = \frac{D'^3}{12EI} V + \frac{D'}{GA_v} V \quad (13)$$

Where the shear modulus is calculated as $G = \frac{E}{2(1+\nu)}$

Dividing the deformation from Eq. (13) with the force applied results the flexibility equation.

$$f = \frac{D'^3}{12E \left(\frac{1}{12} t_w a^3 \right)} + \frac{D'}{GA_V} \quad (14)$$

The shear area for a rectangular section is taken as $A_V = \frac{5}{6} a t_w$.

Substituting the aspect ratio ($A = \frac{a}{D_w}$) and the shear area to the flexibility equation results:

$$f = \frac{1}{E t_w A^3} + \frac{6}{G t_w 5A} \quad (15)$$

Then the flexibility equation is inversed to find the stiffness equation:

$$K = \frac{5EA^3 G t_w}{5G + 6EA^2} \quad (16)$$

The equation above shows that the stiffness of WWFF is linearly proportional to t_w . To compare the stiffness for various plates, it is convenient to normalized the stiffness by dividing the stiffness equation by the web thickness. The result shows that the stiffness of WWFF is linearly proportional to t_w (web thickness).

$$K = \frac{5EA^3 G}{5G + 6EA^2} t_w \quad (17)$$

Chapter 3: Experimental Program

3.1 Introduction

The experimental program consisted of nineteen specimens at Structural Engineering Laboratory at the University of British Columbia. A self-reacting frame that is available at the structural lab was utilized as part of the set up. This reaction frame was connected to the strong floor. The purpose of the test is to investigate the structural behavior of different specimens and validate the numerical modelling. In this chapter, the experiment set up, loading protocol, specimens description, and instrumentations are discussed.

3.2 Experiment Set Up

The experiment set up is designed to generate a shear load in the specimen. Figure 3.1 shows the testing apparatus of this experiment. There are five main parts of the experiment set up: the loading beam (Section 3.2.1), pantograph (Section 3.2.2), mounting (Section 3.2.3), out-of-plane support (Section 3.2.4), and fin extension (Section 3.2.5). The setup was restrained by the pantograph and fin extension on the right and the out-of-plan restraint on the left. With the use of the pantograph, the setup was restraint from rotating in plane, where the WWFF can be tested in the U1 direction without any restraint in the U2 direction. The use of the out-of-plane restraint and the fin prevents the setup from both translating and rotating out of plane. The specimen was connected to the loading beam and the mounting at the flanges using moment-resisting bolts

connections. The experimental set-up was donated and fabricated by George Third and Sons, Custom Plate & Profiles, and Pacific Bolts.

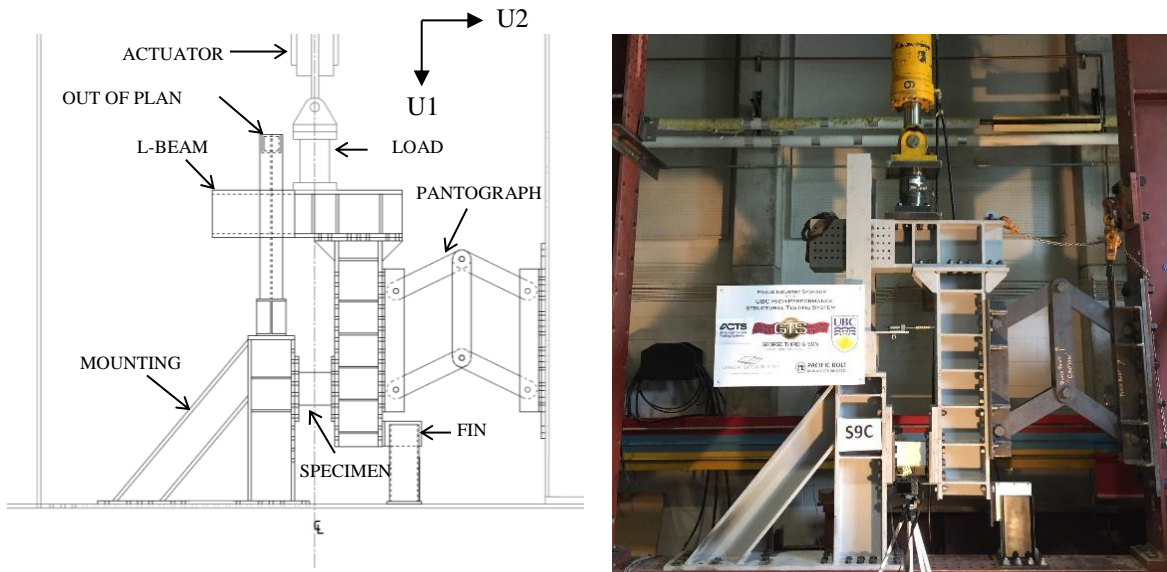


Figure 3.1 Experimental Setup

3.2.1 Loading beam (L-beam)

An L-shaped beam was used as the loading beam in the experiment as shown in Figure 3.2. The actuator and the load cell were connected to the loading beam at the top part at the center line of the specimen. The centered location of the actuator is to eliminate or minimize the axial load on the pantograph due to the eccentricity. The vertical part of the loading beam was connected to the specimen flange and to the pantograph at the opposite side.

The loading beam was fabricated using two W12x106 sections. The horizontal length is 130 cm and the vertical part is 110 cm.

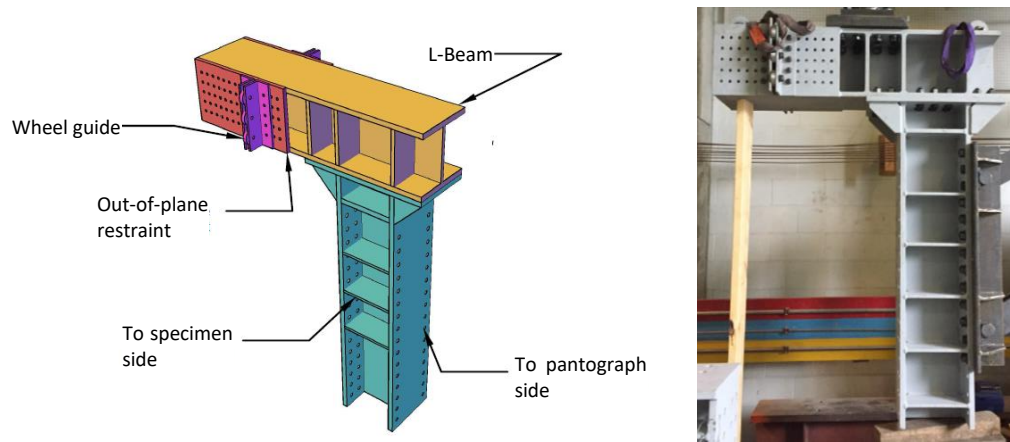


Figure 3.2 Loading beam

3.2.2 Pantograph

Figure 3.3 shows the pantograph system used in this experiment. To assure the verticality of the loading beam, a pantograph system was installed at the opposite side of the L-beam. The pantograph is an all-pinned struts system that allow the translational movement, but restricts the rotational movement. In other words, the L-beam is not restricted from translational (up, down, left and right) movement, but the rotation is restrained. The diagonal struts were 50 cm and the vertical struts were 70 cm. This configuration has a range of horizontal motion from 75 cm to 105 cm.

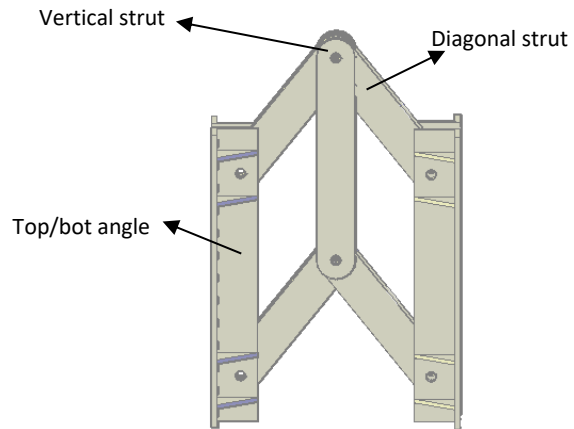


Figure 3.3 Pantograph system

3.2.3 Mounting

The mounting acted as a support for the specimen (see Figure 3.4). This mounting was fabricated with a W12X106 section for the vertical beam and W10X88 for the diagonal beam or the ‘kickback’. Both of these beams were connected to a single base plate. This base plate was connected to the base beam of the self-reacting frame. This mounting was 115 cm height. The diagonal beam was connected in 50° angle from the base plate. The bolt hole pattern at the vertical beam matched the pattern at the loading beam.

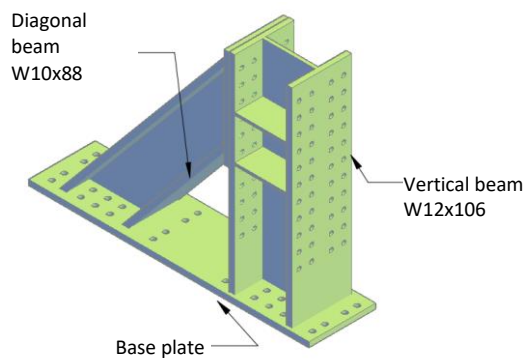


Figure 3.4 Mounting

3.2.4 Out-of-plane support

The out-of-plane support was connected to the top part of the vertical beam. The wheels at the loading beam acted as a guide.

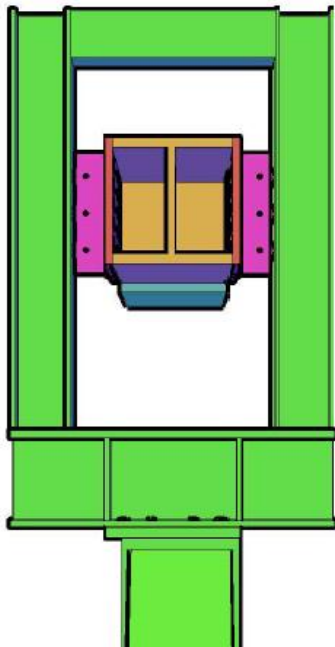


Figure 3.5 Out-of-plan support

3.2.5 Fin extension

To restrict the out-of-plan movement at the lower part of the L-beam, a fin extension was installed at the lower right corner of the L-beam below the pantograph. This structure was 40 cm height.

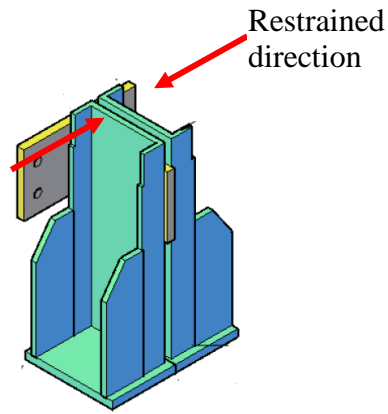


Figure 3.6 Fin extension

3.3 Loading mechanism

This test set up configuration was designed to subject the specimen with the shear load at both flanges. The support reactions and the internal force diagrams due to this loading are presented on Figure 3.7. The internal shear force of the specimen is uniform throughout the element with the same magnitude of the actuator force. The moment reaction (M) at both ends was assumed to have the value of $M = 0.5VD_w$, with an inflection point at the middle.

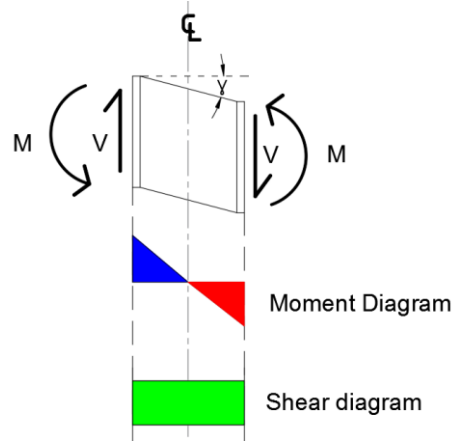


Figure 3.7 Loading mechanism of the specimen

As shown in Figure 3.8, the actuator's center line coincides with the specimen center. This means no eccentricity between the actuator and the specimen center mid-point, hence the force in the pantograph could be minimized. However, the axial force at the pantograph (N1 and N2) will change the inflection point in the specimen and cause the end moment of the specimen to be slightly different. The nature of accidental eccentricity and fix connection between the specimen and the loading beam will create axial loads on the pantograph. For simplicity, this discrepancy was ignored in this study.

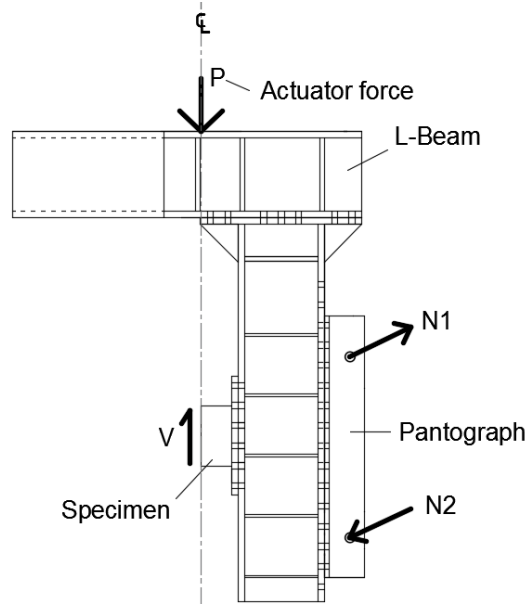


Figure 3.8 Pantograph force

3.4 Specimen design

The WWFF specimen was fabricated from three plates (two flanges and one web). The specimens were built using the A36 steel material. The web plate was fillet-welded at the center line of the flanges. The weld grade used was E49XX. The fillet weld size used depends on the thickness of the web.

The flanges had moment connection bolts patterns at both ends. There were two types of typical flange used. Flange A had larger dimension than Flange B to accommodate the web size and also provide higher moment capacity.

The displacement of the specimen depended on its web depth. Based on the previous studies, the maximum drift of the fuse could go up to 15-30%. The depth of the specimen then was also

selected based on the 30% depth as the maximum displacement. The actuator stroke limited the maximum displacement of the specimen.

Both flanges were designed to have an adequate thickness to prevent them to affect the stiffness significantly. The thickness was determined by minimum thickness of bolts in tension and prying action from CSA. Based on the magnitude of the prying action two different thicknesses were selected, 19 mm and 25 mm.

3.5 Test matrix

Based on the proposed equations and the objectives of this study, the testing matrix of the experiment was developed. There were total of 19 specimens tested. The specimens were built using the A36 steel material. The expected yielding stress of 285 MPa was used. Ten specimens were cyclic tested, and nine specimens were subjected to monotonic loading. All unique specimens' type is presented in Table 3.1.

Table 3.1 Test matrix

Specimen	Web Thk	Length	Depth	Net Depth	S	A	Flange Thk	Flange type	Loading
	t_w	a	D	$D' = D - 2t_w$	$\frac{D'}{t_w}$	$\frac{a}{D'}$	t_f		
	[mm]	[mm]	[mm]	[mm]			[mm]		
A0.75S22s	4.8	78.6	114.3	104.8	22.0	0.75	19	B	M,C
A075S22-1.3	6.4	104.8	152.4	139.7	22.0	0.75	19	B	M,C
A075S22-2	9.5	157.2	228.6	209.6	22.0	0.75	25	A	M,C
A1.5S22	4.8	157.2	114.3	104.8	22.0	1.50	19	B	M,C
A2S22	4.8	209.6	114.3	104.8	22.0	2.00	19	A	M,C
A0.75S32	4.8	114.3	161.9	152.4	32.0	0.75	19	B	M,C
A1.5S32	4.8	228.6	161.9	152.4	32.0	1.50	19	A	M,C
A2S32	4.8	304.8	161.9	152.4	32.0	2.00	25	A	M,C
A0.75S43	4.8	152.4	212.7	203.2	42.7	0.75	19	B	M,C
A1.5S43	4.8	304.8	212.7	203.2	42.7	1.50	25	A	C

*M=monotonic, C=cyclic

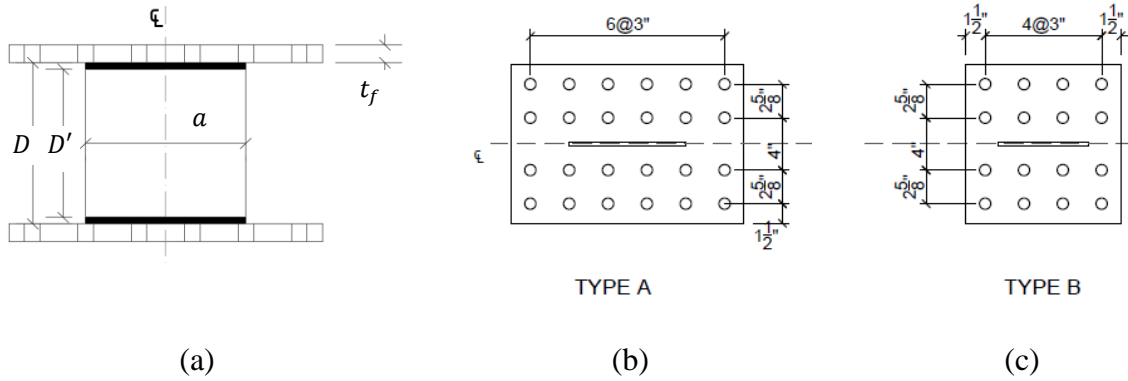


Figure 3.9 Typical specimen geometry

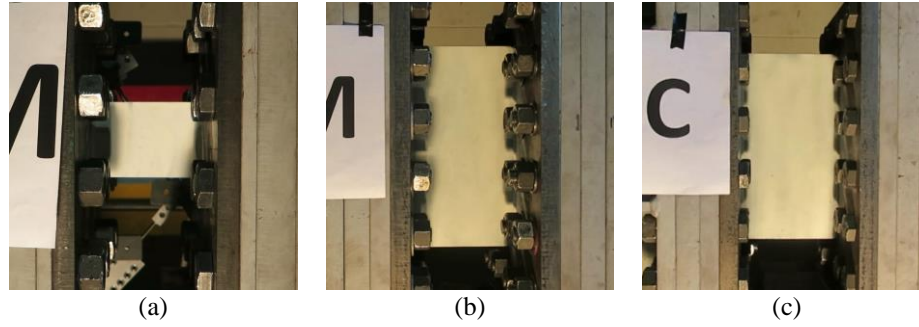


Figure 3.10 WWFF specimens (a)A1.5S0.75 (b)A1.5S32 (c) A2S32

3.5.1 Size ratio study

In size ratio study, the slenderness ratio and the aspect ratio are kept equal, but the specimen size was geometrically scaled. There were three specimens type studied, i.e., A0.75S22, A0.75S22-1.3, and A0.75S22-2. Specimen A0.75S22-1.3 and A0.75SR22-2 were geometrically scaled based on A0.75S22 with the scale factor 1.3 and 2 respectively. Whereas their slenderness ratio and aspect ratio were 22 and 0.75 respectively. The results on overall behavior (yield force, energy, hysteretic behavior) are observed.

Table 3.2 Testing matrix for size ratio study

Specimen	Web Thk	Length	Depth	Net Depth	S	A	Size Ratio to S1
	t_w	a	D	$D' = D - 2t_w$	$\frac{D'}{t_w}$	$\frac{a}{D'}$	
	[mm]	[mm]	[mm]	[mm]			[-]
A0.75S22	4.8	78.6	114.3	104.8	22.0	0.75	1
A075S22-1.3	6.4	104.8	152.4	139.7	22.0	0.75	1.3
A075S22-2	9.5	157.2	228.6	209.6	22.0	0.75	2

3.5.2 Aspect ratio study

Aspect ratio is defined as the ratio of the width (a) to the depth of the web (D'). There were 2 sets of 3 specimens were tested. The first set had a slenderness ratio of 22, while the other set had a slenderness ratio of 32. The aspect ratio of the specimens varied from 0.75 to 2.0. Based on the preliminary analysis, one can observe that the yielding point and the stiffness change with the changes of the aspect ratio.

Table 3.3 Testing matrix for aspect ratio study

Specimen	Web Thk	Length	Depth	Net Depth	S	A
	t_w	a	D	$D' = D - 2t_w$	$\frac{D'}{t_w}$	$\frac{a}{D'}$
	[mm]	[mm]	[mm]	[mm]		
A0.75S22	4.8	78.6	114.3	104.8	22.0	0.75
A1.5S22	4.8	157.2	114.3	104.8	22.0	1.50
A2S22	4.8	209.6	114.3	104.8	22.0	2.00
A0.75S32	4.8	114.3	161.9	152.4	32.0	0.75
A1.5S32	4.8	228.6	161.9	152.4	32.0	1.50
A2S32	4.8	304.8	161.9	152.4	32.0	2.00

3.5.3 Slenderness ratio study

Slenderness ratio is defined as the ratio of the web depth to the web thickness. The slenderness ratio observed in this experiment is divided into three ranges: low (<30), mid (30-40), high (>40). The slenderness ratio effect was studied for two different aspect ratios: 0.75 and 1.5. For each aspect ratio, three specimens represented three different slenderness ratio ranges were tested.

Table 3.4 Testing matrix for slenderness ratio study

Specimen	Web Thk	Length	Depth	Net Depth	S	A
	t_w	a	D	$D' = D - 2t_w$	$\frac{D'}{t_w}$	$\frac{a}{D'}$
	[mm]	[mm]	[mm]	[mm]		
A0.75S22	4.8	78.6	114.3	104.8	22.0	0.75
A0.75S32	4.8	114.3	161.9	152.4	32.0	0.75
A0.75S43	4.8	152.4	212.7	203.2	42.7	0.75
A1.5S22	4.8	157.2	114.3	104.8	22.0	1.50
A1.5S32	4.8	228.6	161.9	152.4	32.0	1.50
A1.5S43	4.8	304.8	212.7	203.2	42.7	1.50

3.6 Instrumentations

3.6.1 Actuator

The actuator used in the test was made by Sealum with a capacity of 650 kN and stroke limit of +/- 150mm. Both ends were swivel head. This actuator had no force or displacement feedback. Control was conducted using the displacement control feedback from linear pots.

The actuator was connected at the top beam of the self-reacting frame, facing down. The swivel part was in the in-plane direction which means that the out-of-plan rotation of the actuator was restrained. Figure 3.11 shows the actuator used in this study.



Figure 3.11 Actuator

3.6.2 Load Cell

A load cell was mounted between the actuator's end and the L-beam. The load cell used in this study (Figure 3.12) was MTS 661.31 with a capacity of 1300 kN. Two adapter plates were used to connect the load cell to the load beam and the actuator.



Figure 3.12 Load cell

3.6.3 Displacement sensors

Several linear pot instruments were installed on the test set up. Two of the linear pots (LP1 and LP2) were used as the control feedback to move the actuator (displacement control). The list of linear pots is presented in Table 3.5.

Table 3.5 Linear pot list

No.	Name	Type	Model	Tip Point
1	LP1	Linear pot	TEX0100	A
2	LP2	Linear pot	TEX0100	A
3	LP3	Linear pot	TEX0050	B
4	LP5	Linear pot	TEX0300	Actuator

The linear pots were installed in between the inner sides of the flanges. This ensures that the effect of the slippage in the displacement reading could be avoided. The configuration of this linear pot is presented in Figure 3.13. The tip of both LP1 and LP2 were connected to the same point (A) at the top flange (L-beam side). Whereas, the base was connected to the other flange (mounting side). This triangular configuration allowed the tracking of point A coordinate in 2-dimensional space. The displacement in U1 direction of point A was used as the control feedback. LP3 recorded the displacement of point B in U2 direction only. The displacement in U2 direction of point A and B then was compared to monitor the in-plane rotation.

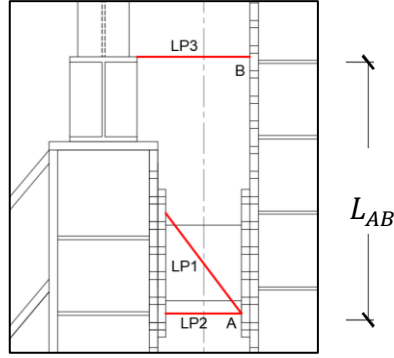


Figure 3.13 Linear pots layout

The linear pots measured the displacement of point A. These measurements then were converted as a point's coordinate. Figure 3.14 shows geometric transformation of the linear pots reading to coordinate. The relationship between the linear pots reading and the displacement is presented at Eq. (18) and (19). The displacement at certain time-j is calculated as the difference between the coordinate at that time-j (X_j, Y_j) and the initial coordinate ($X_{initial}, Y_{initial}$). After the specimen was secured between the loading beam and the mounting, the linear pots were installed on the pre-drilled holes.

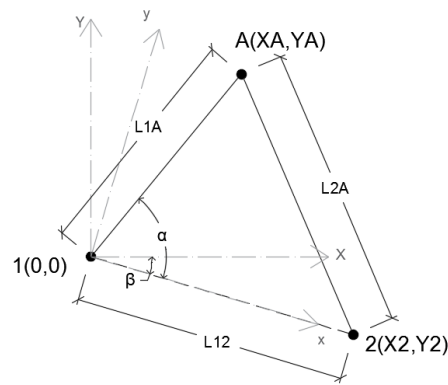


Figure 3.14 Geometric relationship of the linear pots configuration

$$X_A = x_A \cos(\beta) - y_A \sin(\beta) * \text{sign}(Y2) \quad (18)$$

$$Y_A = y_A \cos(\beta) + x_A \sin(\beta) * \text{sign}(Y2) \quad (19)$$

The rotation of the specimen was calculated as:

$$\frac{U2_A - U2_B}{L_{AB}} \quad (20)$$

3.7 Free run

Prior to testing, a free run procedure was conducted. This running was conducted without any specimen attached. This procedure purpose was to determine the additional load due to the friction and self-weight of the experiment set up. The load reading from the load cell in this free run shows the load taken by test set up from friction and self-weight. This reading would later be subtracted from the experimental force reading.

3.8 Loading protocol

3.8.1 Monotonic

One of the loading protocol applied in this study is monotonic push over load with vertical direction (U1 positive). The loading was applied until fracture occurred or when the instrumentations reached their stroke capacity.

3.8.2 Quasi-static

The quasi-static loading protocol of this experiment adopted AISC 341-16 requirement for beam-to-column connections with some additional cycles. Additional cycles in smaller drift was added to observe the elastic behavior of the fuse (Table 3.6). The loading protocol consists of two cycles of 0.002 drift ratio (defined using the displacement in the U1 direction divided by the clear distance of the web (D')), followed by six cycles of 0.00375, 0.005, 0.0075, four cycles of 0.01 and two cycles of 0.015, and increments of 0.01 until 0.05 drift ratio. Figure 3.15 shows the loading protocol applied to the model.

Table 3.6 Quasi-static drift loading

No.	Number of cycle	Drift ratio (γ_{total})	No.	Number of cycle	Drift ratio (γ_{total})	No.	Number of cycle	Drift ratio (γ_{total})
1	2	0.002	11	2	0.06	21	2	0.16
2	6	0.00375	12	2	0.07	22	2	0.17
3	6	0.005	13	2	0.08	23	2	0.18
4	6	0.0075	14	2	0.09	24	2	0.19
5	4	0.01	15	2	0.1	25	2	0.20
6	2	0.015	16	2	0.11	26	2	0.21
7	2	0.02	17	2	0.12	27	2	0.22
8	2	0.03	18	2	0.13	28	2	0.23
9	2	0.04	19	2	0.14	29	2	0.24
10	2	0.05	20	2	0.15	30	2	0.25

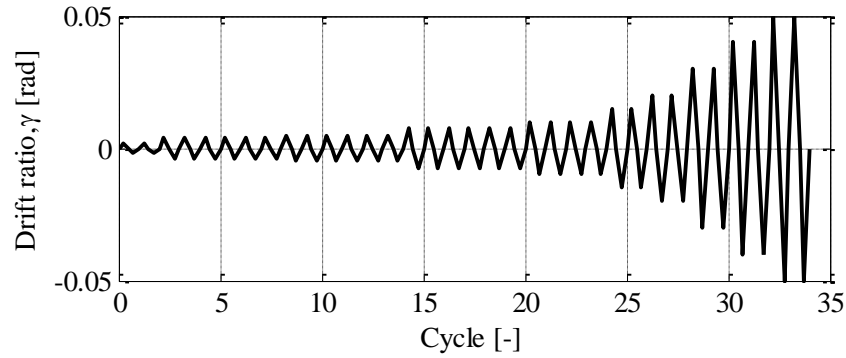


Figure 3.15 Loading protocol for Quasi-static

3.9 Testing procedure

The specimens had temporary bracings installed at 4 corners to protect the web from accidental loading or damage during delivering and moving process. These braces then were removed when the specimen was ready to be installed.

Some preparation work needed to be done before testing. Three sets of two bolt holes were drilled to each specimen to install the instrumentation mounting. All instrumentation was mounted on the back side of the specimen, while the other side of the web was white washed.

The specimen was carefully mounted to designated bolt holes using 7/8" bolts. Adapter plates were used to adjust the space in between if necessary. After the specimen and the displacement sensors were installed properly, the test was conducted.

Come-along chain was installed at the top of the L-beam as a safety line. To minimize the sudden change of the force coming to the actuator, the valve at the outgoing hydraulic line was

slowly loosened to give time for the actuator to adjust the pressure. The test was conducted until the failure of the specimen or until the capacity of instrumentations reached.

Chapter 4: Experimental Result

4.1 Introduction

This chapter presents the result of the experiment program on nineteen WWFF specimens explained in Chapter 3. The output obtained from the test was force-displacement relationship for each loading protocol. This result then compared to the proposed analytical equations for predicting the yielding force and stiffness. Furthermore, the observations of the specimens' behavior during the experiment are reported.

4.2 Free run result

As mentioned before, a free-run was conducted to measure the gravity force from the experimental set up. From the free-run we obtained that the hanging part of the apparatus caused an additional load of 8 kN. This force was later added to the force reading from the load cell with the direction of gravity.

4.3 Cyclic results

Ten WWFF were tested with cyclic loading. The force-drift relationship and the photos at different drifts for each specimen were presented below.

4.3.1 A0.75S22

A0.75S22 had slenderness ratio of 22 and aspect ratio 0.75. The shear force versus drift ratio relationship is presented in Figure 4.1, while Figure 4.2 shows the specimen at different drifts. It can be observed that the force started to degrade after ultimate drift ratio of 3%, and yielding occurred near the weld with two horizontal parallel lines shape on the web. The degradation becomes noticeable at 5% drift due to more yielding and slight buckling. The parallel lines were also more noticeable at this drift. At 6% drift, the buckling became more severe along with fracture at the welding zone. A0.75S22 then fractured at 7%.

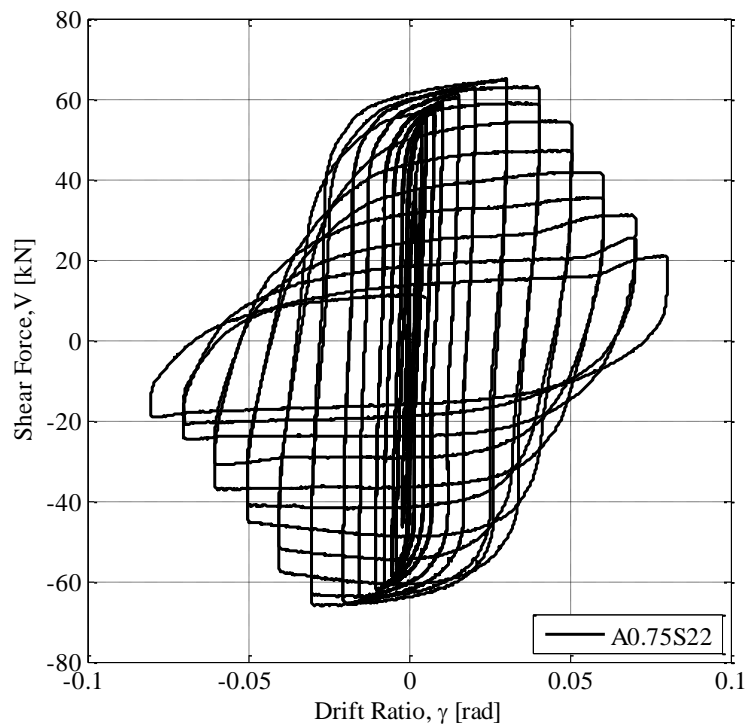


Figure 4.1 Force-drift of A0.75S22

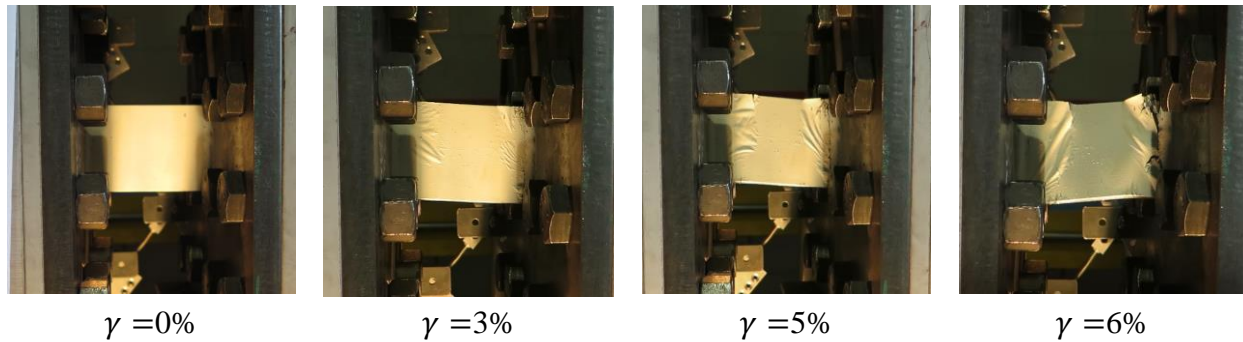


Figure 4.2 A0.75S22 at different drifts

4.3.2 A0.75S22-1.3

A0.75S22-1.3 was geometrically scaled by 1.3 to A0.75S22-1. Figure 4.3 shows the force-drift relationship of this WWFF and Figure 4.4 shows the specimen during the test. The maximum force occurred at 3% drift and started to degrade after that. The specimen showed yielding near the welding zone at 3% drift. At 5% drift the force showed more severe degradation due to buckling and further yielding. However, A0.75S22-1.3 failed at 8% drift because of fracture along the welding zone on the right side (L-beam).

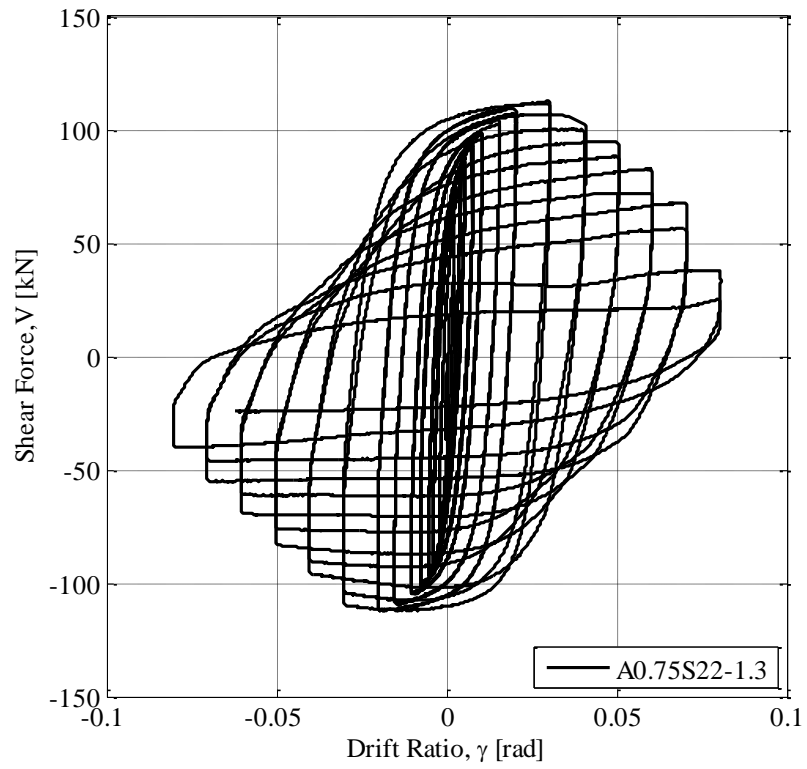


Figure 4.3 Force-drift of A0.75S22-1.3

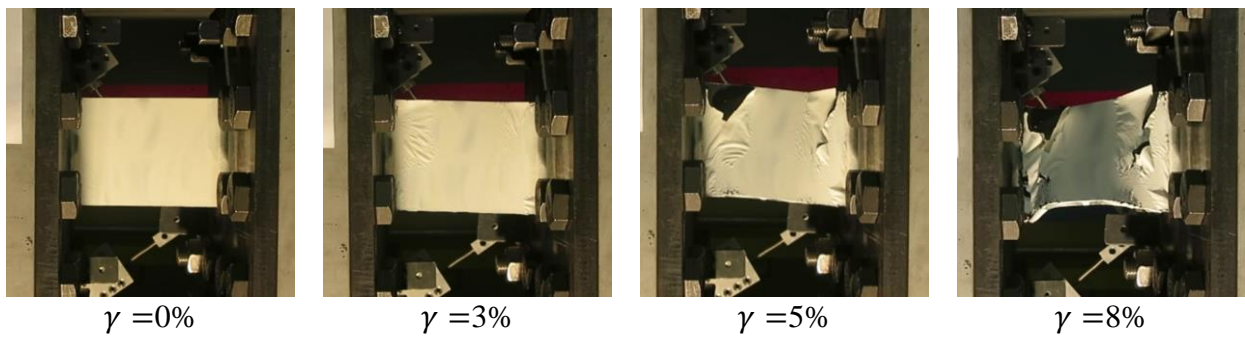


Figure 4.4 A0.75S22-1.3 at different drifts

4.3.3 A0.75S22-2

A0.75S22-2 was twice as large as A0.75S22, but had the same slenderness ratio and aspect ratio. Force-drift ratio obtained from the test is shown in Figure 4.5, and the specimen photos for different corresponding drifts are shown in Figure 4.6. At 4% ultimate drift ratio, yielding was observed at the corner of the web. The force started to degrade at 5% drift. This behavior occurred due to buckling and yielding of the specimen. The force continued to drop and fractured at the edge of welding zone occurred at 7%. The maximum drift was 9% with fracture across the welding zone at the left side (mounting).

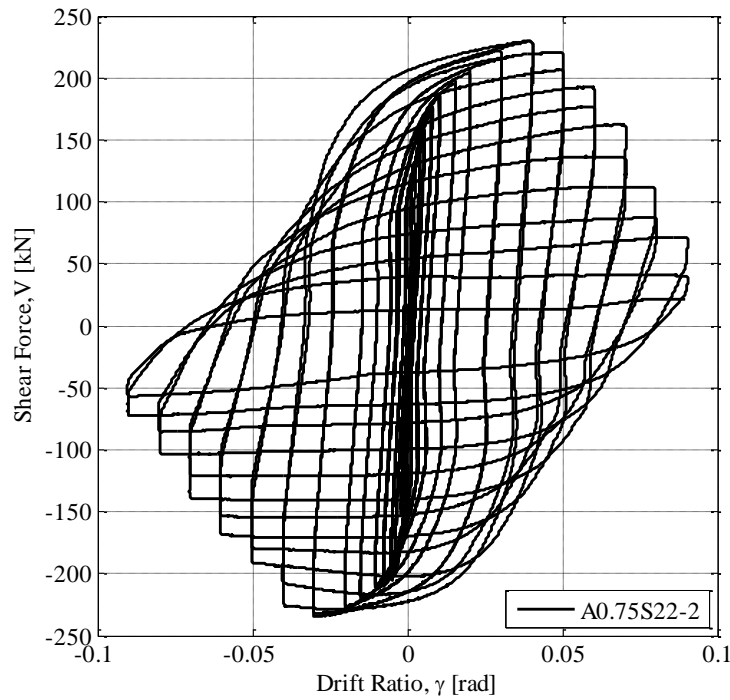


Figure 4.5 Force-drift relationship of A0.75S22-2

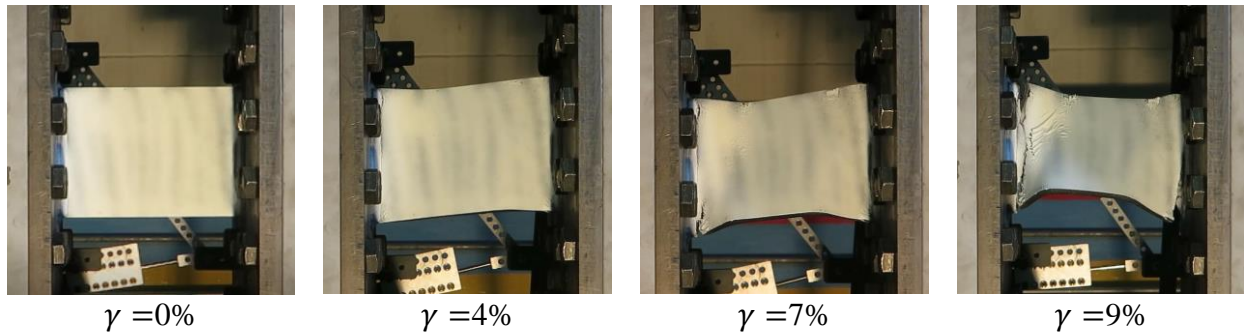


Figure 4.6 A0.75S22-2 at different drifts

4.3.4 A1.5S22

A1.5S22 was a low slenderness ratio specimen (22) with aspect ratio of 1.5. At 3% drift ratio, the force reached ultimate force and started to degrade afterwards. Some yielding pattern was noticeable near the edge. From Figure 4.7, it can be observed that the force started to degrade at 5% drift. Corresponding to this drift, the specimen showed shear yielding behavior at the middle part of the web (Figure 4.16). Towards the peak of in 6% and 7% drift cycles, there is a slight increase of force in U1 positive due to development of tension field. However, it is not significantly shown in the specimen. The specimen fractured near the welding zone at 6% drift and failed at 7%.

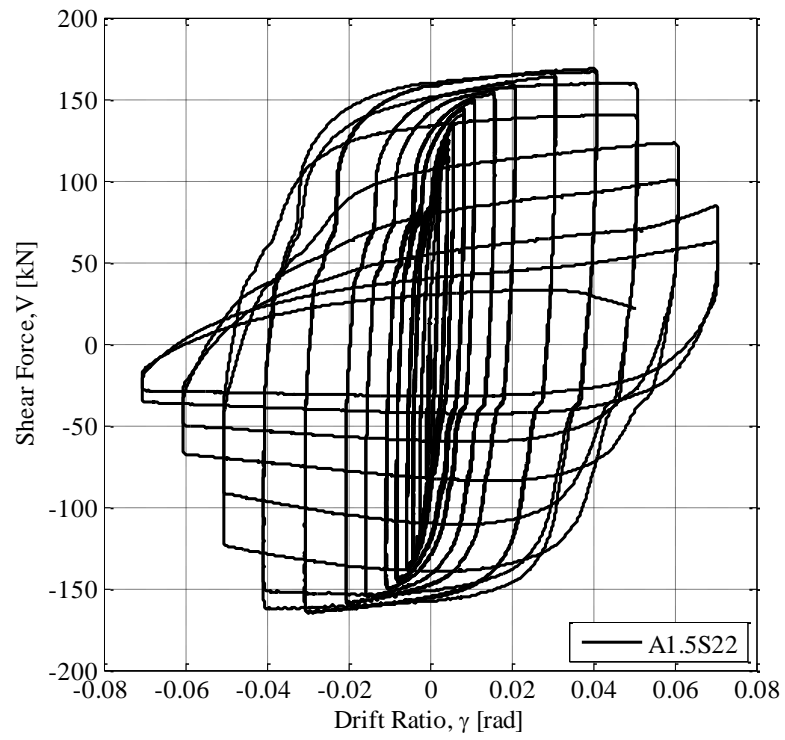


Figure 4.7 Force-drift relationship of A1.5S22

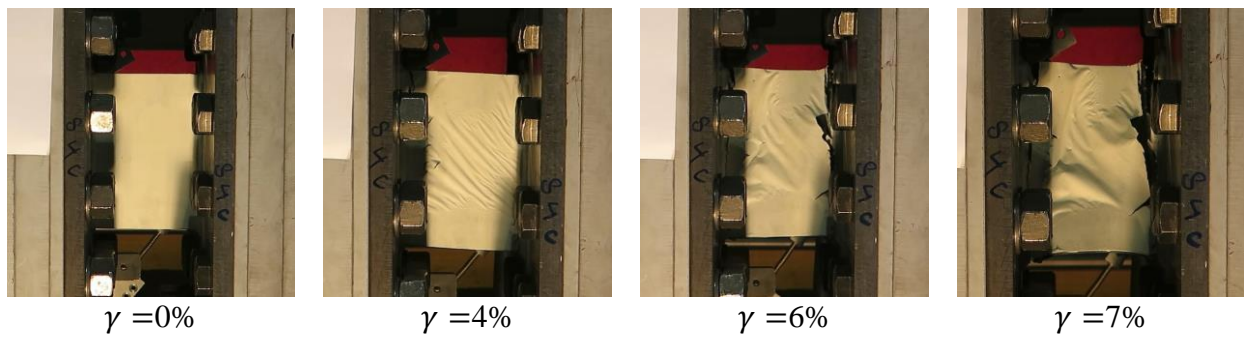


Figure 4.8 A1.5S22 at different drifts

4.3.5 A2S22

A2S22 had slenderness ratio of 22 and aspect ratio of two. The force-drift relationship is presented on Figure 4.9 and the specimen at different drifts in Figure 4.10. The specimen reached the ultimate drift ratio at 4% drift. The yielding pattern propagated from the weld to the center of the web. Force degradation occurred at 5% drift. At this drift, the specimen showed shear yielding in the web, but no significant buckling observed. The force dropped significantly at 6% drift due to buckling and tear at the end of the welding. The buckling stretched diagonally between the weld. A tear through occurred along the welding zone at 7% drift.

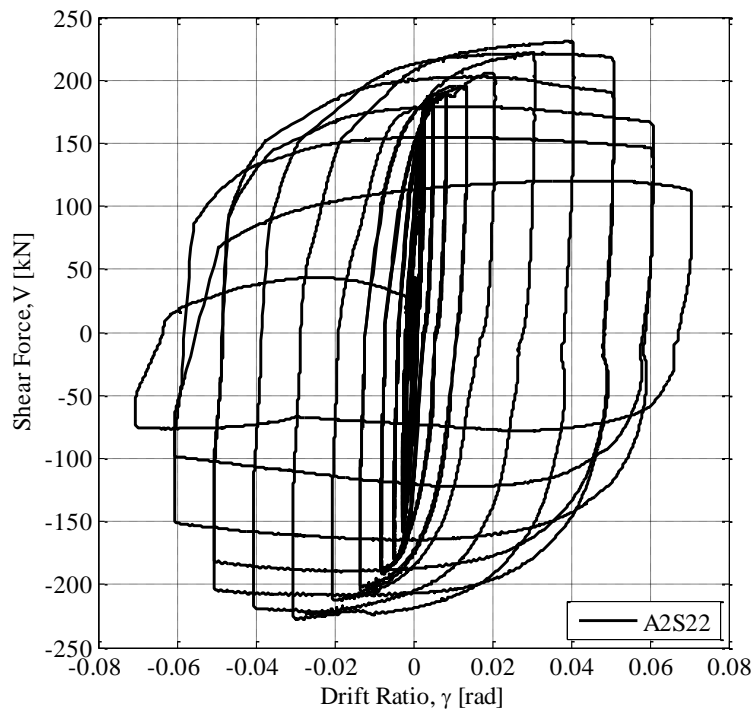


Figure 4.9 Force-drift relationship of A2S22

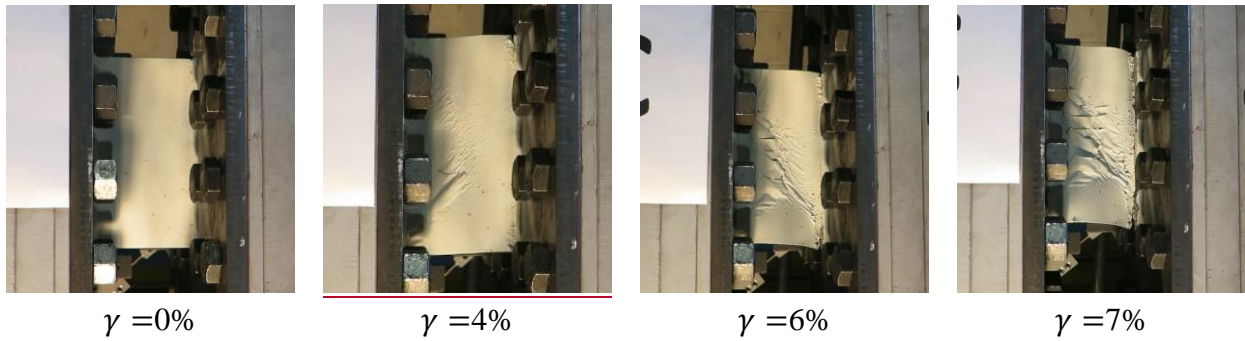


Figure 4.10 A2S22 at different drifts

4.3.6 A0.75S32

A0.75S32 was a mid-slenderness ratio with aspect ratio of 0.75. The force-drift relationship is presented in Figure 4.11 and the specimen at different drifts in Figure 4.12. The hysteretic curve shows pinching behavior. The force started to degrade after reaching the ultimate drift ratio at 1%. There was no noticeable damage at the specimen. At 7% drift ratio, the specimen buckled out of plane with two parallel lines in the middle off the web. Also, small tear started to form at the end of the buckling lines. The tear grew bigger with additional tear near the welding area. The specimen failed at 10% drift.

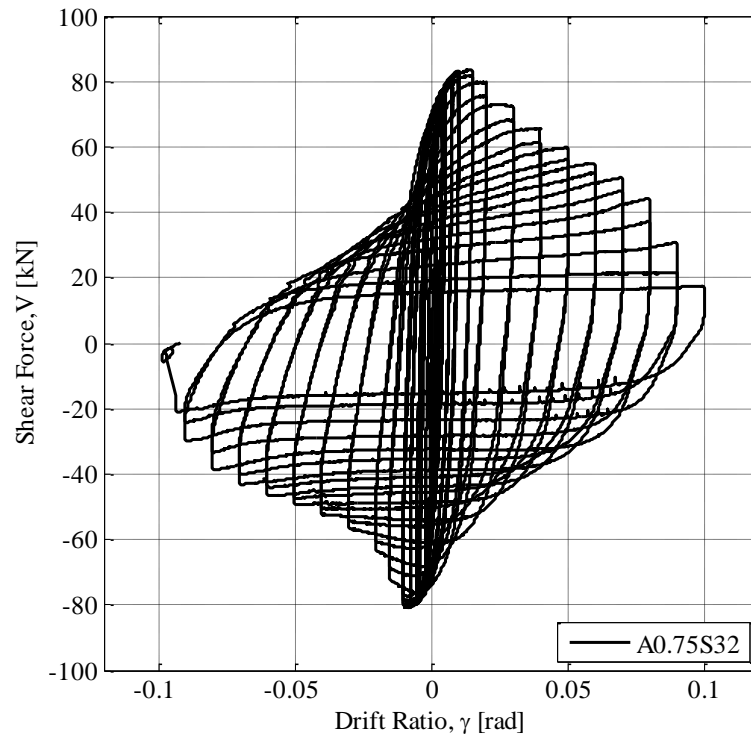


Figure 4.11 Force-drift relationship of A0.75S32

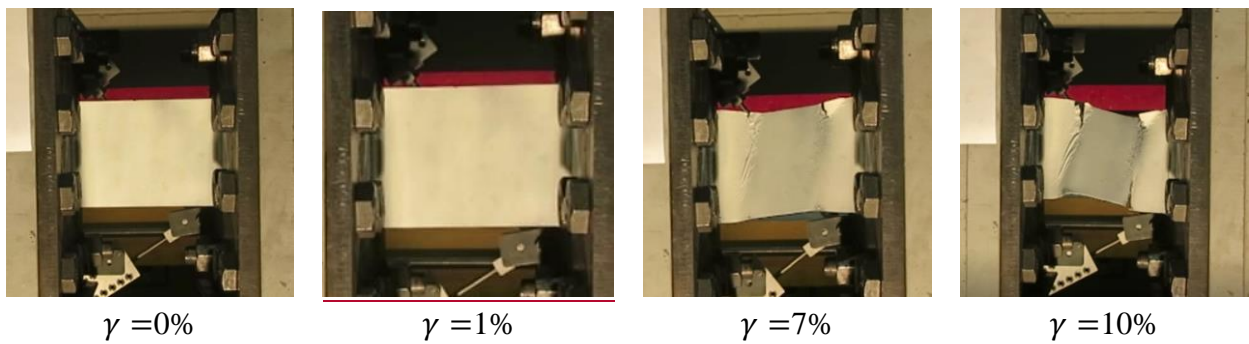


Figure 4.12 A0.75S32 at different drifts

4.3.7 A1.5S32

Force-drift relationship of A1.5S32 and the specimen photos at different drifts are presented in Figure 4.13 and Figure 4.14 respectively. The force started to degrade after reaching the ultimate drift ratio at 1%. There was no noticeable damage at the specimen. At drift 5% shown that the specimen buckling with two diagonal (X-shape) buckling shape. At 7% the force continued to degrade, and the buckling became more severe. This specimen showed fractured at the buckling zone and the welding zone. The test was stopped after 11% due the severity of the fracture.

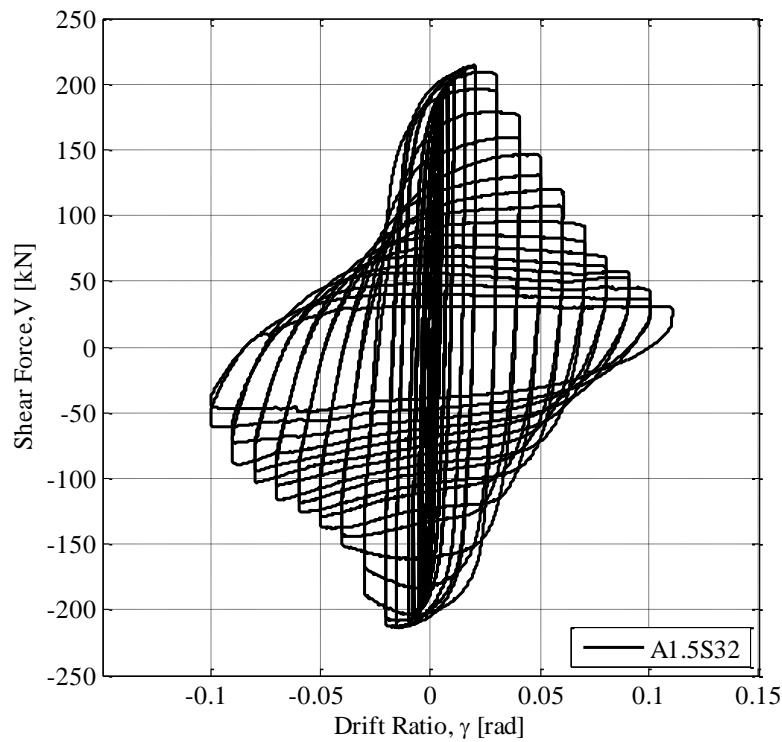


Figure 4.13 Force-drift relationship A1.5S32

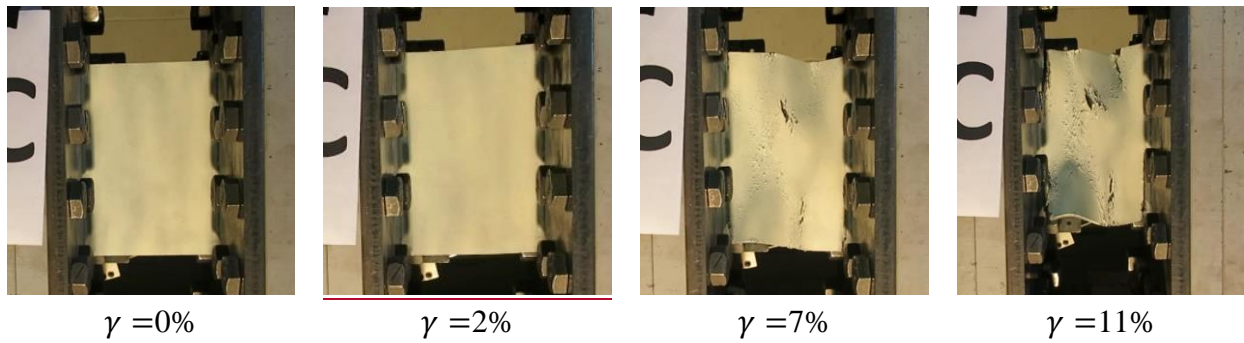


Figure 4.14 A1.5S32 at different drifts

4.3.8 A2S32

Figure 4.15 shows the force-drift relationship of A2S32. The picture of the specimen during the test is shown in Figure 4.16. The ultimate force was reached at 3% drift. Corresponding to this drift, the specimen showed no significant damage. The hysteretic curve degrades at 5% drift. At further cycle, this diagonal buckling shape started to form a X-shape, followed by the decrease of force. The fracture occurred at the buckling zone and welding zone (drift 13%).

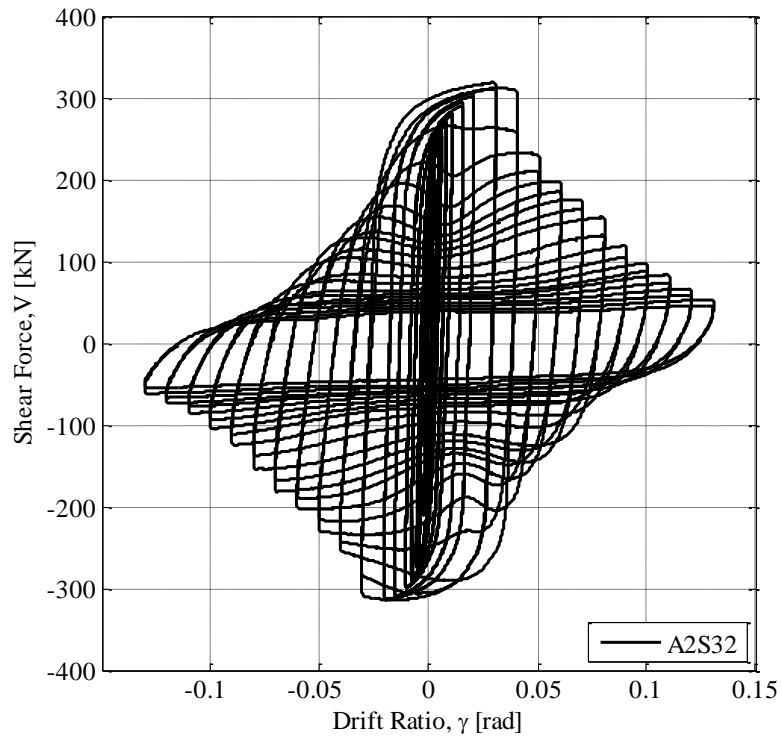


Figure 4.15 Force-drift relationship of A2S32

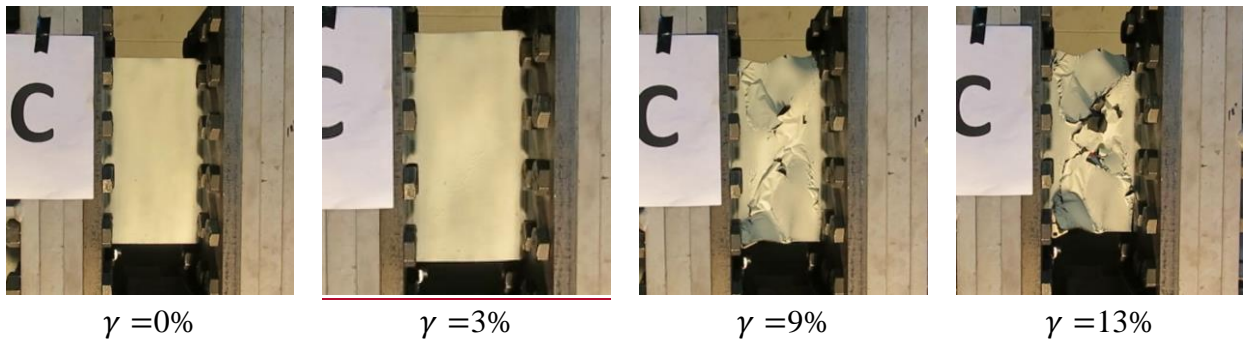


Figure 4.16 A232 at different drift

4.3.9 A0.75S43

A0.75S43 had a high slenderness ratio of 42.7; and its aspect ratio was 0.75. Hysteretic curve of force-drift relationship is shown in Figure 4.19. The photos of specimen during experiment are presented in Figure 4.18. The hysteretic shows pinching behavior. At drift ratio of 0.5%, the force reached ultimate and started to degrade afterwards. This was earlier than the other specimen with lower slenderness ratio. Buckling shape was two horizontal line across the web (from free end to free end). The fracture initially occurred at the welding zone then at the buckled part. The fracture then propagated across these buckling lines. The test was stopped due to testing apparatus limitation.

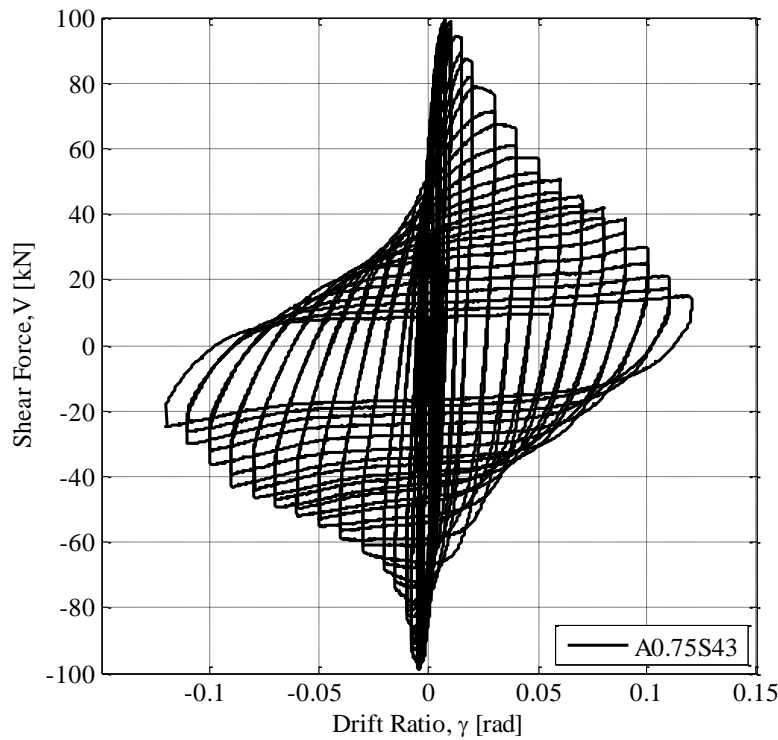


Figure 4.17 Force-drift relationship of A0.75S43

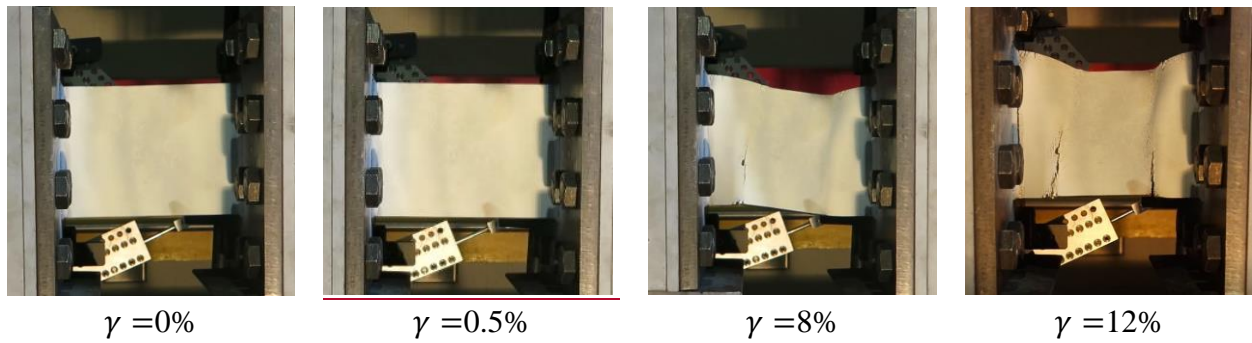


Figure 4.18 A0.75S43 at different drifts

4.3.10 A1.5S43

A1.5S43 had 42.7 slenderness ratio with 1.5 aspect ratio. The fore-drift relationship is shown in Figure 4.19 and the specimen photos are in Figure 4.20. The ultimate drift was reached at 0.8%. However, there was no significant damage shown during the test. At 8% drift, the force showed continuation of force degradation, while the specimen shows buckling happened at the web. From the photos, it can be observed that the buckling happened in diagonal shape across the web from the welding part to the opposite welding zone. Due to cyclic loading, the diagonal buckling of the mirror direction occurred and hence the X-buckling shape occurred in the web. Fracture propagated from the middle part of the web in this X-shape buckling. Fracture was also observed at the along the welding zone. The test was stopped due to testing apparatus limitation.

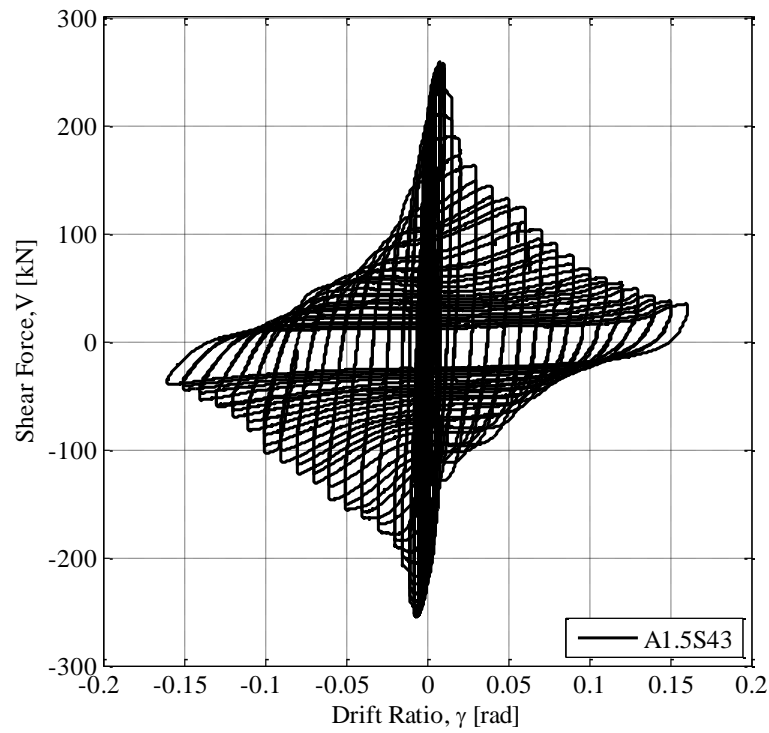


Figure 4.19 Force-drift relationship of A0.75S43

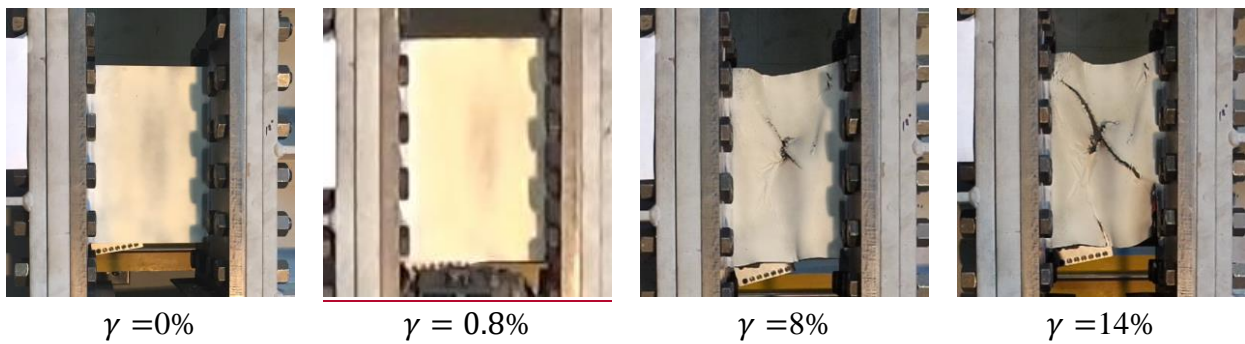


Figure 4.20 A1.5S43 at different drifts

4.4 Monotonic result

The monotonic results are briefly presented here. Nine specimens were tested with monotonic loading. Figure 4.21 shows the force-drift relationship of the monotonic loading. Force-drift result from monotonic loading is compared to cyclic result and shows that the monotonic does not represent the backbone of the hysteretic curve. This is due to cyclic hardening of WWFF and rapid degradation due to cyclic load. Therefore, the results of monotonic is not further discussed.

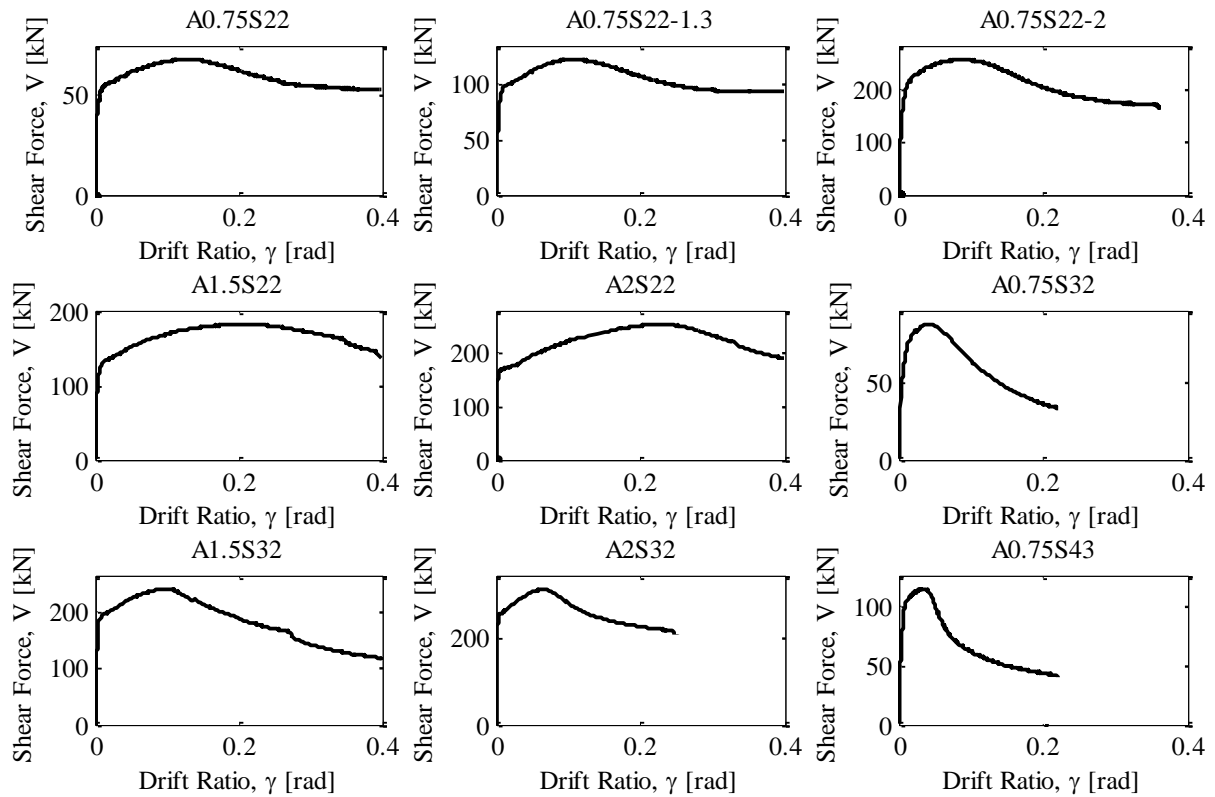


Figure 4.21 Force-drift relationship of monotonic loading

4.5 Discussion

4.5.1 Buckling shape and fracture location

Figure 4.22 shows the failure mode of the specimens at the corresponding drift ratio when significant yielding or buckling was observed. Two important observations were discovered. First, when the aspect ratio (A) is low (in the case $A = 0.75$), the yield lines were parallel to the loading. As the aspect ratio (A) increases to 1.5 and 2, the yield line starts to form in an angle, through tension field action and buckling of the web.

Secondly, the slenderness ratio showed influence of the failure of WWFF. In the lower slenderness ratio ($S = 22$) specimen, the web was more compact, this forced the WWFF to fail through fracture along the weld zone (left column of Figure 4.22). On the other hand, as the slenderness ratio increases, the web become more flexible, in this case the yield lines started to move towards the center of the web.

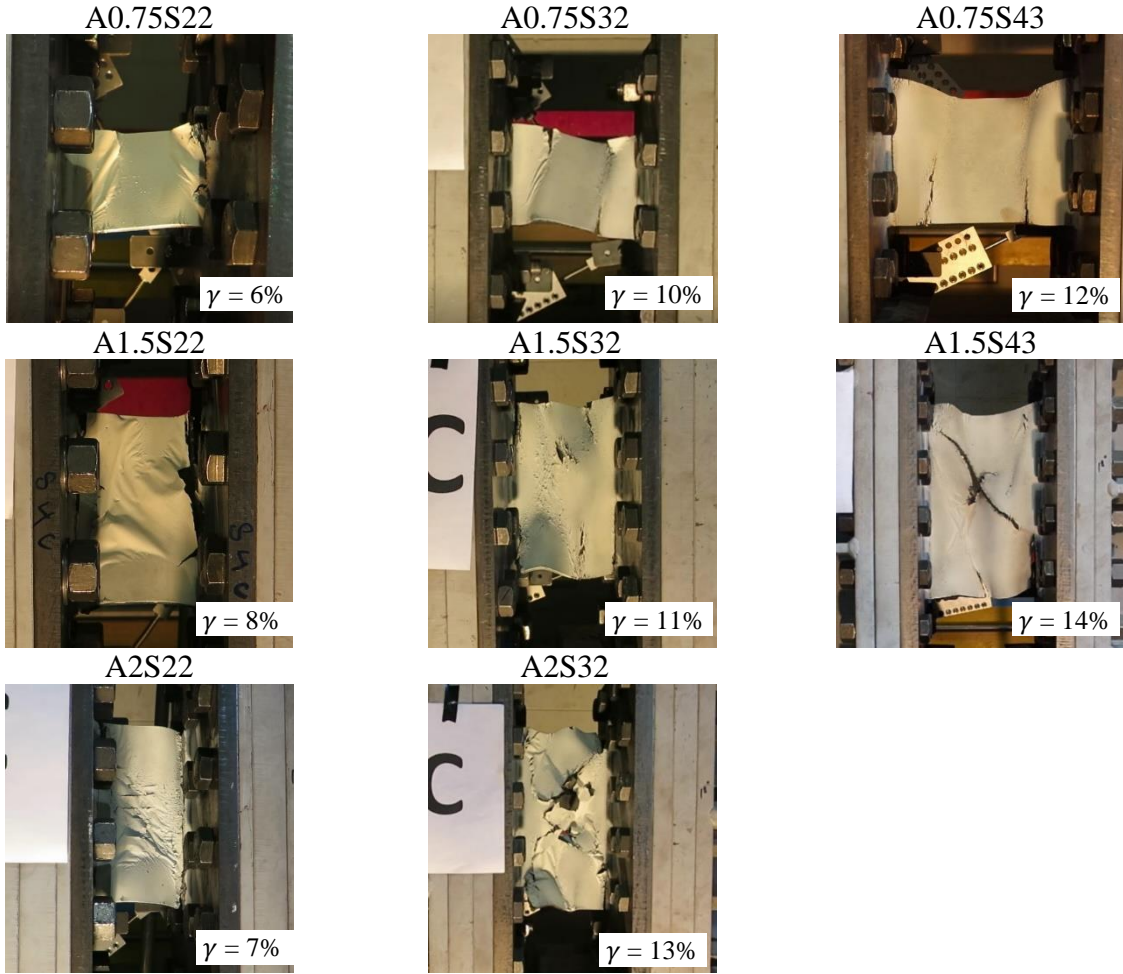


Figure 4.22 Failure mode of the different specimen

4.5.2 Force-drift relationship

The virtual displacement recorded was converted to drift ratio by dividing it with D' and plotted against force reading of the load cell. The force-drift relationships of the size ratio study are shown in Figure 4.23. Specimen A0.75S22-1.3 and A0.75SR22-2 were geometrically scaled based on A0.75S22. The overall shape of the hysteretic curves is similar with force increasing as the size ratio becomes larger.

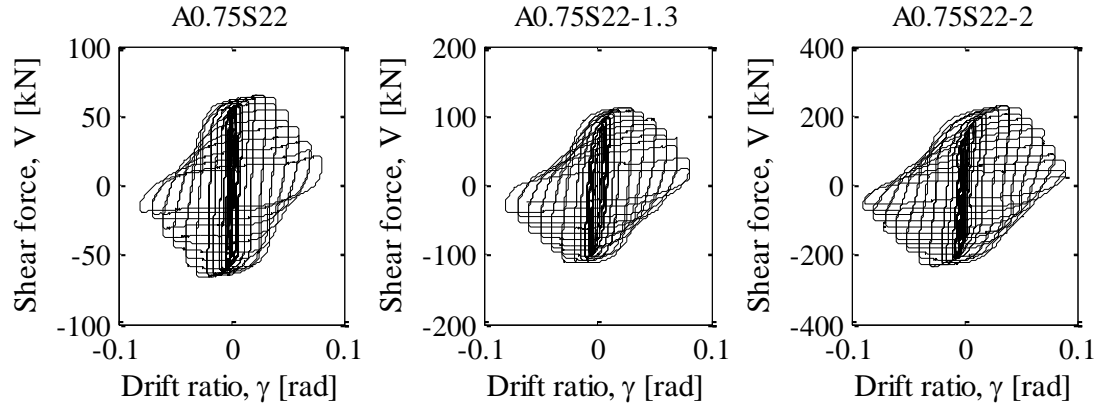


Figure 4.23 Force-drift relationship of size ratio study (A0.75S22, A0.75S22-1.3, A0.75S22-2)

Figure 4.24 shows the force-drift relationship of the specimens. The result shows that the WWFFs can produce very stable hysteresis curves. This means WWFF can be used as efficient damper to dissipate earthquake energy. At the low slenderness ratio, the hysteresis was very full. As the slenderness ratio (S) increases, the hysteretic curve becomes more pinching. On the other hand, the aspect ratio does not have significant impact to the shape of the hysteresis loops.

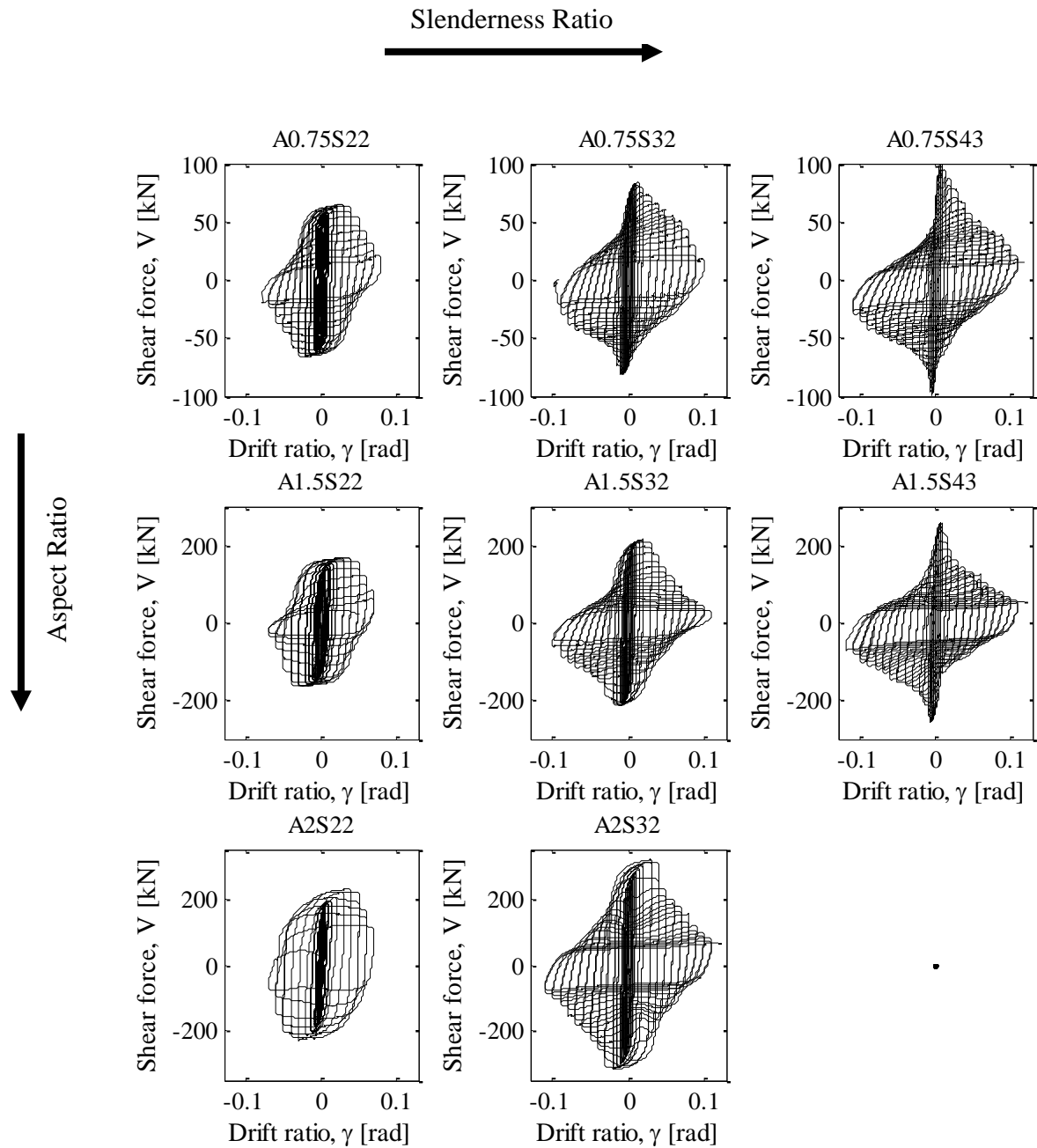


Figure 4.24 Cyclic force-drift relationship of aspect ratio and slenderness ratio study (all specimen except A0.75S22-1.3 and A0.75S22-2)

In addition to the hysteresis loops presented before, backbone curves for the specimens were generated from the envelope of the hysteretic curves. Figure 4.25 shows the backbone curves obtained from the hysteretic curves. The key parameters such as the yield force (V_y), yield drift ratio (γ_y), ultimate force (V_u), ultimate drift ratio (γ_u), over-strength factor ($\Omega_y = \text{ratio of } V_u \text{ to } V_y$) and the failure mode are summarized in Table 4.1.

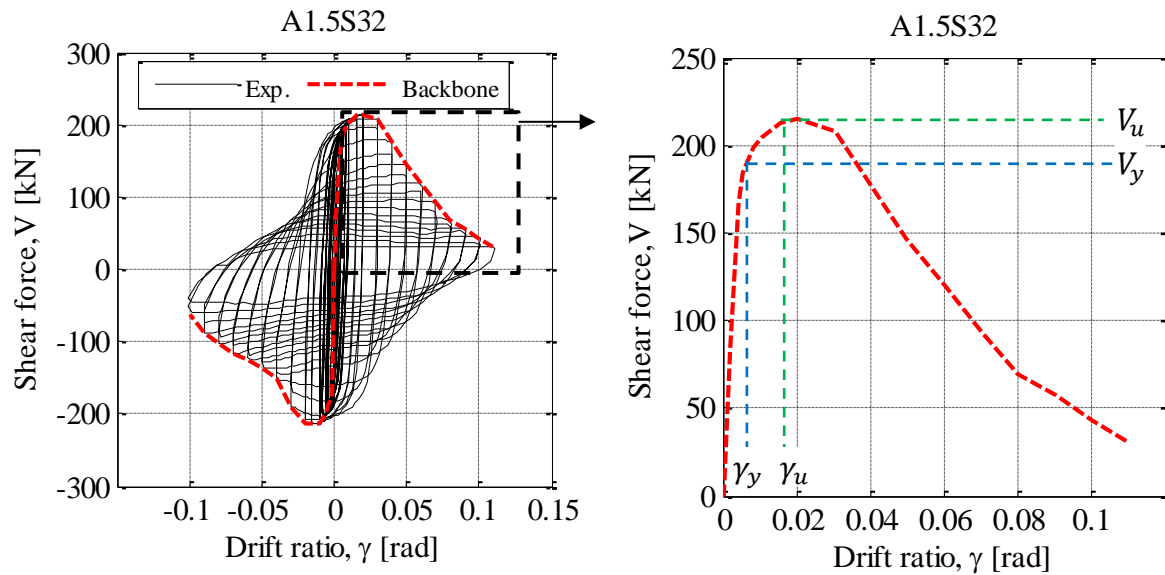


Figure 4.25 Sample backbone curve

Table 4.1 Summary of experiment results

Specimen	Yield force	Initial stiffness	Ultimate force	Over-strength factor	Yield drift ratio	Ultimate drift ratio	Buckling shape	Fracture location
	V_y	K	V_u	Ω_y	γ_y	γ_u		
	[kN]	[kN/rad]	[kN]	[-]	[%]	[%]		
A0.75S22	42	17822	65	1.57	0.23%	3.0%	horizontal	weld zone
A1.5S22	103	47349	166	1.62	0.22%	3.0%	diagonal	weld zone
A2SR22	140	69273	225	1.61	0.20%	4.0%	diagonal	weld zone
A0.75S32	62	24107	82	1.33	0.26%	1.0%	horizontal	buckling zone, weld zone
A1.5S32	144	57337	213	1.48	0.25%	2.0%	diagonal	weld zone
A2S32	221	95349	310	1.40	0.23%	3.0%	diagonal	welding zone, buckling zone
A0.75S43	79	30027	97	1.24	0.26%	0.5%	horizontal	buckling zone, weld zone
A1.5S43	210	81808	257	1.22	0.26%	0.8%	diagonal	buckling zone, weld zone

4.5.3 Size ratio effect

The size ratio factor (f_{SC}) of A0.75S22-1.3 and A0.75S22-2 to A0.75S22 was 1.3 and 2, respectively. The results on overall hysteretic was observed. A0.75S22 was the benchmark specimen in this study and hence the factor was one. The force was obtained from the experiment was scaled by the size ratio factor. Factored shear force (V_f) was defined using similitude law as:

$$V_f = \frac{V}{f_{SC}^2} \quad (21)$$

The factored hysteretic loops and the corresponding backbone curve of A0.75S22 and A0.75S22-2 agreed to each other (Figure 4.26). However, A0.75S22-1.3 showed lower factored force

compared to A0.75S22 and A0.75S22-1.3. Nevertheless, the overall behavior still shows acceptable agreement with the others. This means that the WWFF with the same aspect ratio and slenderness ratio can be geometrically scaled; and it will exhibit similar behavior.

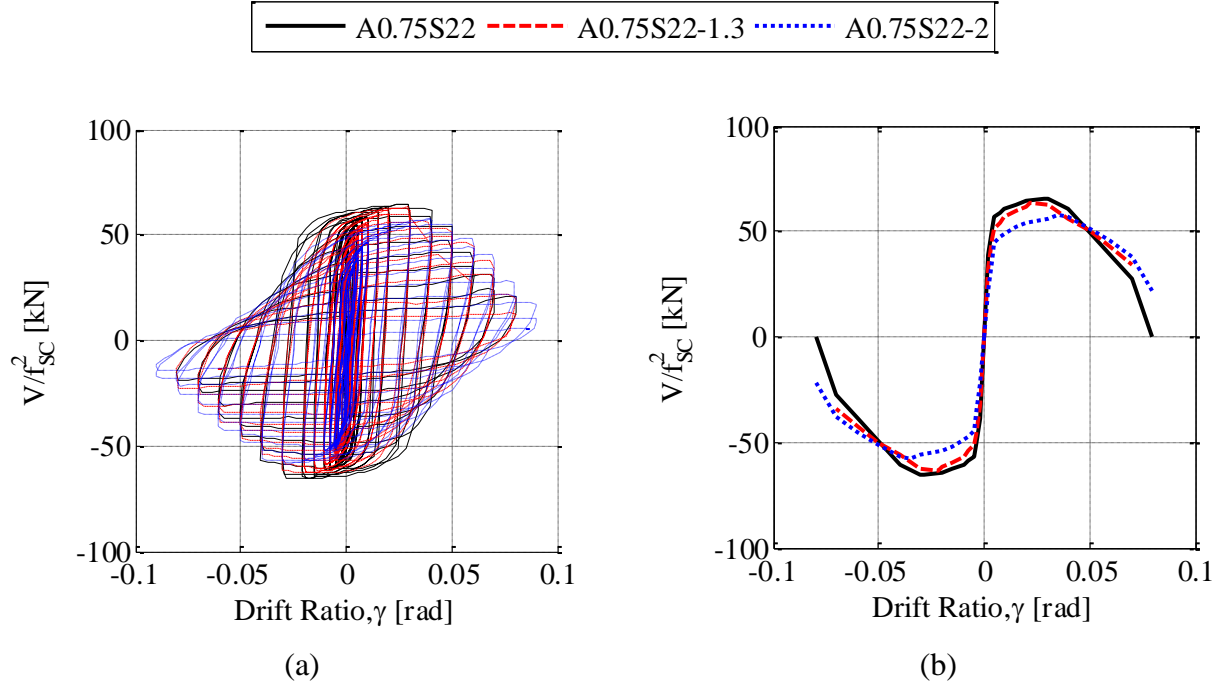


Figure 4.26 (a) Hysteresis curve; (b) Backbone curve; (c) Factored cumulative energy of A075SR22, A075SR22-1.3, A075SR22-2

4.5.4 Yield force and initial stiffness

Figure 4.27(a) and Figure 4.27 (b) show that the yielding force (V_y) and initial stiffness (K) are functions of aspect ratio (A). The result shows both the yielding force (V_y) and initial stiffness (K) increases linearly as the aspect ratio (A) increases. Similarly, as the slenderness ratio (S) increases, the yielding force (V_y) and initial stiffness (K) also increases.

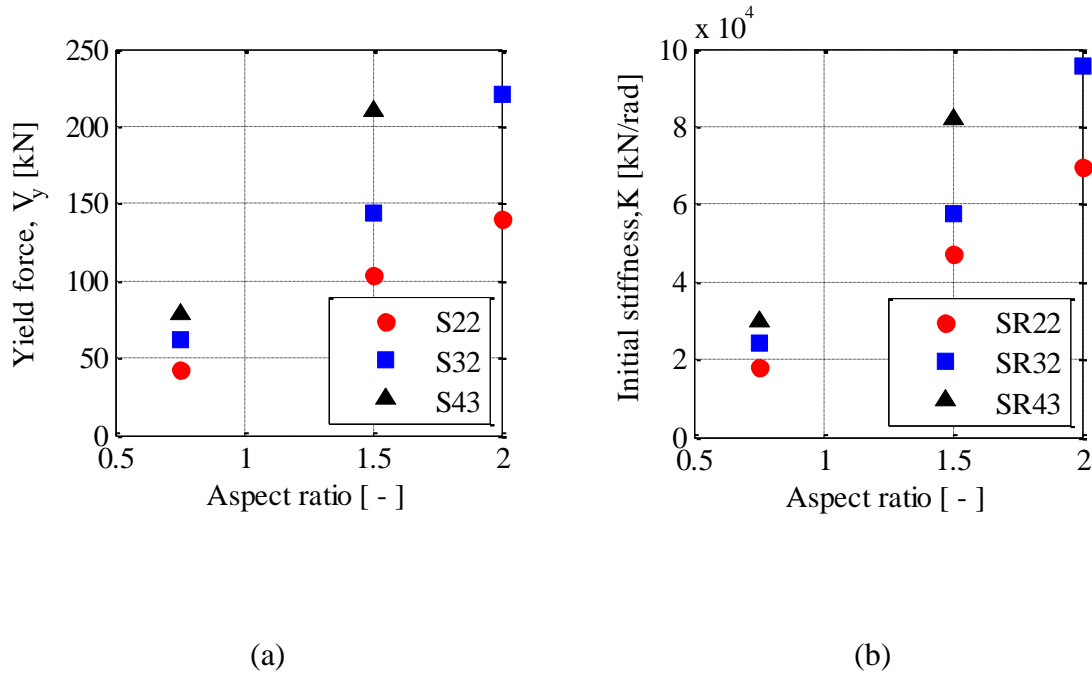


Figure 4.27 (a) Yield shear force and (b) initial stiffness for different aspect ratio

The yield force and initial stiffness above were normalized so that they are comparable among different slenderness ratio. The plot of normalized force, initial stiffness, and the proposed analytical equations are presented in Figure 4.28, and the summary is presented in Table 4.2.

. Figure 4.28a shows the effect of the aspect ratio on the yielding force of the WWFF. The shear force in Figure 4.28a was normalized using the pure shear force ($V_p = 1/\sqrt{3} \sigma_y a t_w$). The result shows the normalized yielding force (V_y/V_p) shows good agreement with the analytical equation shown in Eq. (11) with average difference of 5%. In general, as the aspect ratio increases the normalized yield force approaches V_p . In the low aspect ratio range, minor increase in the aspect

ratio results in high increase of the normalized yield force. Whereas, at the high aspect ratio, the increase in aspect ratio does not result in significant increase of normalized yield force.

Similarly, Figure 4.28b shows the normalized elastic stiffness for the WWFF at different aspect ratio. The elastic stiffness was normalized using the web thickness. The result shows the normalized elastic stiffness matched the theoretical equation shown in Eq. (17). very well with average difference of 8%. In general, the normalized elastic stiffness increases linearly as the aspect ratio increases.

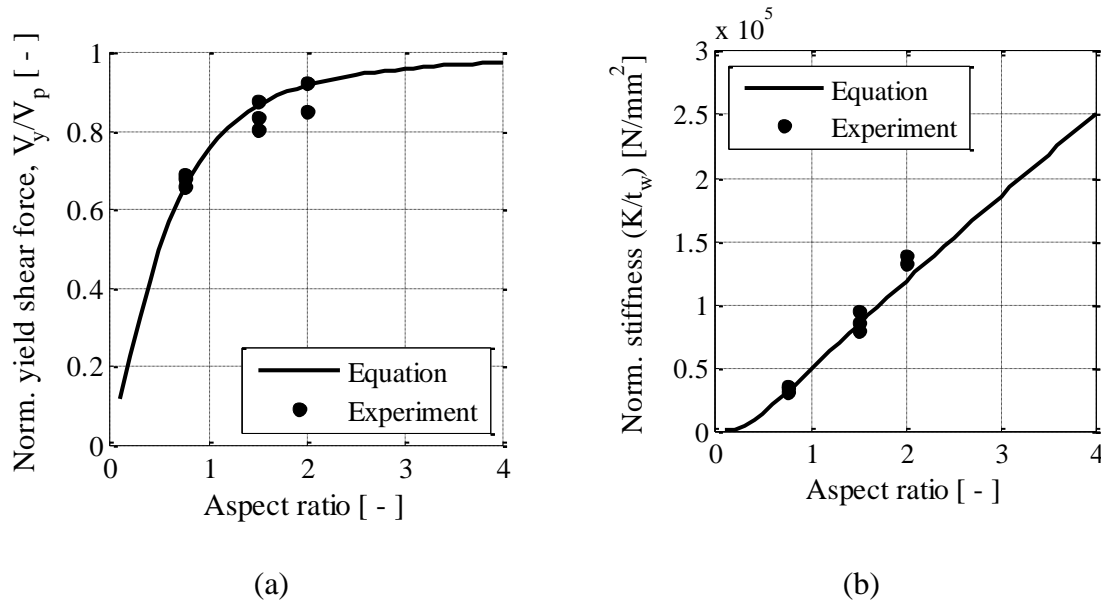


Figure 4.28 (a) Normalized yield shear force and (b) normalized stiffness for different aspect ratio

Table 4.2 Summary of yield force, initial stiffness, and prediction

Specimen	Yield force			Initial stiffness		
	V_y			K		
	Eq.	Exp.	% Diff.	Eq.	Exp.	% Diff.
	[kN]	[kN]	[%]	[kN/rad]	[kN/rad]	[%]
A0.75S22	39	42	7	15282	17822	14
A1.5S22	102	103	1	41997	47349	11
A2SR22	144	140	3	59227	69273	15
A0.75S32	56	62	9	22229	24107	8
A1.5S32	149	144	3	61087	57337	7
A2S32	210	221	5	86149	95349	10
A0.75S43	75	79	5	29638	30027	1
A1.5S43	198	210	6	81449	81808	6

4.5.5 Yield drift ratio and ultimate drift ratio

Yielding drift is the drift ratio corresponding to the yielding force, whereas the ultimate drift ratio is at ultimate force. The yielding drift ratio and ultimate drift ratio obtained from the backbone are presented in Figure 4.29a and Figure 4.29b respectively. The yielding drift ratio (γ_y) remains similar for all specimens, it ranged from 0.2% to 0.26%, with an average of 0.23%. Figure 4.29b shows the ultimate drift ratio (γ_u). The result shows as the slenderness ratio increases the ultimate drift ratio (γ_u) decreases. This means the stocky specimens reached the ultimate force at larger drift ratio. On the other hand, the slender specimens buckled earlier, hence showed lower ultimate drift ratio (γ_u).

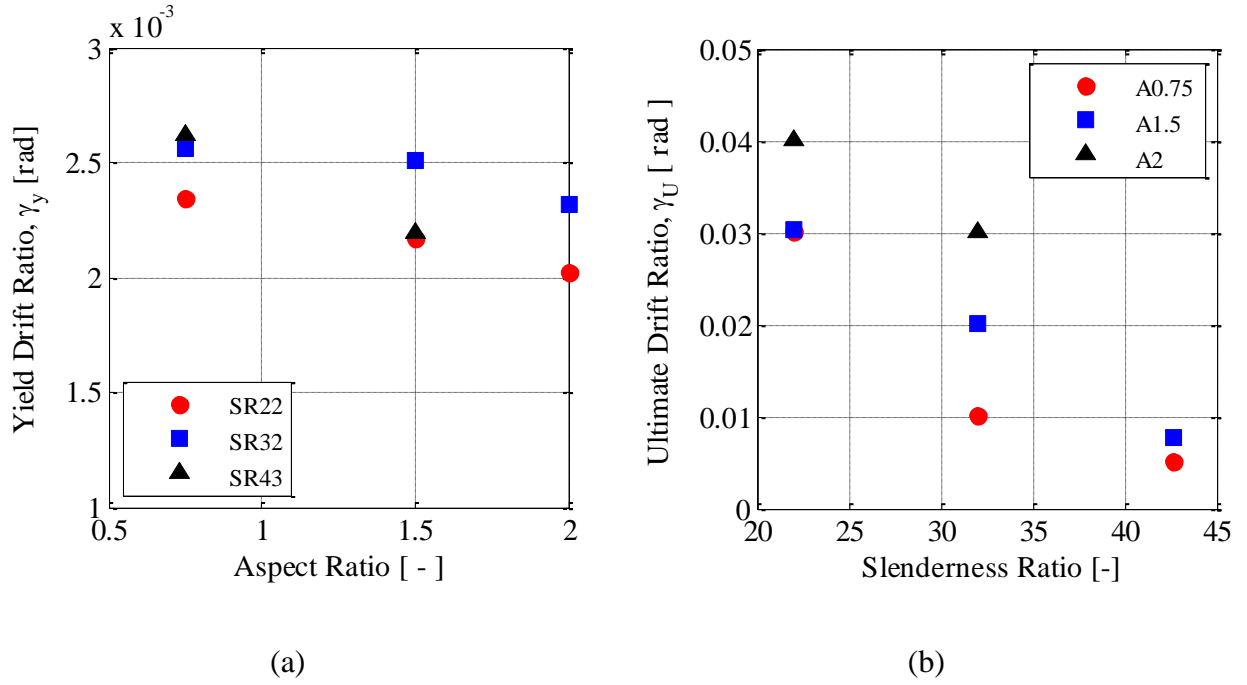


Figure 4.29 (a) Yielding drift ratio and (b) ultimate drift ratio

4.5.6 Degradation

After reaching the ultimate force, the shear force started to degrade due to buckling and fracture. Figure 4.30a and Figure 4.30b show the normalized backbone curves for the specimens with $A = 0.75$ and $A = 1.5$, respectively. In these figures, the forces were normalized using the expected plastic shear force $V_p = 1/\sqrt{3} \sigma_y a t_w$, where σ_y is the expected yield stress of the plate which is selected as 285 MPa. The result shows as the slenderness ratio (S) reduces, the ultimate force (V_u) increases, but the backbone curve will degrade more rapidly with lower ultimate drift ratio (γ_u).

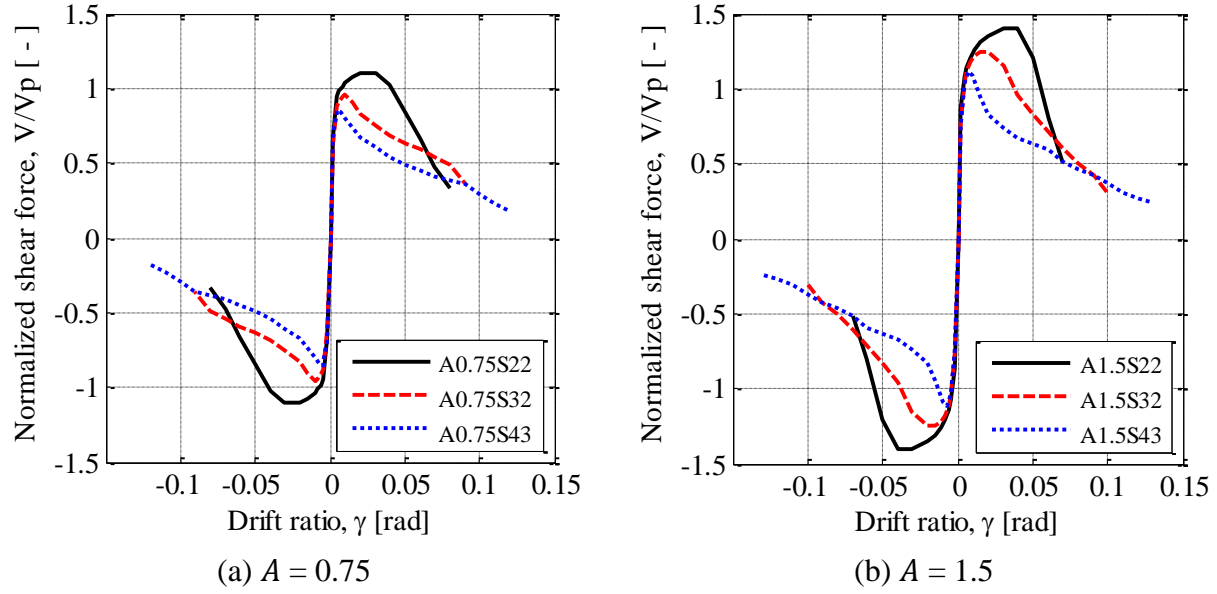


Figure 4.30 Backbone of normalized force plot of aspect ratio 0.75 and 1.5

4.5.7 Energy dissipation

Two sets of three specimen with S value of 22, 32, and 43 were studied. The first set had aspect ratio of 0.75 whereas the second one was 1.5. The cumulative energy dissipated normalized using the volume of web steel were plotted in Figure 4.31a and Figure 4.31b for the specimen with aspect ratio of 0.75 and 1.5, respectively.

The result shows as the slenderness ratio increases, the slope of the normalized cumulative energy dissipation decreases. It can be observed that the specimen with the same aspect ratio started dissipating the same cumulative energy in the beginning, then start to diverge as the higher slenderness ratio started to buckle. Although the lower slenderness ratio tends to be more desirable due to more stable hysteretic behavior, it shows lower ductility compared to higher slenderness ratio.

In general, the total normalized cumulative energy dissipation at the end of the experiment was similar for the specimen with the same aspect ratio. The specimen with the aspect ratio of 0.75 had a total normalized cumulative energy about 0.28 kN-mm/mm³, while the specimen with the aspect ratio of 1.5 has a total normalized cumulative energy about 0.38 kN-mm/mm³.

If the total energy to be dissipated by the WWFF is a constant, the specimen with higher slenderness ratio needs to go through higher cumulative drift ratio. This might not be desirable for building.

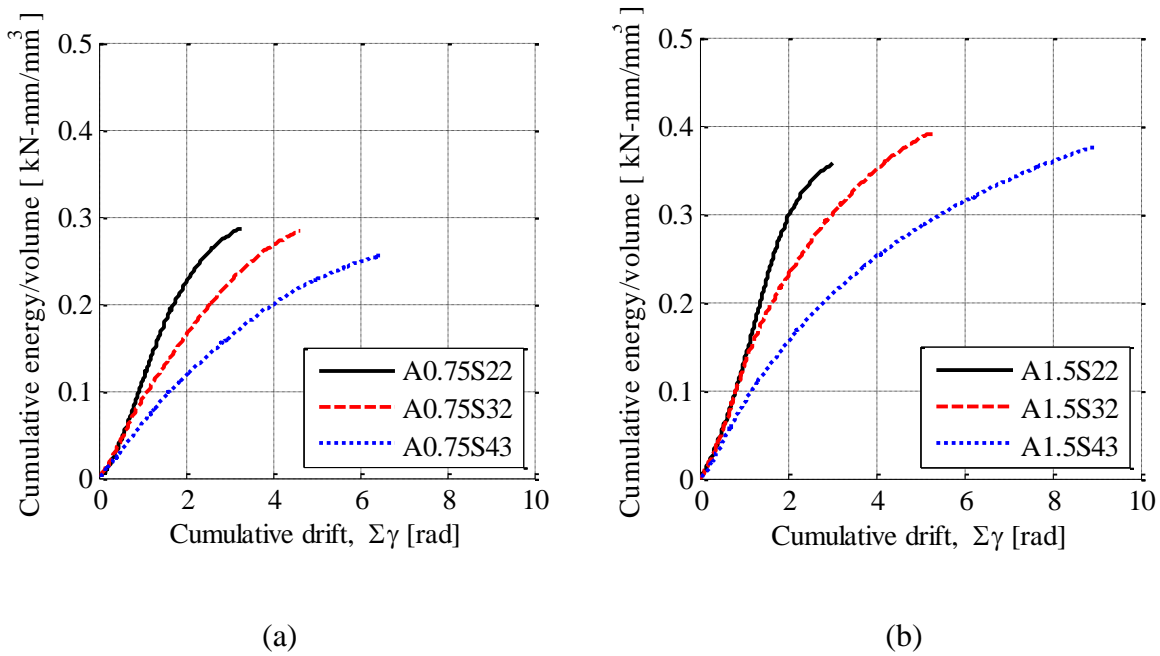


Figure 4.31 Normalized energy plot of aspect ratio 0.75 and 1.5

4.5.8 Over-strength factor

Over-strength factor, calculated as ratio of ultimate force to yielding force, is plotted in Figure 4.32. From this figure, one can observe that the over-strength varies with the changes in slenderness ratio. As the slenderness ratio decreases, the over-strength becomes lower.

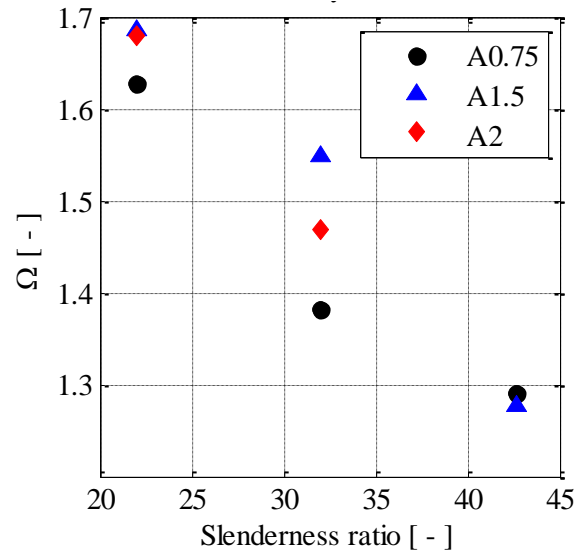


Figure 4.32 Over-strength factor

Chapter 5: Numerical Model

5.1 Introduction

This chapter describes the numerical model of the Welded Wide Flange Fuse using finite element program ABAQUS/CAE. A graphical user interface program ABAQUS/CAE in conjunction with *Python* programming language was used to build the finite element model. In this chapter the general model description, approaches, and assumptions in material modeling, mesh algorithm, element definition, initial imperfection, and the boundary condition are discussed.

5.2 Model description

Only the web part of the specimen was modelled in ABAQUS as a shell element. The boundary condition is assigned at top and the bottom part of the flanges. The depth modelled is the clear depth between the weld lines.

Geometric modelling was done in *Sketch* according to the specimen size. Section's type used is shell/continuum shell, homogenous. Two type of material stress-strain relationships were used for monotonic and cyclic loading. In the *Assembly Module* the web is taken as the instance with independent type. Mesh was defined as a percentage of the web depth. The convergence study of the mesh is presented in 5.2.4.

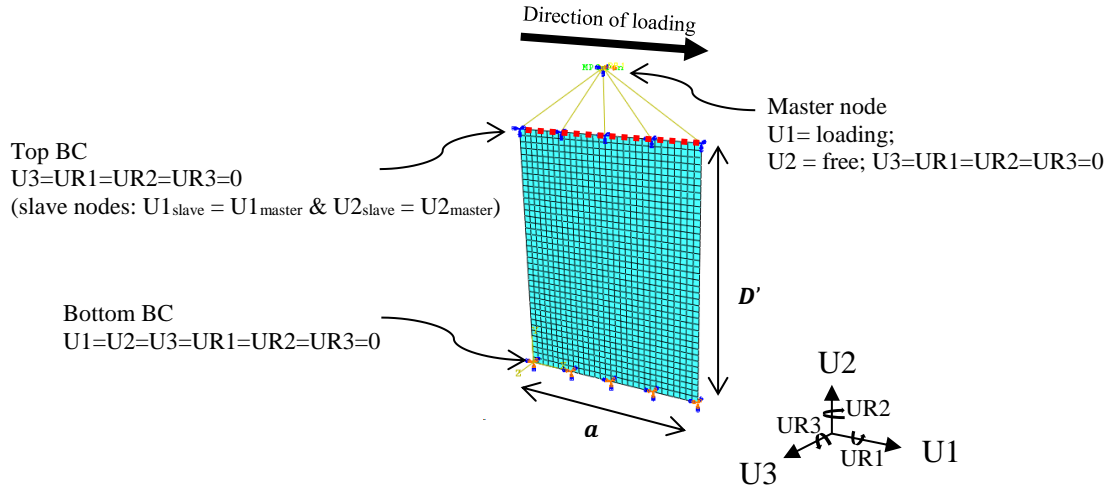


Figure 5.1 Specimen model in ABAQUS/CAE

5.2.1 Material modelling

In ABAQUS/CAE finite element software, true stress and true strain material data is used. The true stress is the stress experienced by the instantaneous cross-sectional area caused by the instantaneous load acting. True strain is the change of instantaneous gauge length of the specimen. The material stress strain relationship obtained from the coupon test is an engineering stress-strain relationship. This data is converted to true stress and true stress using Eq. (22) and (23).

The relationship between true stress and engineering stress is defined as:

$$\sigma_T = \sigma(1 + \epsilon) \quad (22)$$

Whereas the engineering strain is converted to true strain with following equation:

$$\epsilon_T = \ln(1 + \epsilon) \quad (23)$$

The A36 steel was used as the material of specimen. A36 is a commonly available steel grade for steel plate. Steel A36 has a yield strength of 36 ksi and ultimate strength 58-80 ksi. Young's modulus is taken as 29,000 ksi.

In this study, the *Combined* material model from *plastic* material in ABAQUS/CAE [18] was used to model the kinematic and isotropic hardening of the A36 steel material. Fracture was not explicitly modelled.

5.2.2 Element type

Shell element was used because the web has typical geometric property where one dimension, which is the thickness, is significantly smaller than the other geometry properties.

Element type used to model the web was S4R element, which was a four-node shell elements with reduced integration. This shell element is a conventional type of shell elements.

This element has three translational and three rotational DOFs at each node. S4R is a general-purpose shells element that uses thick shell theory if the thickness increases and uses discrete Kirchhoff thin shell theory for small thickness. S4R element considers the finite membrane strains and large rotations. This type of element fits large-strain analysis. It has one integration location which makes it computationally efficient.

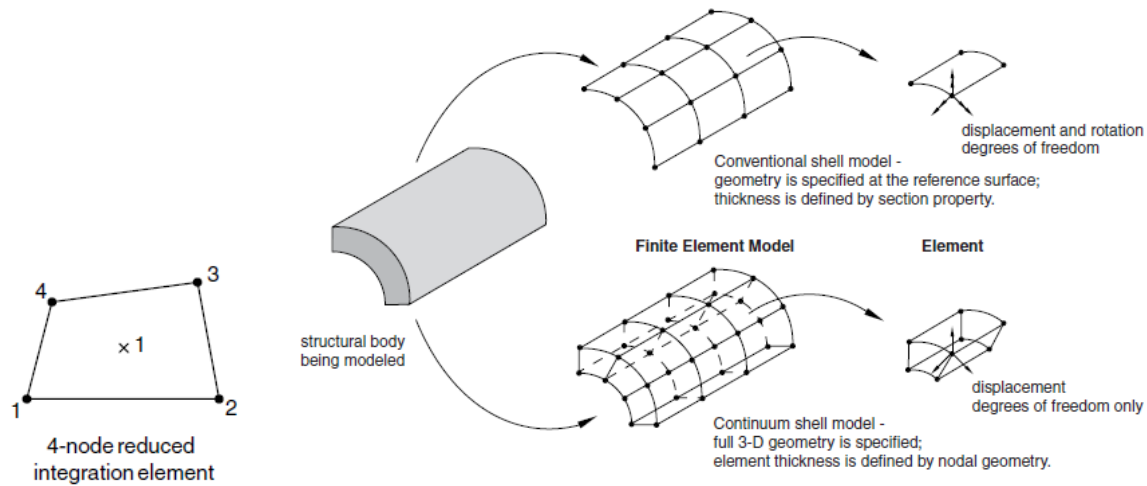


Figure 5.2 S4R shell element (ABAQUS manual)

S4R also allows transverse shear deformation. The transverse shear is assumed to be constant over the thickness. A homogenous shell section was defined as the section with thickness as specified on specimen geometry properties. The Simpson's integration rule through the thickness was used with nine integration points.

5.2.3 Imperfections

It is known that any structure inherits imperfection. This imperfection should be applied in finite element model to achieve realistic buckling forces and shapes.

To account for the geometric imperfection of specimen, initial imperfection is assigned in the finite element modeling. There are three ways to model imperfection in ABAQUS: (1) linear superposition of the buckling eigen modes, (2) displacement obtained from static analysis, (3)

manual input of imperfection values on specific nodes. In this research the initial imperfection is obtained from buckling eigen analysis.

The initial imperfection applied to the FE model used the buckling eigen modes. In order to get the eigen values for buckling, the undeformed models are analyzed first. The undeformed model was subjected to one-unit load in the direction of U1 (direction of the intended loading).

In this study, the imperfection was modeled using a combination of first three buckling modes. The imperfection amplitude for each mode was selected equals to 0%, 0.25%, 0.3%, 0.95% of clear depth (D'). Figure 5.3 shows the deformed shape of the buckling modes for the WWFF with different aspect ratio. Specimen with 0.75 aspect ratio shows that the deformation U3 of first and second mode are concentrated at the free edge. Whereas the larger aspect ratio (1.5 and 2) shows U3 deformation in the middle of the web as well. This shows that the buckling mode of specimen with $A=0.75$ is not tension field dominant. On contrary, specimen with $A=1.5$ and $A=2$ tends to form the diagonal tension field.

Figure 5.4 shows that backbone curves for specimen A1.5S32 obtained from the experimental test plotted against different imperfection amplitude models. Without imperfection (0% D' amplitude), the backbone curve shows no degradation. As the imperfection amplitude increases, the degradation starts earlier (at smaller drift ratio) and the degradation is more severe. The result shows the imperfection amplitude equals 0.3% D' imperfection provides the best match to the experimental result. Hence, 0.3% D' was selected as the imperfection amplitude for the finite element model.

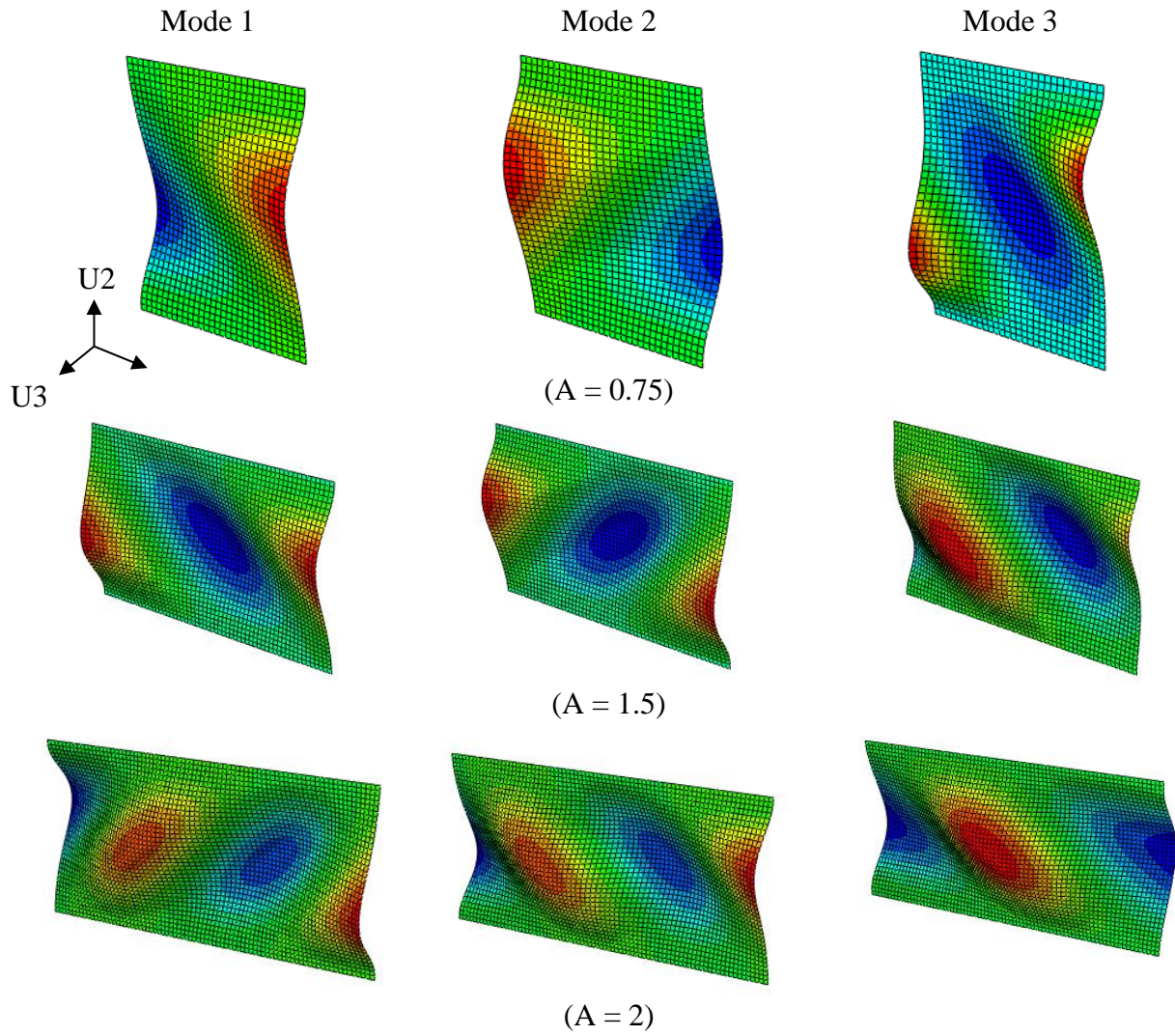


Figure 5.3 Mode shape of buckling analysis of $A=0.75$, $A=1.5$, and $A=2$

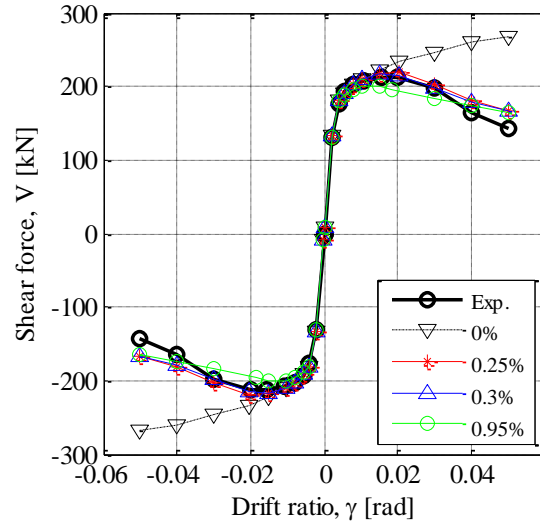


Figure 5.4 A1.5S32 Backbone for different imperfection amplitude (0%, 0.25%, 0.3%, and 0.95% of D')

5.2.4 Mesh

Meshing is very important in finite element modelling. Different mesh can affect the analysis result. Too coarse mesh will result in inaccuracy of the analysis, whereas too fine mesh is computationally ineffective. Therefore, it is very important to conduct mesh convergence analysis to determine what the proper mesh size for this analysis.

In this study, the influence of the mesh sizes equals to 10%, 6%, 4%, 2% and 1% of the clear web depth (D') was examined. Figure 5.5 shows the backbone curves of the finite element model with different mesh sizes for the A1.5S32 specimen (Table 1). The result shows as the mesh size reduces the curve starts to degrade after the WWFF passes the peak force. As the mesh size reduces to 2% of the clear web depth (D'), the backbone curve matches converge to the 1% clear

web depth (D'). Hence, the mesh size of 2% of the clear web depth (D') was selected in this study.

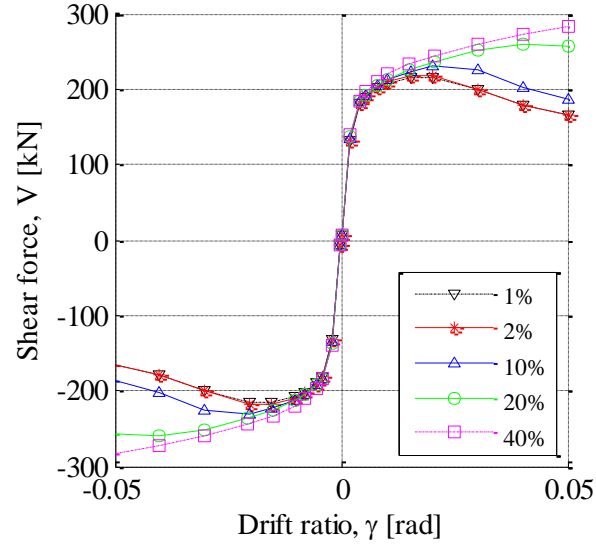


Figure 5.5 A1.5S32 backbone for different mesh size (1%, 2%, 10%,20%, and 40% of t_w)

5.2.5 Boundary condition

The boundary condition was modelled on top and bottom part of the web. The bottom part represents the connection to the mounting. The top boundary condition represents the connection to the loading beam (L-beam). Therefore, the loading protocol is assigned at the top boundary condition as displacement control loading in U1 direction (horizontal).

The top part of the web was constrained using *Beam Multi Point Constraints(MPC)*. The MPC was used to simulate the rigid beam movement of the loading beam. The loading beam was expected to move in U1 direction without significant rotation. *Pin MPC* constrains all degree of

freedom of one master point or one set of master points to a set of slave points. In this model, single master point is used as a reference point with all degree of freedom restrained. In addition, the rotational DOFs of the master and slave nodes were restrained. Displacement loading history was applied at the master node. The bottom part of the web is restrained with all degree of freedom restrained to simulate the rigid connection between the web and the flange.

5.3 Finite element model validation

The developed finite element model in ABAQUS then needed to be validated with the experimental result.

5.3.1 Force-drift relationship

The calibrated finite element model was used to simulate the force-drift response of the WWFFs tested in the experiment phase. Figure 5.6 shows the comparison of the force-drift responses between the experimental test and the finite element simulation. The result shows that the simple modeling approach presented in this study can model the force-drift response of the WWFF well.

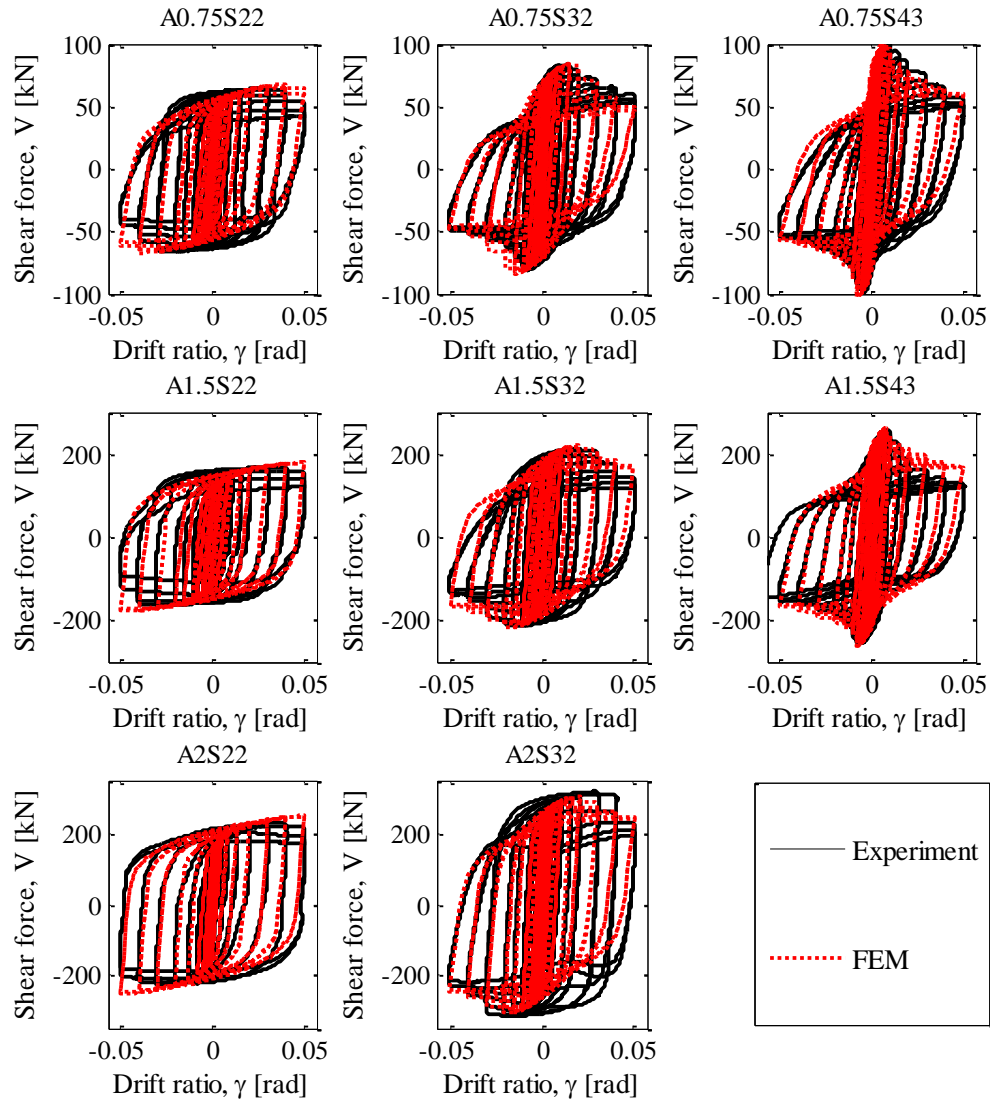


Figure 5.6 Comparison between experimental and FE model for cyclic loading

5.3.2 Buckling shape

In addition to the force-drift response comparison, Figure 5.7 shows comparison of the buckling shape observed from the analytical simulation and experimental testing. The specimen with

aspect ratio of 0.75 shows out-of-plane buckling at the free edges. As the aspect ratio increases, diagonal tension field starts to form in the web. The buckling zone occurs at the edge and middle part of the web. The result shows the finite element model can simulate the overall buckling response of the WWFF well.

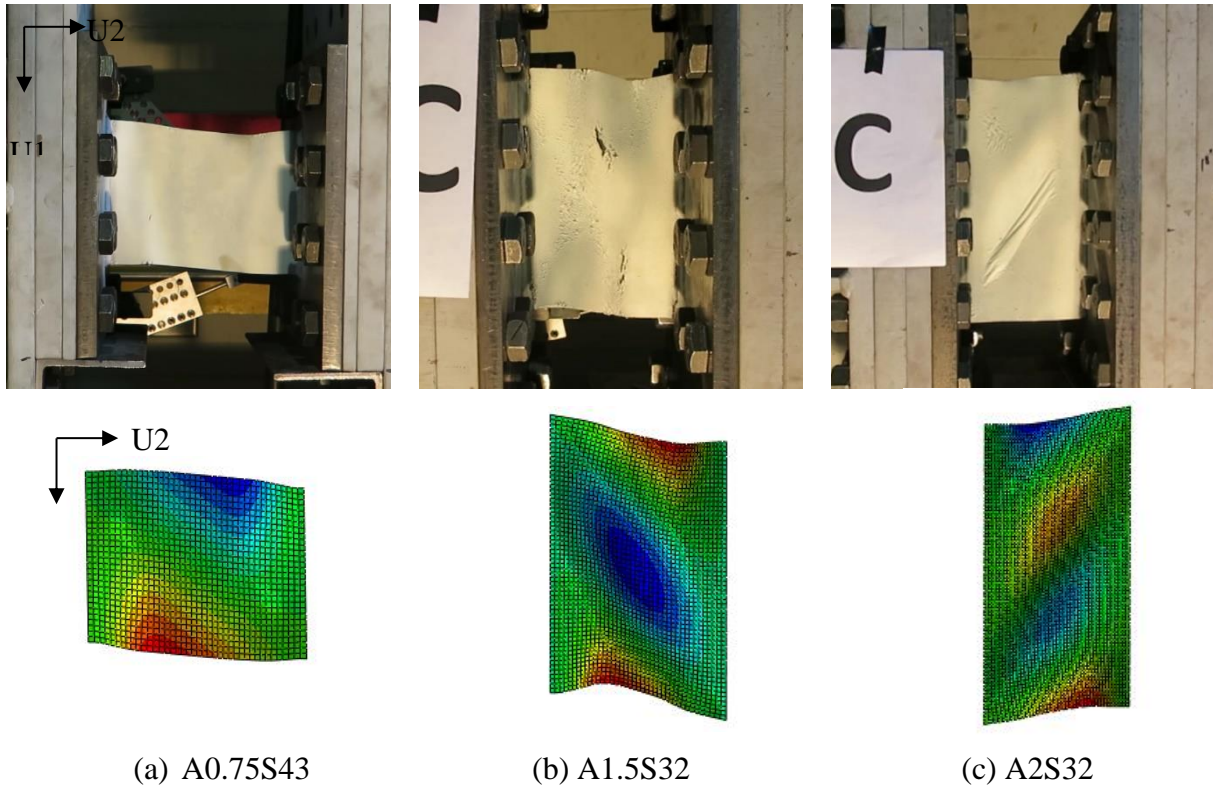


Figure 5.7 Buckling shape of experiment and corresponding U3 deformation of FEM

Chapter 6: Parametric Study

6.1 Introduction

A finite element model of the web part of WWFF using ABAQUS/CAE was developed and validated in previous chapter. Based on validated model, a parametric study was performed. The objective of this study is to identify key parameters that affect the behavior of WWFF. In this study, numbers of FE model with various aspect ratio and slenderness ratio were built in ABAQUS/CAE. The results were used to complete the trend for each parameter or to provide better understanding of WWFF behavior.

6.2 Finite element model matrix

After the developed finite element models have been validated, detailed parameter study was carried out to examine the nonlinear behavior of the WWFF with different geometry parameters. Twenty-four WWFFs with different aspect ratios and slenderness ratios were included in this study. This includes 6 models with slenderness ratio of 32 and aspect ratios from 0.5 to 3. In addition, 18 models with slenderness ratios from 18 to 43 with aspect ratios of 1 to 2.5. This aspect ratio and slenderness ratio were selected to provide data points beside the experiment. Table 2 shows the summary of the specimen parameters included in the parameter study.

Table 6.1 FEM analysis matrix

Aspect ratio study			Slenderness ratio study								
Model name	S	A	Model name	S	A	Model name	S	A	Model name	S	A
	$\frac{D'}{t_w}$	$\frac{a}{D'}$		$\frac{D'}{t_w}$	$\frac{a}{D'}$		$\frac{D'}{t_w}$	$\frac{a}{D'}$		$\frac{D'}{t_w}$	$\frac{a}{D'}$
	[-]	[-]		[-]	[-]		[-]	[-]		[-]	[-]
FA1	32	0.5	FS1	18	1	FS7	18	1.5	FS13	18	2.5
FA2	32	1	FS2	23	1	FS8	23	1.5	FS14	23	2.5
FA3	32	1.25	FS3	28	1	FS9	28	1.5	FS15	28	2.5
FA4	32	1.75	FS4	33	1	FS10	33	1.5	FS16	33	2.5
FA5	32	2.5	FS5	38	1	FS11	38	1.5	FS17	38	2.5
FA6	32	3	FS6	43	1	FS12	43	1.5	FS18	43	2.5

6.3 Yielding force and initial stiffness

Figure 6.1a shows the normalized yield force of WWFF with different aspect ratios. These results were plotted against analytical equations proposed in Chapter 2. Overall, the normalized yield shear force (experiment and finite element model) increases but with decreasing rate as the aspect ratio increases. This trend is similar with the equation proposed. Similarly, the initial stiffness of the WWFF obtained from the finite element simulation, experimental testing and stiffness equation proposed are summarized in Figure 6.1b. The normalized stiffness of the experiment and finite element model is linearly varied and follows the equation proposed.

The result shows excellent match of the initial stiffness between the finite element simulation, experimental test and proposed equation. This shows the behavior of the WWFF can be consistently predicted, hence it can be reliably used in engineering applications.

The summary of the normalized yield force and normalized initial stiffness value from the proposed equation, experiment, and finite element model are presented in Table 6.2. The yielding force and initial stiffness predicted using Eq. (11) and Eq. (17) were also compared with the experiment and finite element model. The result shows the Eq. (11) and Eq. (17) can be used reliably to predict the yielding force and initial stiffness of WWFF well.

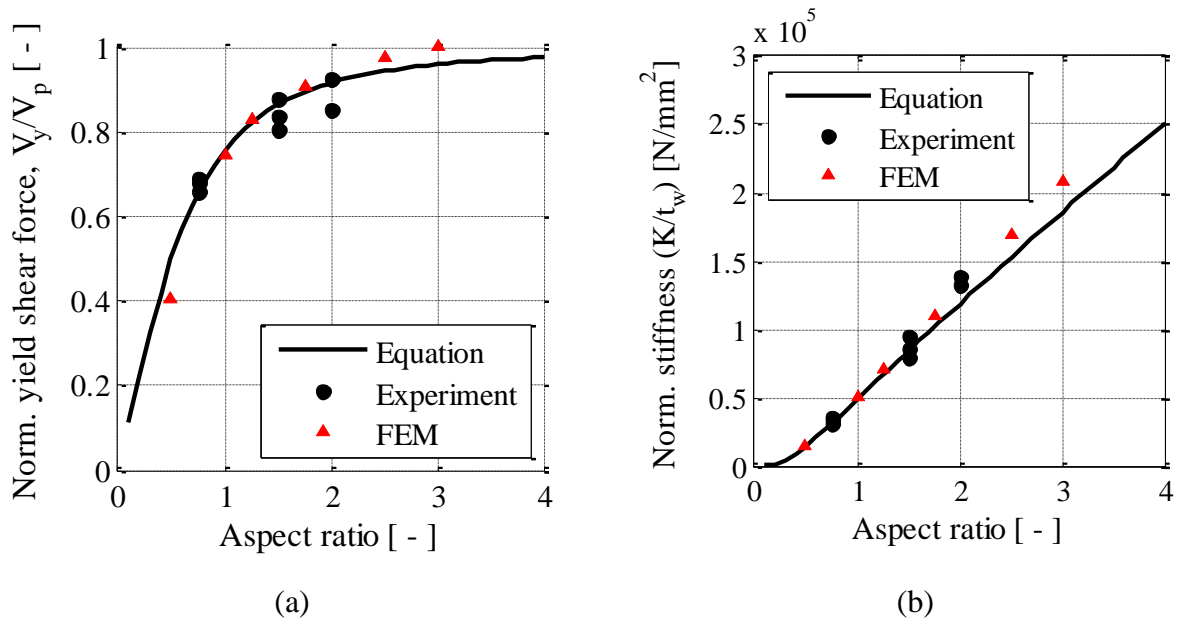


Figure 6.1 Normalized yield shear force and stiffness for different aspect ratio

Table 6.2 Normalized yield force and normalized initial stiffness of equation, experiment, and finite element

Specimen	Norm. yield force			Initial stiffness		
	V_y			K/t_w		
	Eq.	Exp.	% Diff.	Eq.	Exp.	% Diff.
	[-]	[-]	[%]	[kN/mm ²]	[kN/mm ²]	[%]
A0.75S22	0.65	0.68	3	31	36	14
A1.5S22	0.87	0.83	4	84	95	11
A2SR22	0.92	0.85	8	119	139	15
A0.75S32	0.65	0.69	5	31	33	8
A1.5S32	0.87	0.80	8	84	79	7
A2S32	0.92	0.93	1	119	131	10
A0.75S43	0.65	0.66	0	31	31	1
A1.5S43	0.87	0.88	1	84	85	0
FA1	0.50	0.45	12	14	14	3
FA2	0.76	0.82	7	49	51	5
FA3	0.82	0.89	7	66	71	6
FA4	0.90	0.96	7	102	110	8
FA5	0.94	1.03	9	152	169	10
A6	0.96	1.06	10	186	208	11

6.4 Over-strength ratio

Figure 6.2 shows the over-strength ratio (calculated using the maximum force divided by the yielding force) obtained from the finite element modelling and experimental testing. Overall, the finite element model and the experimental result matches well. The result shows as the over-strength ratio decreases linearly as the slenderness ratio increases. This is because the specimens with higher slenderness ratio buckles earlier and have lower over-strength ratio. Specimen with slenderness ratio lower than 30 have over-strength ratio greater than 1.5, this might not be as

desirable as the connections and the main structural components will need to be capacity designed to ensure the yielding will only occur in the WWFF.

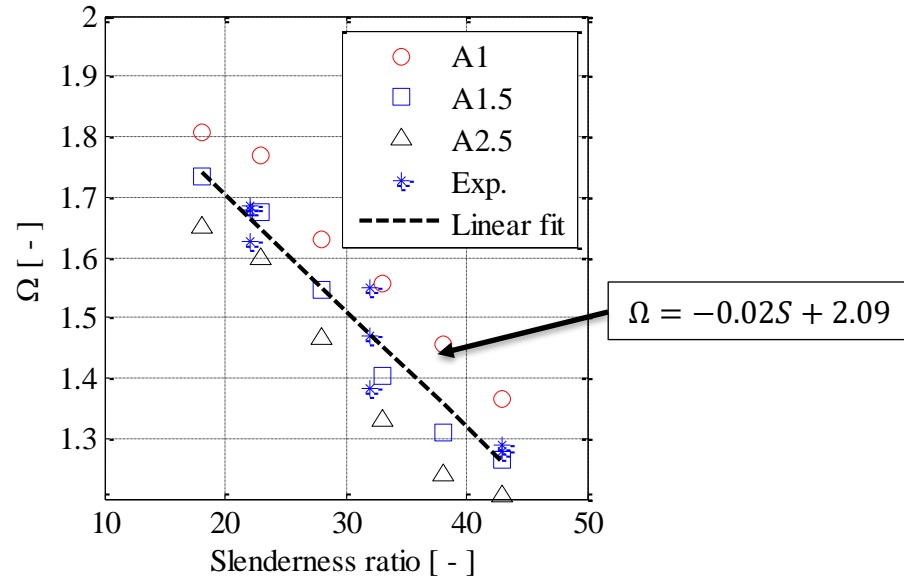


Figure 6.2 Over-strength ratio for different slenderness ratio

6.5 Ultimate drift ratio

In addition to the over-strength ratio, Figure 6.3 shows the comparison of the ultimate drift ratios (the drift at maximum force) vs. the slenderness ratios from the finite element model and experiment. The result shows the ultimate drift ratio decreases as the slenderness ratio increases. Specimens with higher slenderness ratio tends to buckle earlier and therefore have lower ultimate drift ratio.

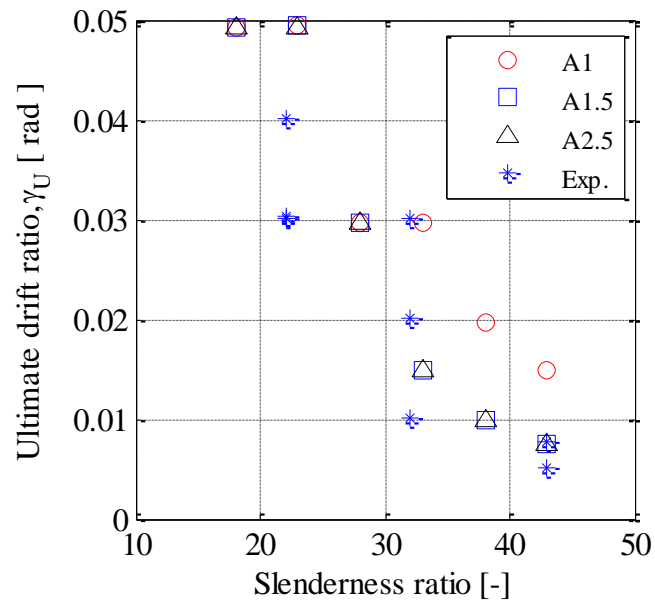


Figure 6.3 Ultimate drift ratio of parametric study

Chapter 7: Summary, Conclusion, and Recommendation

7.1 Summary and conclusion

Experimental and analytical studies were conducted to investigate the behavior of Welded Wide Flange Fuse. The experiment was performed on 19 specimens with two different loading protocols (monotonic and cyclic). The cyclic results are used in deeper study of the behavior of WWFF. Finite element model was developed using ABAQUS/CAE and validated by the experimental result. Parametric studies on aspect ratio and slenderness ratio of WWFF then conducted using the validated mode. Two design equations to predict yielding force and initial stiffness are proposed here. These two equations are also validated by the experimental and finite element models.

The Welded Wide Flange Fuse (WWFF) is proposed as an alternative structural fuse for seismic application. Detailed experimental and numerical studies were conducted on the WWFF and the results are summarized as follow:

1. WWFF exhibits stable hysteresis, which indicates that WWFF is an efficient energy dissipation device.
2. The behavior of the WWFF is highly influenced by the aspect and slenderness ratio.
3. As the aspect ratio increases, the buckling shape changes from two parallel lines in the loading direction to diagonal buckling shape. However, the hysteretic shape does not significantly change with aspect ratio.

4. WWFF with low slenderness ratio shows a failure mode with pure shear yielding and fracture near the welding zone. As the slenderness ratio increases, plate buckling and yielding through tension field action occurs, moving the fracture to the center of the web.
5. Slender specimens reached the ultimate force at a lower drift ratio, but degrades more gently after the force passed the ultimate force.
6. WWFF shows relatively similar total energy absorption per volume for same aspect ratio. As the aspect ratio increases, the total energy absorption per volume increases.
7. At the same aspect ratio and cumulative drift ratio, the specimen with lower slenderness ratio has higher total energy absorption per volume.
8. The simple finite element model can be used to model the force-deformation response of the WWFF.
9. As the mesh sizes decreases, the model is able to simulate the degradation response of the WWFF. A mesh size of $2\%D'$ is a good mesh size to model the WWFF.
10. The result of the finite element model is sensitive to imperfection. Imperfection amplitude of $10\%D'$ shows good agreement with the experiment result.
11. The yield force and initial stiffness can be reliably predicted by the simple analytical equations presented.
12. Over-strength factor of WWFF varies with the slenderness ratio. As the slenderness ratio increases, the over-strength factor decreases.

7.2 Recommendation for future study

The results of this study show that WWFF is a reliable and predictable damper. Further study on its behavior and its application should be conducted. Recommendations for future study are as follow:

1. The finite element model in this research does not include fracture model. Therefore, development in more advance modelling that includes fracture of WWFF is recommended to provide better understanding of WWFF ductility.
2. This study only covers component level study of WWFF. Detailed study on the application of WWFF in system level is required so that the complete picture of WWFF as robust damper is achieved.
3. Different hole patterns can be introduced to the web. The behavior of WWFF changes due to the present of hole patterns on its web and should be further studied. By introducing hole patterns, WWFF is even more versatile to meet different demands of structure.

Bibliography

- [1] American Institute of Steel Construction (2016), “Seismic Provisions for Structural Steel Buildings,” American Institute of Steel Construction, Chicago.
- [2] Brando, G., D’Agostino, F., and De Matteis, G. (2013), “Experimental tests of a new hysteretic damper made of buckling inhibited shear panels,” *Mater. Struct.*, Vol (46), no. 12, pp. 2121–2133.
- [3] Chan, R. W. K. and Albermani, F. (2008), “Experimental study of steel slit damper for passive energy dissipation,” *Eng. Struct.*, Vol (30), no. 4, pp. 1058–1066.
- [4] Chan, R. W. K., Albermani, F., and Kitipornchai, S. (2013), “Experimental study of perforated yielding shear panel device for passive energy dissipation,” *J. Constr. Steel Res.*, Vol (91), pp. 14–25.
- [5] Chan, R. W. K., Albermani, F., and M. S. Williams (2009), “Evaluation of yielding shear panel device for passive energy dissipation,” *J. Constr. Steel Res.*, Vol (65), no. 2, pp. 260–268.
- [6] Lewis, G. R. (2010), "Replaceable Shear and Flexural Links for the Linked Column Frame System,". Department of Civil and Environment Engineering, Portland State University.
- [7] Li, G. and Li, H. N. (2013), “Experimental study and application in steel structure of ‘dual

- functions' metallic damper," *Adv. Steel Constr.*, Vol (9), no. 3, pp. 247–258.
- [8] Tang, J. Li, Y. and Liu, X. (2015), "Research on Dissipation and Fatigue Capacity of Nonstiffener Shear Panel Dampers," *Adv. Civ. Eng.*, Vol (2015).
- [9] Li, Z., Albermani, F., Chan, R. W. K., and Kitipornchai, S. (2011), "Pinching hysteretic response of yielding shear panel device," *Eng. Struct.*, Vol (33), no. 3, pp. 993–1000.
- [10] Ma, X., Borchers, E., Krawinkler, H., and Deierlein, G. (2011), "Design and Behavior of Steel Shear Plates with Openings as Energy Dissipating Fuses," Report no. 173, Department of Civil and Environment Engineering, Stanford University.
- [11] Sahoo, D. R., Singhal, T., Taraithia, S. S., and Saini, A. (2015), "Cyclic behavior of shear-and-flexural yielding metallic dampers," *J. Constr. Steel Res.*, Vol (114), pp. 247–257.
- [12] Stephens, M. T. (2011), "Numerical and Experimental Analysis of Composite Sandwich Links for the LCF System," Civil and Environmental Engineering, Portland State University.
- [13] Symans, M., Charney, F., Whittaker, A., Constantinou, M., Kircher, C., Johnson, M., and McNamara, R. (2008), "Energy dissipation systems for seismic applications: current practice and recent developments," *J. Struct. Eng.*, Vol (134), no. 1, pp. 3–21.
- [14] Teruna, D. R., Majid, T. A., and Budiono, B. (2015), "Experimental study of hysteretic steel damper for energy dissipation capacity," *Adv. Civ. Eng.*, Vol (2015).

- [15] Valizadeh, H., Sheidaii, M., and Showkati, H. (2012), "Experimental investigation on cyclic behavior of perforated steel plate shear walls," *J. Constr. Steel Res.*, Vol (70), pp. 308–316.
- [16] Zhang, C., Zhang, Z., and Shi, J., (2012), "Development of high deformation capacity low yield strength steel shear panel damper," *J. Constr. Steel Res.*, Vol (75), pp. 116–130.
- [17] Zheng, J., Li, A., and Guo, T., (2015), "Analytical and experimental study on mild steel dampers with non-uniform vertical slits," *Earthq. Eng. Eng. Vib.*, Vol (14), no. 1, pp. 111–123.
- [18] Constantinou, M. C., & Symans, M. D. (1992), "Experimental and analytical investigation of seismic response of structures with supplemental fluid viscous dampers," Buffalo, NY: National Center for earthquake engineering research.
- [19] Zhang, R. H., & Soong, T. T. (1992), "Seismic design of viscoelastic dampers for structural applications," *Journal of Structural Engineering*, Vol(118),no.5, pp. 1375-1392.
- [20] Wolski, M., Ricles, J. M., & Sause, R. (2009), "Experimental study of a self-centering beam–column connection with bottom flange friction device," *Journal of Structural Engineering*, Vol(135),no. 5, pp. 479-488.
- [21] Zhu, S., & Zhang, Y. (2008), "Seismic analysis of concentrically braced frame systems with self-centering friction damping braces," *Journal of Structural Engineering*, Vol(134), no. 1, pp. 121-131.

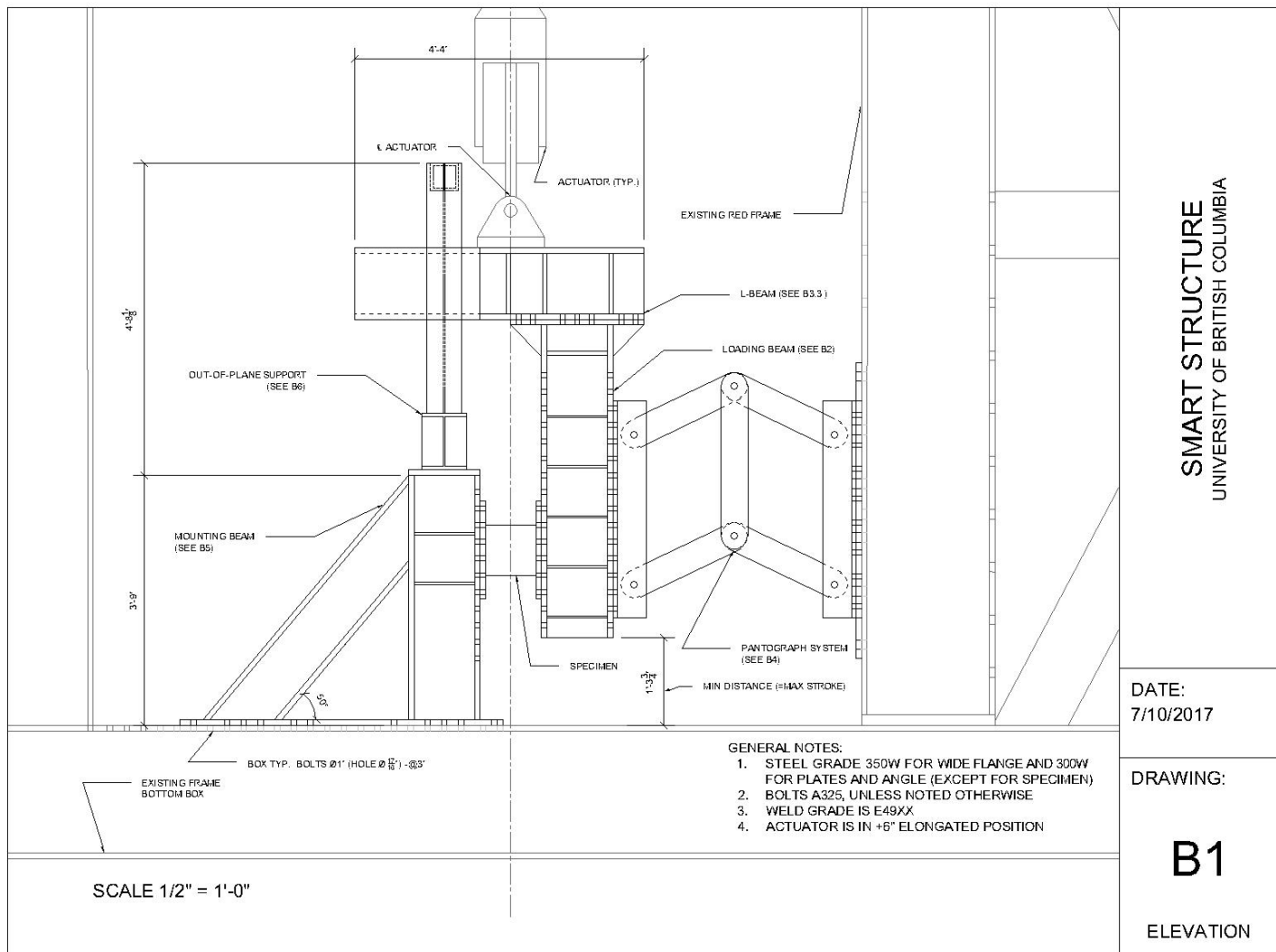
- [22] Clark, P.W., Aiken, I.D., Kelly, J.M., Higashino, M. and Krumme, R. (1995), "Experimental and analytical studies of shape-memory alloy dampers for structural control," *Smart Structures and Materials 1995: Passive Damping*, Vol. (2445), pp. 241-252).
- [23] DesRoches, R., & Delemont, M. (2002), "Seismic retrofit of simply supported bridges using shape memory alloys," *Engineering Structures*, Vol. (24), no. 3, pp. 325-332.
- [24] Iwata, M., Kato, T., & Wada, A. (2000). "Buckling-restrained braces as hysteretic dampers". *Behavior of Steel Structures in Seismic Areas*, pp. 33-38.
- [25] Pachoumis, D. T., Galoussis, E. G., Kalfas, C. N., & Christitsas, A. D. (2009), "Reduced beam section moment connections subjected to cyclic loading: Experimental analysis and FEM simulation," *Engineering Structures*, Vol. (31), no. 1, pp. 216-223.
- [26] Krawinkler, H., & Popov, E. P. (1982). "Seismic behavior of moment connections and joints," *Journal of the Structural Division*, Vol. (108), no. 2, pp. 373-391.
- [27] Ghabraie, K., Chan, R., Huang, X., & Xie, Y. M. (2010), "Shape optimization of metallic yielding devices for passive mitigation of seismic energy," *Engineering Structures*, Vol. (32), no. 8, pp. 2258-2267.
- [28] Xie, Q. (2015), "State of the art of buckling-restrained braces in Asia," *Journal of Constructional Steel Research*, Vol. (61), no. 6, pp. 727-748.

- [29] Dusicka, P., Itani, A. M., & Buckle, I. G. (2004), "Evaluation of conventional and specialty steels in shear link hysteretic energy dissipators," *Proceedings of the 13th World Conference on Earthquake Engineering*, Paper No. 522.
- [30] Bruneau, M., Uang, C., & Sabelli, R. (2011), "*Ductile Design of Steel Structures, 2nd Edition*," McGraw-Hill Professional.
- [31] M. Smith (2009), "*ABAQUS/Standard User's Manual*, Version 6.9. Providence, RI: Simulia.

Appendices

Appendix A

Testing apparatus shop drawing



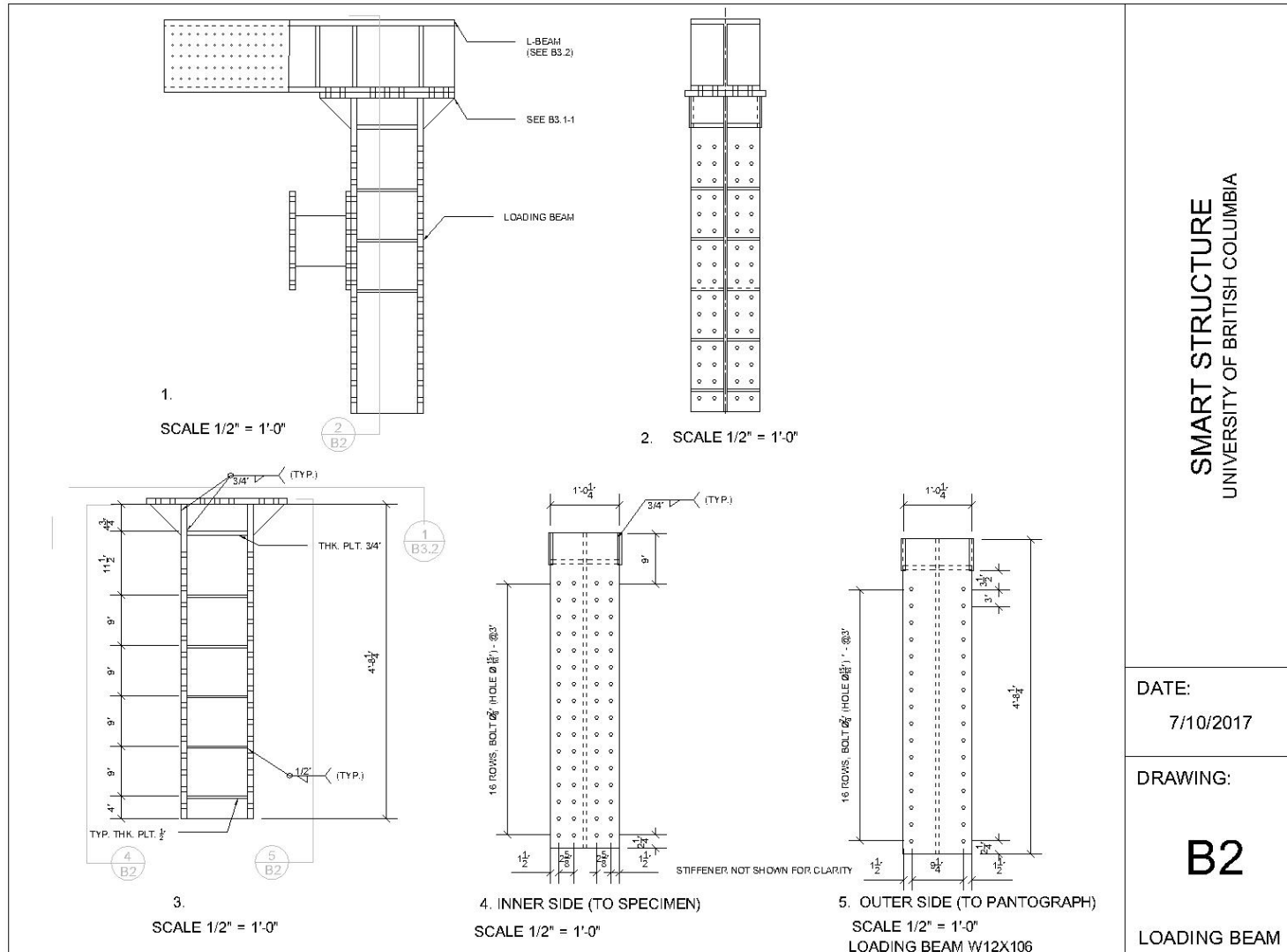
SMART STRUCTURE
UNIVERSITY OF BRITISH COLUMBIA

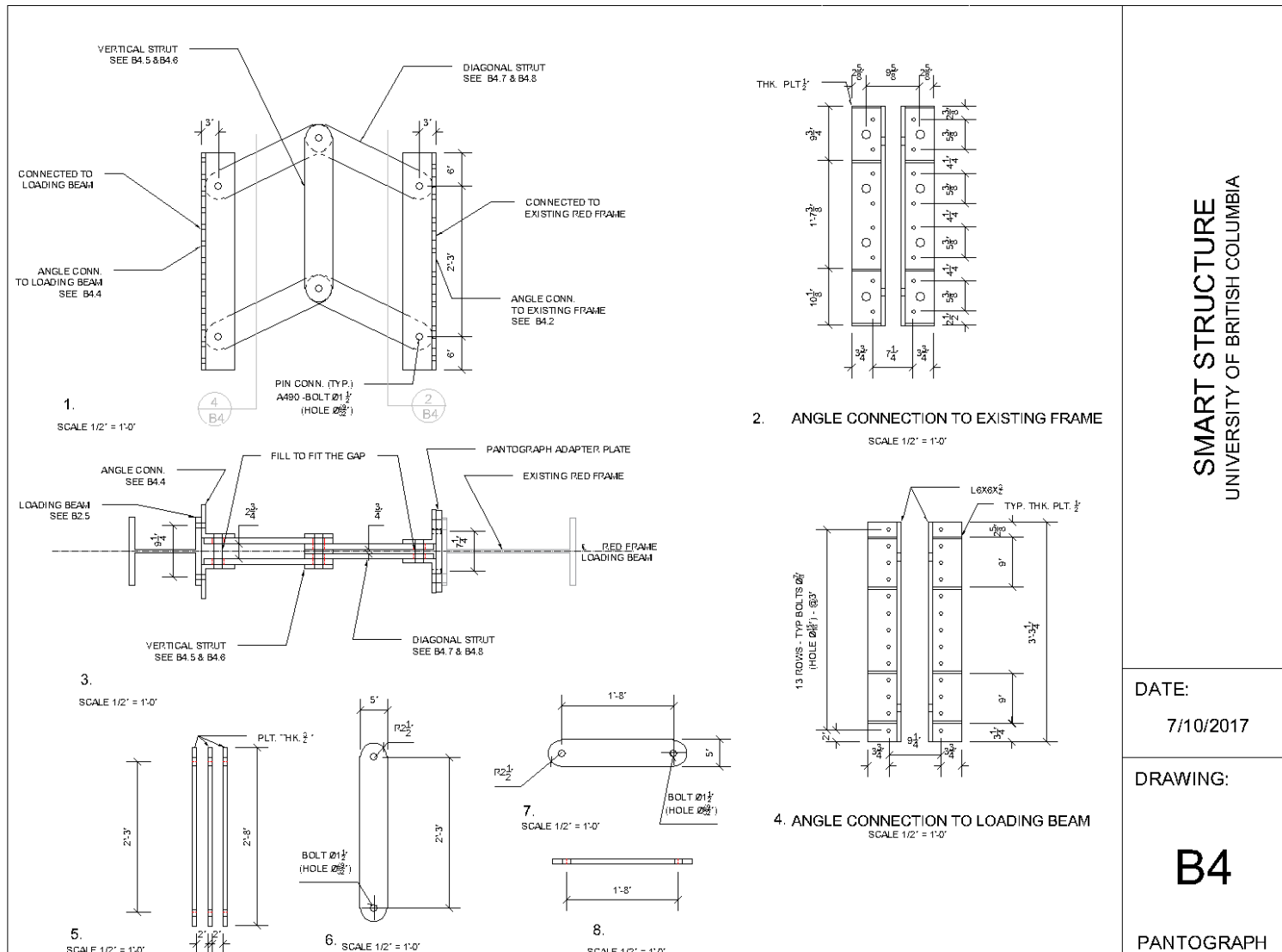
DATE:
7/10/2017

DRAWING:

B1

ELEVATION





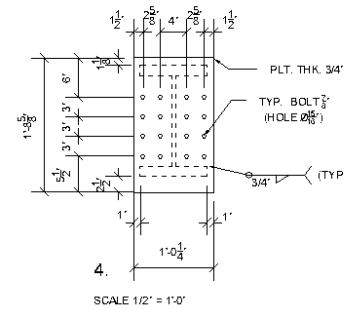
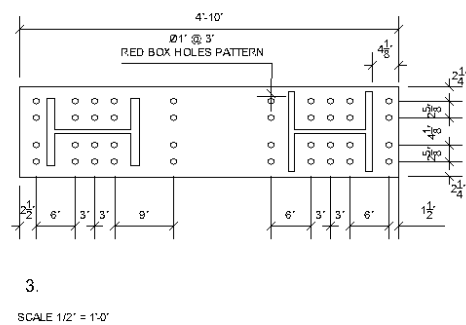
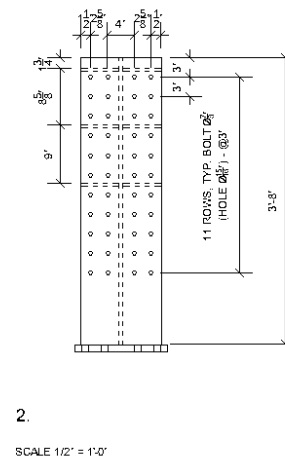
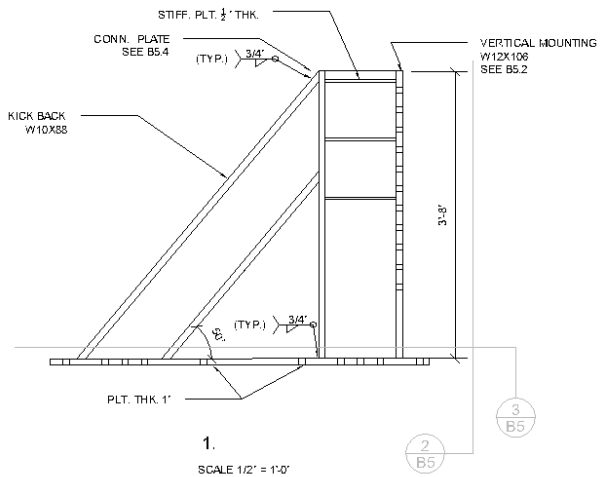
SMART STRUCTURE
UNIVERSITY OF BRITISH COLUMBIA

DATE:
7/10/2017

DRAWING:

B4

PANTOGRAPH



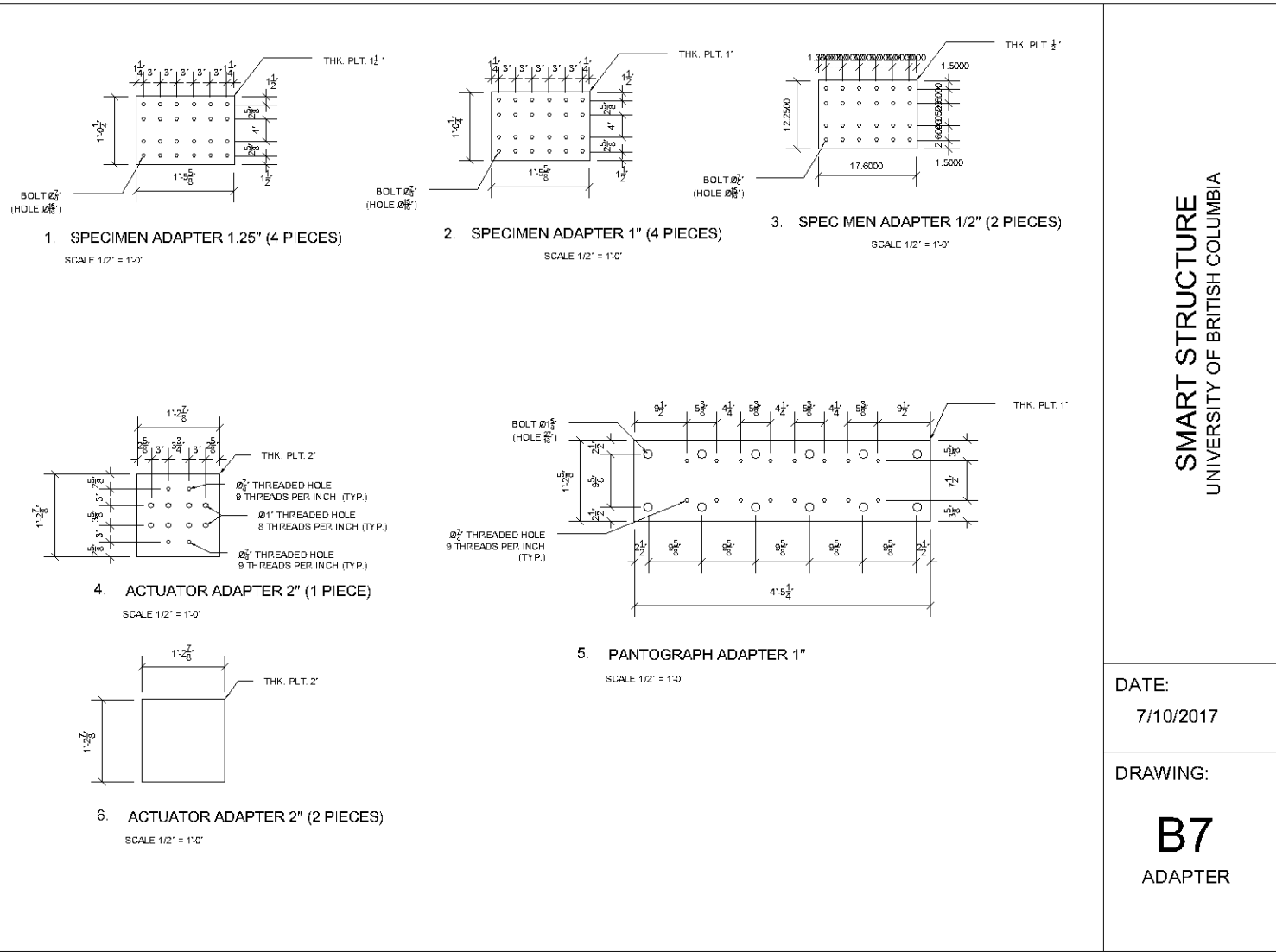
SMART STRUCTURE
UNIVERSITY OF BRITISH COLUMBIA

DATE:
7/10/2017

DRAWING:

B5

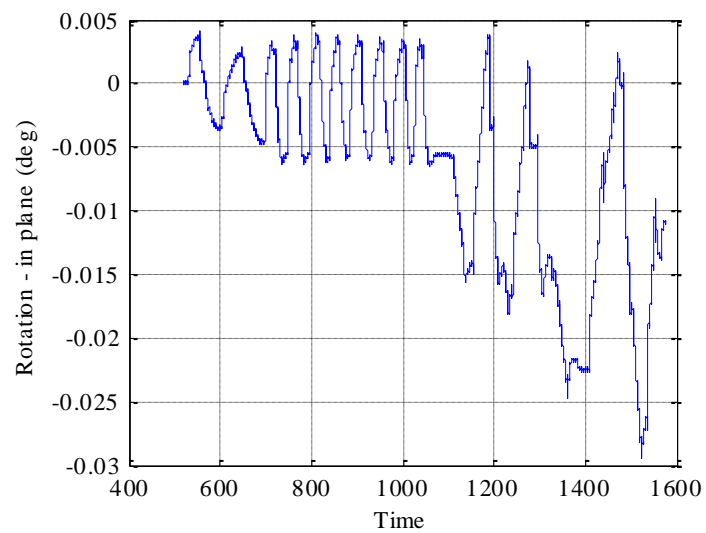
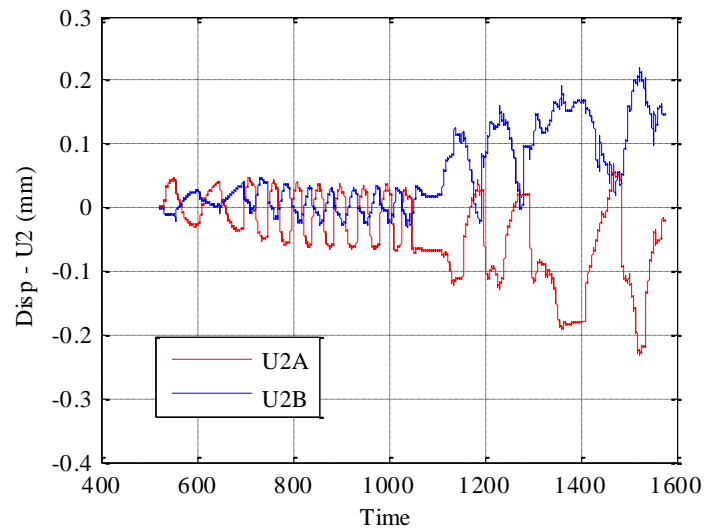
MOUNTING



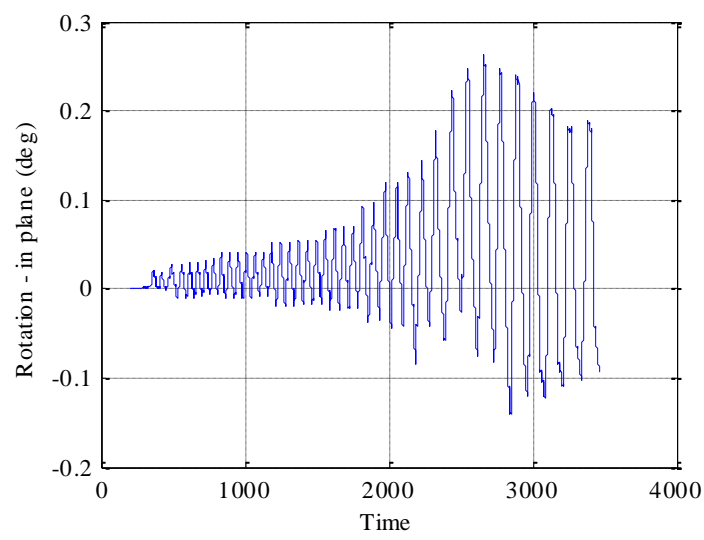
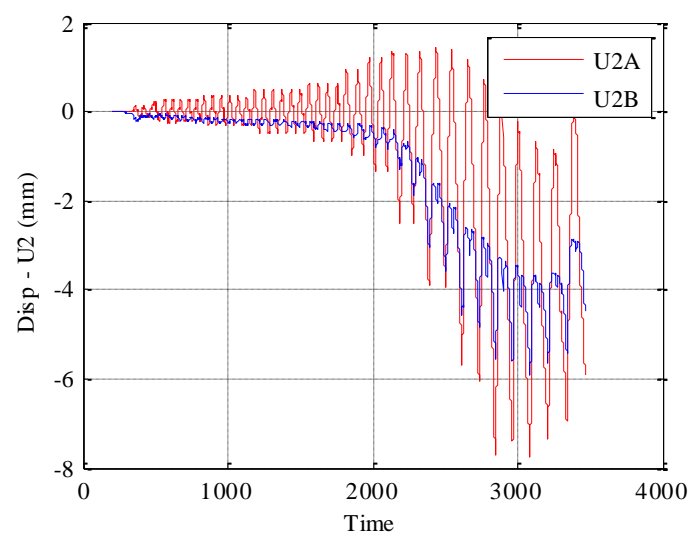
Appendix B

U2 displacement and rotation

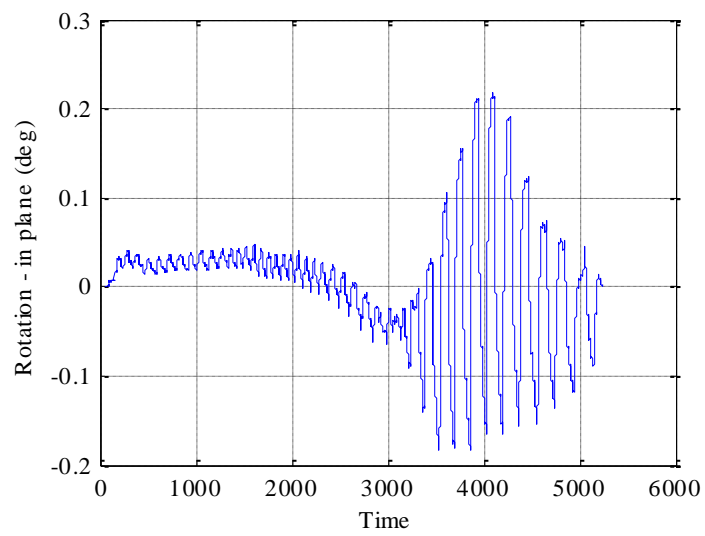
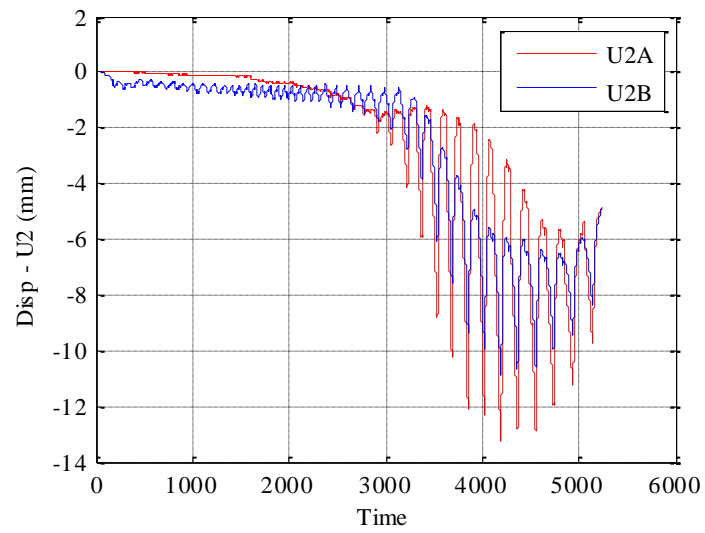
A0.75S22



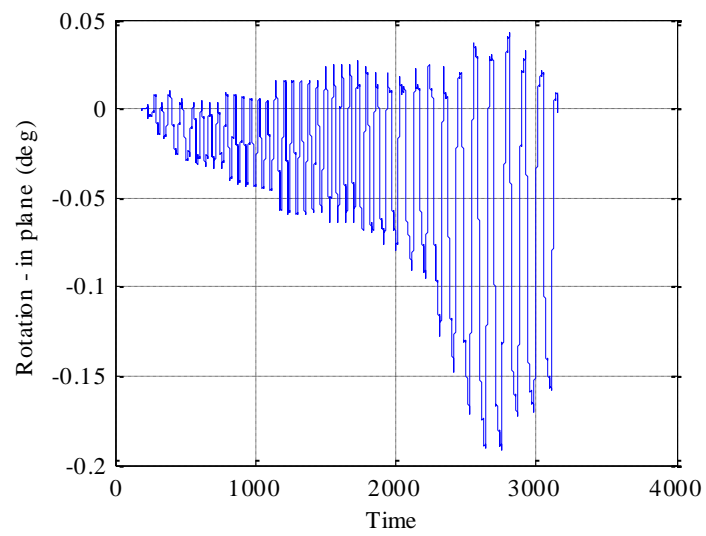
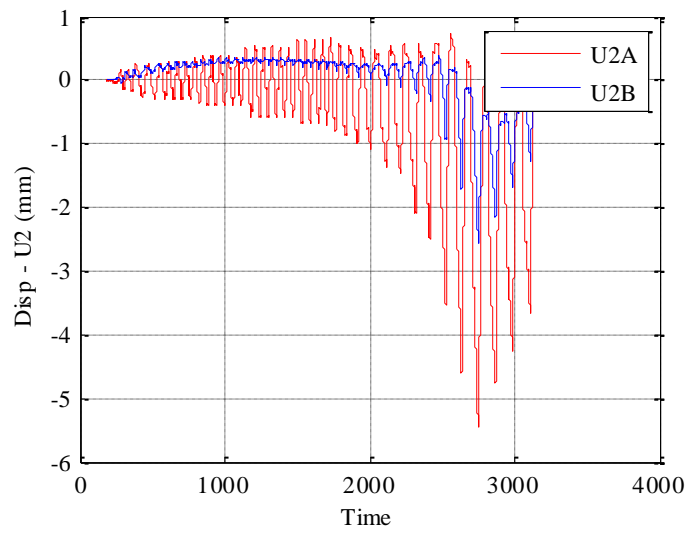
A0.75S22-1.3

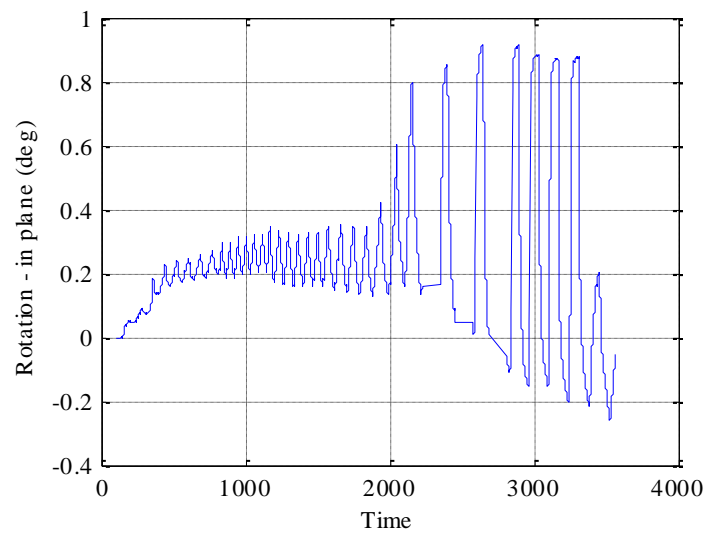
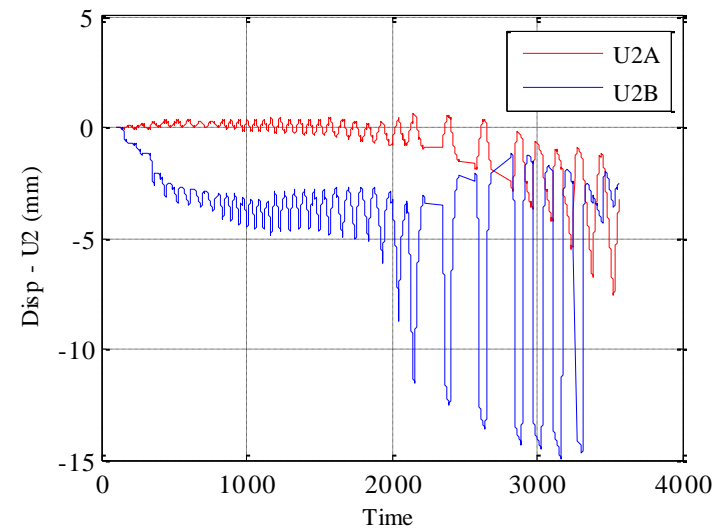


A0.75S22-2

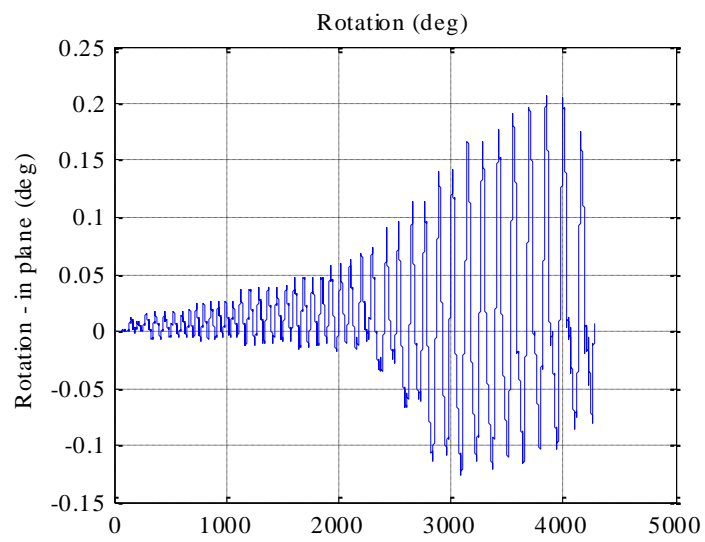
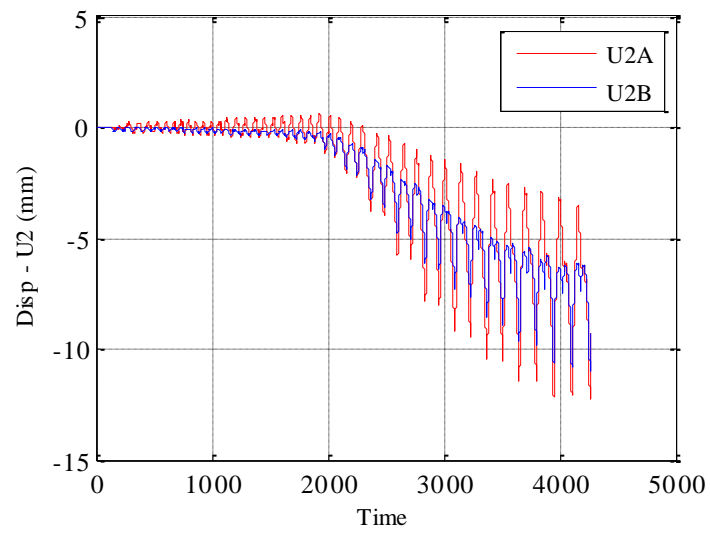


A1.5S22

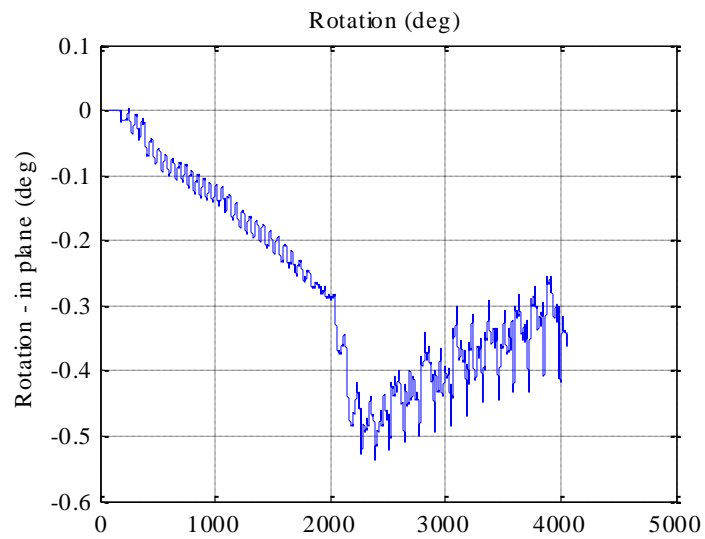
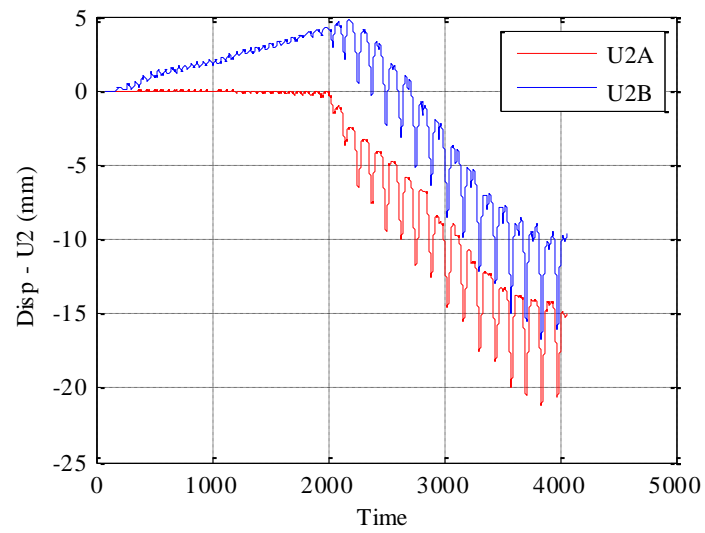


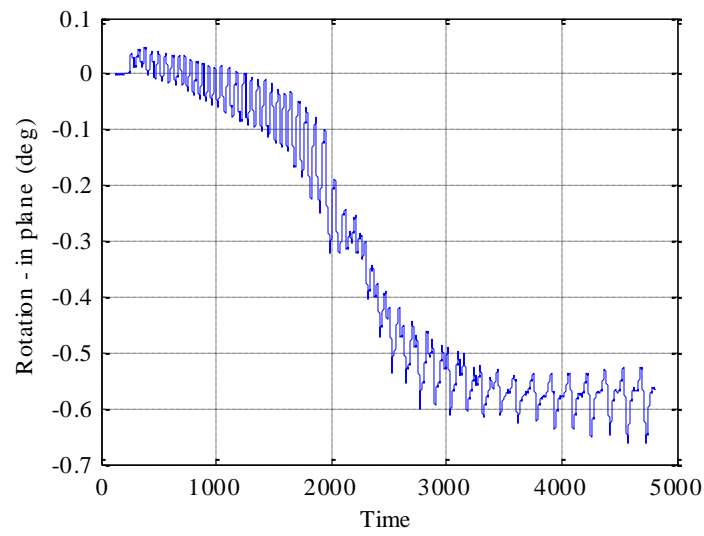
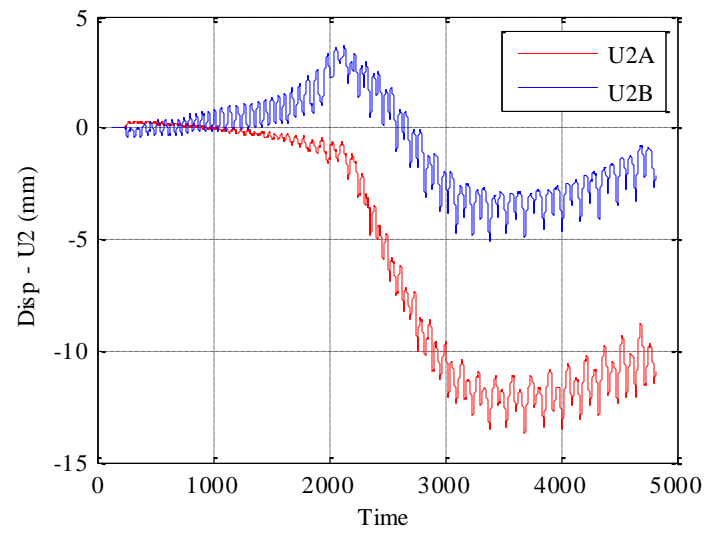


A0.75S32

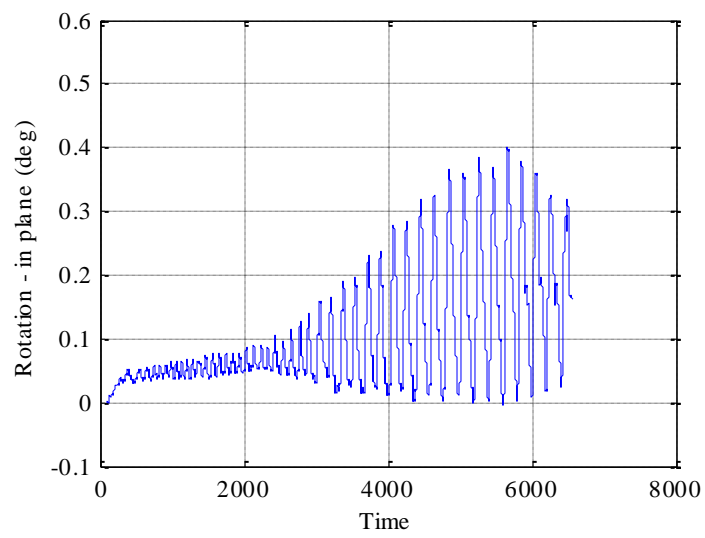
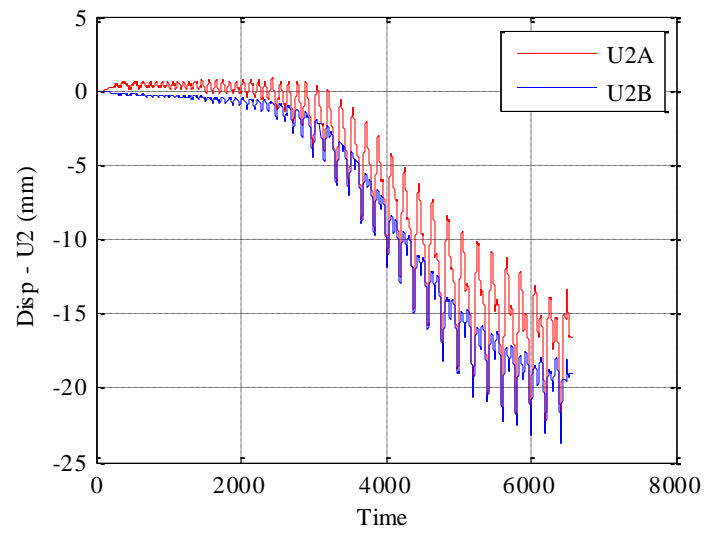


A1.5S32

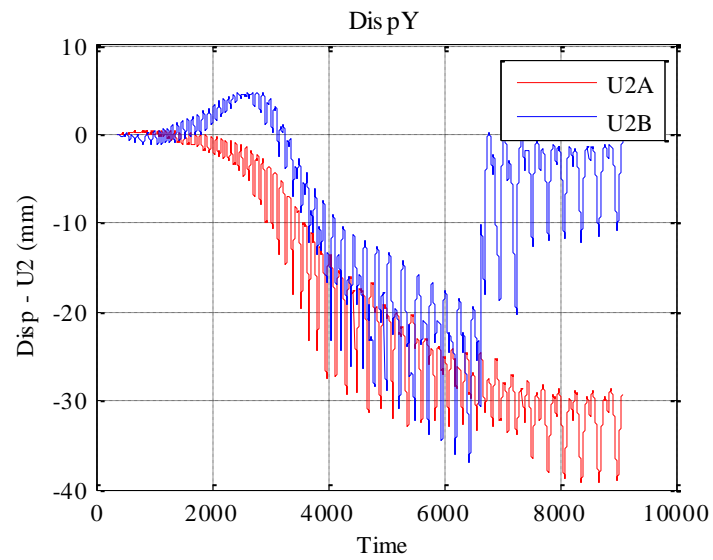




A0.75S43



A1.5S43



*U2B jump around 6700 was due to manual adjustment of LP3

